

INTRACLUSTER MEDIUM ENTROPY PROFILES FOR A CHANDRA ARCHIVAL SAMPLE OF GALAXY CLUSTERS

Kenneth. W. Cavagnolo^{1,2}, Megan Donahue¹, G. Mark Voit¹, and Ming Sun^{1,3}

ABSTRACT

We present radial entropy profiles of the intracluster medium (ICM) for a collection of 239 clusters taken from the *Chandra* X-ray Observatory's Data Archive. Entropy is of great interest because it controls ICM global properties and records the thermal history of a cluster. Entropy is therefore a useful quantity for studying the effects of feedback on the cluster environment and investigating any breakdown of cluster self-similarity. We find that most ICM entropy profiles are well-fit by a model which is a power-law at large radii and approaches a constant value at small radii: $K(r) = K_0 + K_{100}(r/100 \text{ kpc})^\alpha$, where K_0 quantifies the typical excess of core entropy above the best fitting power-law found at larger radii. We also show that the K_0 distributions of both the full archival sample and the primary *HIFLUGCS* sample of Reiprich (2001) are bimodal with a distinct gap between $K_0 \approx 30 - 50 \text{ keV cm}^2$ and population peaks at $K_0 \sim 15 \text{ keV cm}^2$ and $K_0 \sim 150 \text{ keV cm}^2$. The effects of PSF smearing and angular resolution on best-fit K_0 values are investigated using mock *Chandra* observations and degraded entropy profiles, respectively. We find that neither of these effects is sufficient to explain the entropy-profile flattening we measure at small radii. The influence of profile curvature and number of radial bins on best-fit K_0 is also considered, and we find no indication K_0 is significantly impacted by either. For completeness, we include previously unpublished optical spectroscopy of $\text{H}\alpha$ and $[\text{N II}]$ emission lines discussed in Cavagnolo et al. (2008a). All data and results associated with this work are publicly available via the project web site.

Subject headings: astronomical data bases: miscellaneous – cooling flows – X-rays: general – X-rays: galaxies: clusters

¹Michigan State University, Department of Physics and Astronomy, East Lansing, MI, 48824-2320

²University of Waterloo, Department of Physics and Astronomy, Waterloo, ON, N2L 2G1; kcavagno@scimail.uwaterloo.ca

³University of Virginia, Department of Astronomy, Charlottesville, VA, 22904

1. Introduction

The general process of galaxy cluster formation through hierarchical merging is well understood, but many details, such as the impact of feedback sources on the cluster environment and radiative cooling in the cluster core, are not. The nature of feedback operating within clusters is of great interest because of the implications regarding the formation of massive galaxies and for the cluster mass-observable scaling relations used in cosmological studies. Early models of structure formation which included only gravitation predicted self-similarity among the galaxy cluster population. These self-similar models made specific predictions for how the physical properties of galaxy clusters, such as temperature and luminosity, should scale with cluster redshift and mass (Kaiser 1986, 1991; Evrard & Henry 1991; Navarro et al. 1995, 1997; Evrard et al. 1996; Evrard 1997; Teyssier et al. 1997; Eke et al. 1998; Bryan & Norman 1998). However, numerous observational studies have shown clusters do not follow the tight mass-observable scaling relations predicted by simulations (Edge & Stewart 1991; Allen & Fabian 1998; Markevitch 1998; Arnaud & Evrard 1999; Horner et al. 1999; Nevalainen et al. 2000; Finoguenov et al. 2001). To reconcile observation with theory, it was realized non-gravitational effects, such as heating and radiative cooling in cluster cores, could not be neglected if models were to accurately replicate the process of cluster formation (*e.g.* Kaiser 1991; Evrard & Henry 1991; Loewenstein 2000; Voit et al. 2002; Borgani et al. 2002).

As a consequence of radiative cooling, best-fit total cluster temperature decreases while total cluster luminosity increases. In addition, feedback sources such as active galactic nuclei (AGN) and galactic winds can drive cluster cores (where most of the cluster flux originates) away from hydrostatic equilibrium. Thus, at a given mass scale, radiative cooling and feedback conspire to create dispersion in otherwise theoretically tight mass-observable correlations like mass-luminosity and mass-temperature. While considerable progress has been made both observationally and theoretically in the areas of understanding, quantifying, and reducing scatter in cluster scaling relations (Buote & Tsai 1996; Jeltama et al. 2005; Kravtsov et al. 2006; O’Hara et al. 2006; Nagai et al. 2007; Ventimiglia et al. 2008), it is still important to understand how non-gravitational processes, taken as a whole, affect cluster formation and evolution.

A related issue to the departure of clusters from self-similarity is that of cooling flows in cluster cores. The core cooling time in 50%-66% of clusters is much shorter than both the Hubble time and cluster age (Stewart et al. 1984; Edge et al. 1992; White et al. 1997; Peres et al. 1998; Bauer et al. 2005). For such clusters (and without compensatory heating), radiative cooling will result in the formation of a cooling flow (see Fabian 1994, for a review). Early estimates put the mass deposition rates from cooling flows in the range of 100 –

$1000 \text{ M}_\odot \text{ yr}^{-1}$ (*e.g.* Jones & Forman 1984; Edge et al. 1994; Peres et al. 1998) However, cooling flow mass deposition rates inferred from soft X-ray spectroscopy were found to be significantly less than predicted, without much gas reaching temperatures lower than $T_{\text{virial}}/3$ (Tamura et al. 2001; Peterson et al. 2001, 2003; Kaastra et al. 2004) Irrespective of system mass, the expected massive torrents of cool gas turned out to be more like cooling trickles.

In addition to the lack of soft X-ray line emission from cooling flows, prior methodical searches for the end products of cooling flows (*i.e.* in the form of molecular gas and emission line nebulae) revealed far less mass is locked-up in cooled by-products than expected (Heckman et al. 1989; McNamara et al. 1990; O’Dea et al. 1994; Voit & Donahue 1995). The disconnects between observation and theory have been termed “the cooling flow problem” and raise the question, “Where has all the cool gas gone?” The substantial amount of observational evidence suggests some combination of energetic feedback sources, such as AGN outbursts and supernovae explosions, have heated the ICM to selectively remove gas with a short cooling time and establish quasi-stable thermal balance in the ICM.

Both the breakdown of self-similarity and the cooling flow problem point toward the need for a better understanding of cluster feedback and radiative cooling. Recent revisions to models of how clusters form and evolve by including feedback sources has led to better agreement between observation and theory (Bower et al. 2006; Croton et al. 2006; Saro et al. 2006; Bower et al. 2008). The current paradigm regarding the cluster feedback process holds that AGN are the primary heat delivery mechanism and that an AGN outburst deposits the requisite energy into the ICM to retard, and in some cases, possibly quench cooling (see McNamara & Nulsen 2007, for a review). How the feedback loop functions is still the topic of much debate, but that AGN are interacting with the hot atmospheres of clusters is no longer in doubt as evidenced by the prevalence of ICM bubbles (*e.g.* Bîrzan et al. 2004; Dunn & Fabian 2008), the possible presence of sound waves (Fabian et al. 2003; Sanders & Fabian 2008), and large-scale shocks associated with AGN outbursts (Forman et al. 2005; McNamara et al. 2005; Nulsen et al. 2005).

One robust observable which has proven useful in studying the effect of non-gravitational processes is ICM entropy. Taken individually, ICM temperature and density do not fully reveal a cluster’s thermal history. ICM temperature primarily reflects the depth of a cluster potential well, while the ICM density mostly reflects the capacity of the well to compress the gas. However, at constant pressure the density of a gas is determined by its specific entropy. By rewriting the expression for the adiabatic index – which can be expressed as $K \propto P\rho^{-5/3}$ – using the observables X-ray temperature (T_X) and electron density (n_e), one can define a new quantity, $K = T_X n_e^{-2/3}$ (Ponman et al. 1999; Lloyd-Davies et al. 2000). The quantity K captures the thermal history of a gas because only gains and losses of heat energy can

change K . The expression for K using observable X-ray quantities is commonly referred to as entropy in the X-ray cluster literature, but in actuality the classic thermodynamic specific entropy for a monatomic ideal gas is $s = \ln K^{3/2} + \text{constant}$.

One important property of gas entropy is that convective stability is approached in the ICM when $dK/dr \geq 0$. Thus, gravitational potential wells are giant entropy sorting devices: low entropy gas sinks to the bottom of the potential well, while high entropy gas buoyantly rises to a radius at which the ambient gas has equal entropy. If cluster evolution proceeded under the influence of gravitation only, then the radial entropy distribution of clusters would exhibit power-law behavior for $r > 0.1r_{200}$ with a constant, low entropy core at small radii (Voit et al. 2005). Thus, large-scale departures of the radial entropy distribution from a power-law can be used to measure the effect processes such as AGN heating and radiative cooling have on the ICM. Several studies have previously found that the radial ICM entropy distribution in some clusters flattens at $< 0.1r_{\text{virial}}$, or that the core entropy has much larger dispersion than the entropy at larger radii (David et al. 1996; Ponman et al. 1999; Lloyd-Davies et al. 2000; Ponman et al. 2003; Piffaretti et al. 2005; Donahue et al. 2005; Pratt et al. 2006; Donahue et al. 2006; Morandi & Ettori 2007). However, these previous studies used smaller, focused samples, and to expand the utility of entropy in understanding cluster thermodynamic history and non-gravitational processes, we have undertaken a much larger study utilizing the *Chandra* Data Archive.

In this paper we present the data analysis and results from a *Chandra* archival project in which we studied the ICM entropy distribution for 239 galaxy clusters. We have named this project the “Archive of *Chandra* Cluster Entropy Profile Tables” or *ACCEPT* for short. In contrast to the sample of nine classic cooling flow clusters studied in Donahue et al. (2006, hereafter D06), *ACCEPT* covers a broader range of luminosities, temperatures, and morphologies, focusing on more than just cooling flow clusters. One of our primary objectives for this project was to provide the research community with an additional resource to study cluster evolution and confront current and future ICM models with a comprehensive set of entropy profiles.

We have found that the departure of entropy profiles from a power-law at small radii is a feature of most clusters, and given high enough angular resolution, possibly all clusters. We also find that the core entropy distribution of both the full *ACCEPT* collection and the Highest X-Ray Flux Galaxy Cluster Sample (*HIFLUGCS*, Reiprich 2001; Reiprich & Böhringer 2002) are bimodal. In a separate letter (Cavagnolo et al. 2008a), we presented results that show indicators of feedback like radio sources assumed to be associated with AGN and H α emission are strongly correlated with core entropy.

A key aspect of this project is the dissemination of all data and results to the public. We

have created a searchable, interactive web site¹ which hosts all of our results. The *ACCEPT* web site will be continually updated as new *Chandra* cluster and group observations are archived and analyzed. The web site provides all data tables, plots, spectra, reduced *Chandra* data products, reduction scripts, and more. Given the large number of clusters in our sample, we have omitted figures, and tables showing/listing results for individual clusters from this paper and have made them available at the *ACCEPT* web site.

The structure of this paper is as follows: In §2 we outline initial sample selection criteria and information about the *Chandra* observations selected under these criteria. Data reduction is discussed in §3. Spectral extraction and analysis are discussed in §3.1, while our method for deriving deprojected electron density profiles is outlined in §3.2. A few possible sources of systematics are discussed in §4. Results and discussion are presented in §5. A brief summary is given in §6. For this work we have assumed a flat Λ CDM Universe with cosmology $\Omega_M = 0.3$, $\Omega_\Lambda = 0.7$, and $H_0 = 70 \text{ km s}^{-1} \text{ Mpc}^{-1}$. All quoted uncertainties are 90% confidence.

2. Data Collection

Our sample is collected from observations taken with the *Chandra* X-ray Observatory (Weisskopf et al. 2000) and which are publicly available in the *Chandra* Data Archive (CDA) as of August 2008. All data was taken with the ACIS detectors (Garmire et al. 2003), which have a pixel scale of $\sim 0.492''$ with an on-axis point spread function (PSF) which is smaller than the detectors’ pixel size. ACIS has an energy resolution of $< 100 \text{ eV}$ for $E \lesssim 2 \text{ keV}$ and $< 300 \text{ eV}$ at all energies. *Chandra*’s unobscured collecting area is $\sim 1145 \text{ cm}^2$ with an effective area of $\sim 600 \text{ cm}^2$ around the peak emission energies of a typical galaxy cluster. At launch ACIS-I and ACIS-S differed by the better soft-energy sensitivity of ACIS-S, but in-flight degradation of the CCDs has slowly closed the differences between the two chip arrays.

We retrieved all data from the CDA listed under the CDA Science Categories “clusters of galaxies” or “active galaxies.” As of submission, we have inspected all CDA clusters of galaxies observations and analyzed 510 of those observations (14.16 Msec). The Coma and Fornax clusters have been intentionally left out of our sample because they are very well studied nearby clusters which require a more intensive analysis than we undertook in this project.

¹<http://www.pa.msu.edu/astro/MC2/accept>

The data available for some clusters limited our ability to derive an entropy profile. Calculation of ICM entropy requires measurement of the gas temperature and density structure as a function of radius (discussed further in §3). To infer temperatures which were reasonably well constrained ($\Delta(kT_X) \approx \pm 1.0$ keV) and to measure more than linear temperature gradients, we imposed the requirements that each cluster temperature profile have at least three concentric radial annular bins containing a minimum of 2500 source counts each. A post-analysis check showed our minimum source counts criterion resulted in a mean $\Delta(kT_X) = 0.87$ keV for the final sample.

In section 5.4 we cull the flux-limited *HIFLUGCS* primary sample (Reiprich 2001; Reiprich & Böhringer 2002) from our full archival collection. The groups M49, NGC 507, NGC 4636, NGC 5044, NGC 5813, and NGC 5846 are part of the *HIFLUGCS* primary sample but were not members of our initial archival sample. In order to take full advantage of the *HIFLUGCS* primary sample, we analyzed observations of these 6 groups. Note, however, that none of these 6 groups are included in the general discussion of *ACCEPT*.

We were unable to analyze some clusters for this study because of complications other than not meeting our minimum requirements for analysis. These clusters were: 2PIGG J0311.8-2655, 3C 129, A168, A514, A753, A1367, A2634, A2670, A2877, A3074, A3128, A3627, AS0463, APMCC 0421, MACS J2243.3-0935, MS J1621.5+2640, RX J1109.7+2145, RX J1206.6+2811, RX J1423.8+2404, SDSS J198.070267-00.984433, Triangulum Australis, and Zw5247.

After applying the temperature profile constraints, adding the 6 *HIFLUGCS* groups, and removing troublesome observations, the final sample presented in this paper contains 317 observations of 239 clusters with a total exposure time of 9.86 Msec. The sample covers the temperature range $kT_X \sim 1 - 20$ keV, a bolometric luminosity range of $L_{bol} \sim 10^{42-46}$ ergs s⁻¹, and redshifts of $z \sim 0.05 - 0.89$. Table 1 lists the general properties for each observation in *ACCEPT*.

We also report previously unpublished H α observations taken by M. Donahue. These observations do not enter into the analysis performed in this paper but are used in Cavagnolo et al. (2008a). Since this paper represents the data of the full project, we include them here. The new $[N II]/H\alpha$ ratios and H α fluxes are listed in Table 3. The upper-limits listed in Table 3 are 3σ significance. The observations were taken with either the 5 m Hale Telescope at the Palomar Observatory, USA, or the Du Pont 2.5 m telescope at the Las Campanas Observatory, Chile. All observations were made with a 2'' slit centered on the brightest cluster galaxy (BCG) using two position angles: one along the semi-major axis and one along the semi-minor axis of the galaxy. The red light (555-798 nm) setup on the Hale Double Spectrograph used a 316 lines/mm grating with a dispersion of 0.31 nm/pixel and

an effective resolution of 0.7-0.8 nm. The Du Pont Modular Spectrograph setup included a 1200 lines/mm grating with a dispersion of 0.12 nm/pixel and an effective resolution of 0.3 nm. The statistical and calibration uncertainties for the observations are both $\sim 10\%$. The statistical uncertainty arises primarily from uncertainty in the continuum subtraction.

3. Data Analysis

Measuring ICM entropy profiles first requires measurement of ICM temperature and density profiles. As discussed in Cavagnolo et al. (2008b), the ICM X-ray peak of the point-source cleaned, exposure-corrected cluster image was used as the cluster center, unless the iteratively determined X-ray centroid was more than 70 kpc away from the X-ray peak, in which case the centroid was used as the radial analysis zero point (see Cavagnolo et al. (2008b) for more details on centroiding procedure). The radial temperature structure of each cluster was measured by fitting a single-temperature thermal model to spectra extracted from concentric annuli centered on the cluster X-ray center. To derive the gas density profile, we first deprojected an exposure-corrected, background-subtracted, point source clean surface brightness profile extracted in the 0.7-2.0 keV energy range to attain a volume emission density. This emission density, along with spectroscopic information (count rate and normalization in each annulus), was then used to calculate gas density. The resulting entropy profiles were then fit with two models: a simple model consisting of only a radial power law, and a model which is the sum of a constant core entropy term, K_0 , and the radial power law.

In this paper we cover the basics of deriving gas entropy from X-ray observables, and direct interested readers to D06 for more in-depth discussion of our data reprocessing and reduction, and Cavagnolo et al. (2008b) for details regarding determination of each cluster’s center and how the X-ray background was handled. The only difference between the data reduction presented in this paper and that of D06 and Cavagnolo et al. (2008b), is that we have used newer versions of the *Chandra* X-ray Center (CXC) issued data reduction software (CIAO 3.4.1 and calibration files in the CALDB 3.4.0).

3.1. Temperature Profiles

One of the two components needed to derive a gas entropy profile is the temperature as a function of radius. We therefore constructed radial temperature profiles for each cluster in our collection. To reliably constrain a temperature, and allow for the detection of tem-

perature structure beyond linear gradients, we required each temperature profile to have a minimum of three annuli containing 2500 counts each. The annuli for each cluster were generated by first extracting a background-subtracted cumulative counts profile using 1 ACIS detector pixel width annular bins (1 ACIS pixel $\approx 0.492''$) originating from the cluster center and extending to the detector edge. We truncated temperature profiles at the radius bounded by the detector edge, or $0.5r_{180}$, whichever was smaller. Truncation occurred at $0.5r_{180}$ as we are most interested in the radial entropy behavior of cluster core regions ($r \lesssim 100$ kpc) and $0.5r_{180}$ is the approximate radius where temperature profiles begin to decline at larger radii (Vikhlinin et al. 2005). Additionally, analysis of diffuse gas temperature structure at large radii, which spectroscopically is dominated by background, requires a time consuming, observation-specific analysis of the X-ray background (see Sun et al. 2008, for a detailed discussion on this point).

Cumulative counts profiles were divided into annuli containing at least 2500 counts. For well-resolved clusters, the number of counts per annulus was increased to reduce the resulting uncertainty of kT_X and, for simplicity, to keep the number of annuli less than 50 per cluster. The method we use to derive entropy profiles is most sensitive to the surface brightness radial bin size and not the resolution or uncertainties of the temperature profile. Thus, the loss of resolution in the temperature profile from increasing the number of counts per bin, and thereby reducing the number of annuli, has an insignificant effect on the final entropy profiles and best-fit entropy models.

Background analysis was performed using the blank-sky datasets provided in the CALDB. Backgrounds were reprocessed and reprojected to match each observation. Off-axis chips were used to normalize for variations of the hard-particle background by comparing blank-sky and observation 9.5-12 keV count rates. Following the analysis described in Vikhlinin et al. (2005), soft residuals were created and fitted for each observation to account for the spatially-varying soft Galactic background (see also Cavagnolo et al. 2008b). The best-fit spectral model for the residual soft component (scaled for sky area) was included as an additional, fixed background component during fitting of cluster spectra. Errors associated with the additional soft background component were determined by refitting cluster spectra using the $\pm 1\sigma$ temperatures of the soft background component’s best fit model and then adding the associated error in quadrature to the final error budget.

For each radial annular region, source and background spectra were extracted from the target cluster and corresponding normalized blank-sky dataset. Following standard CIAO techniques² we created weighted response files (WARF) and redistribution matrices (WRMF)

²<http://cxc.harvard.edu/ciao/guides/esa.html>

for each cluster using a flux-weighted map (WMAP) across the entire extraction region. These files quantify the effective area, quantum efficiency, and imperfect resolution of the *Chandra* instrumentation as a function of chip position. Each spectrum was binned to contain a minimum of 25 counts per energy bin.

Spectra were fitted with XSPEC 11.3.2ag (Arnaud 1996) using an absorbed, single-temperature MEKAL model (Mewe et al. 1985, 1986) over the energy range 0.7-7.0 keV. Neutral hydrogen column densities, N_{H} , were taken from Dickey & Lockman (1990). A comparison between the N_{H} values of Dickey & Lockman (1990) and the higher-resolution Leiden/Argentine/Bonn (LAB) Survey (Kalberla et al. 2005) revealed that the two surveys agree to within $\pm 20\%$ for 80% of the clusters in our sample. For the other 20% of the sample, using the LAB value, or allowing N_{H} to be free, did not result in best-fit temperatures or metallicities which differ significantly from fits using the Dickey & Lockman (1990) values.

The potentially free parameters of the absorbed thermal model are N_{H} , X-ray temperature, metal abundance normalized to solar (heavy-element ratios taken from Anders & Grevesse 1989), and a normalization (η) which is proportional to the integrated emission measure within the extraction region,

$$\eta = \frac{10^{-14}}{4\pi D_A^2 (1+z)^2} \int n_e n_p dV, \quad (1)$$

where D_A is the angular diameter distance in cm, z is the dimensionless cluster redshift, n_e and n_p are the electron and proton densities, respectively, in units of cm^{-3} , and V is the volume of the emission region in cm^3 . In all spectral fits the metal abundance in each annulus was a free parameter and N_{H} was fixed to the Galactic value. No systematic error was added during fitting and thus all quoted errors are statistical only. The statistic used during fitting was χ^2 (XSPEC statistics package CHI). All uncertainties were calculated using 90% confidence.

More than one observation was available in the archive for some clusters. We utilized the combined exposure time for these clusters by first extracting independent spectra, WARFs, WRMFs, normalized background spectra, and soft residuals for each observation. These independent spectra were then read into XSPEC simultaneously and fit with the same spectral model which had all parameters, except normalization, tied among the spectra.

Spectral deprojection of ICM temperature should result in slightly lower temperatures in the central bins of only the clusters with temperature gradients which increase steeply going out from the cluster center. For those clusters, the end result would be a slight lowering of the entropy for the central-most bins. In D06 we studied a sample of nine “classic” cooling flow clusters, all of which have steep temperature gradients ($T(r)_{\text{max}}/T(r)_{\text{min}} \sim 1.5 - 3.5$).

Our analysis in D06 showed that spectral deprojection did not result in significant differences between entropy profiles derived using projected or deprojected temperature profiles. In light of this result, and the fact that deprojection requires about a factor of 5 more computing resources and time, we opted not to deproject our spectra for this phase of the project.

3.2. Deprojected Electron Density Profiles

For predominantly free-free emission, emissivity strongly depends on density and only weakly on temperature, $\epsilon \propto \rho^2 T^{1/2}$. Since ICM temperatures generally exceed 2.0 keV, the flux measures in the energy range 0.7-2.0 keV, together with a small correction for any variations in temperature and metallicity, is therefore a good diagnostic of ICM density. To reconstruct the relevant gas density as a function of physical radius, we deprojected the cluster emission from high-resolution surface brightness profiles and converted to electron density using normalizations and count rates taken from the spectral analysis.

We extracted surface brightness profiles from the 0.7-2.0 keV energy range using concentric annular bins of width $5''$ originating from the cluster center. Surface brightness profiles were corrected with observation-specific, normalized radial exposure profiles to remove the effects of vignetting and exposure time fluctuations. Following the recommendation in the CIAO guide for analyzing extended sources, exposure maps were created using the monoenergetic value associated with the observed count rate peak. The more sophisticated method of creating exposure maps using spectral weights calculated for an incident spectrum with the temperature and metallicity of the observed cluster was also tested for a series of clusters covering a broad temperature range. For the narrow energy band we consider, the chip response is relatively flat and we find no significant differences between the two methods. For all clusters, the monoenergetic value used in creating exposure maps was between 0.8 – 1.7 keV.

The 0.7-2.0 keV spectroscopic count rate and spectral normalization were linearly interpolated from the radial temperature profile grid to match the surface brightness radial grid. Utilizing the deprojection technique of Kriss et al. (1983), the interpolated spectral parameters were used to convert observed surface brightness to deprojected electron density. The conversion from best-fit spectroscopic values to density intrinsically accounts for temperature and metal abundance variations which affect the gas emissivity in our selected energy range. Radial electron density written in terms of relevant quantities is,

$$n_e(r) = \sqrt{\frac{(n_e/n_p) \ 4\pi [D_A(1+z)]^2 \ C(r) \ \eta(r)}{10^{-14} \ f(r)}} \quad (2)$$

where $n_e/n_p \approx 1.2$ for a fully ionized solar abundance plasma, $C(r)$ is the radial emission density derived from eq. A1 in Kriss et al. (1983), η is the interpolated spectral normalization from eq. 1, D_A is the angular diameter distance, z is cluster redshift, and $f(r)$ is the interpolated spectroscopic count rate. Cosmic dimming of source surface brightness is accounted for by the $D_A^2(1+z)^2$ term. This method of deprojection takes into account temperature and metallicity fluctuations which affect observed gas emissivity. Errors for the gas density profile were estimated using 5000 Monte Carlo simulations of the original surface brightness profile. The Kriss et al. (1983) deprojection technique assumes spherical symmetry. However, D06 showed such an assumption has little effect on the final entropy profiles (see also Donahue et al. 2003; Bauer et al. 2005, for the low impact of spherical symmetry assumptions for deriving density profiles).

3.3. β -model Fits

Noisy surface brightness profiles, or profiles with irregularities such as inversions or extended flat cores, result in unstable, unphysical quantities when using an “onion” deprojection technique like that of Kriss et al. (1983). For cases where deprojection of the binned data was problematic, we resorted to fitting the surface brightness profile with a β -model (Cavaliere & Fusco-Femiano 1978), which has the positive attribute of having an analytic deprojection solution. It is well known that the β -model does not precisely represent all the features of the ICM for clusters of high central surface brightness (Ettori 2000; Loken et al. 2002; Hallman et al. 2007). However, for the profiles which required a fit, the β -model was actually a suitable approximation. These clusters have low central surface brightness, unlike the classic cool-core clusters. The single ($N = 1$) and double ($N = 2$) β -models were used in fitting,

$$S_X = \sum_{i=1}^N S_i \left[1 + \left(\frac{r}{r_{c,i}} \right)^2 \right]^{-3\beta_i + \frac{1}{2}}. \quad (3)$$

The models were fitted using Craig Markwardt’s robust non-linear least squares minimization IDL routines^{3,4}. The data input to the fitting routines were weighted using the inverse square of the observational errors. Using this weighting scheme resulted in reduced χ^2 values near unity for, on average, the inner 80% of the radial range considered. Accuracy of errors output from the fitting routine were checked against a bootstrap Monte Carlo analysis of

³<http://rsinc.com/idl/>

⁴<http://cow.physics.wisc.edu/~craigm/idl/>

1000 surface brightness realizations. Both the single- and double- β models were fit to each profile and using the F-test functionality of SHERPA⁵ we determined if the addition of extra model components was justified given the degrees of freedom and χ^2 values of each fit. If the significance was less than 0.05, the extra components were justified and the double- β model was used.

A best-fit β -model was used in place of the data when deriving electron density for the clusters listed in Table 2. These clusters are also flagged in Table 1 with the note letter ‘a.’ The best-fit β -models and background-subtracted, exposure-corrected surface brightness profiles are shown in Figure 1. See Appendix A for notes discussing individual clusters. The disagreement between the best-fit β -model and the surface brightness in the central regions for some clusters is also discussed in Appendix A. In short, the discrepancy arises from the presence of compact X-ray sources, a topic which is addressed in §3.5. All clusters requiring a β -model fit have core entropy $> 95 \text{ keV cm}^2$ and the mean best-fit parameters are listed in Table 4.

3.4. Entropy Profiles

Radial entropy profiles were calculated using the widely adopted formulation $K(r) = kT_x(r)n_e(r)^{-2/3}$. To create the radial entropy profiles, the temperature and density profiles must be on the same radial grid. This was accomplished by interpolating the temperature profile across the higher-resolution radial grid of the deprojected electron density profile using IDL’s native linear interpolation routine *interpol*. Because the density profiles have higher radial resolution, the central bin of a cluster temperature profile will span several of the innermost bins of the density profile. Since we are most interested in the behavior of the entropy profiles in the central regions, how the interpolation was performed for the inner regions is important. Thus, temperature interpolation over the region of the density profile where a single central temperature bin encompasses several density profile bins was applied in two ways: (1) as a linear gradient consistent with the slope of the temperature profile at radii larger than the central T_X bin ($\Delta T_{center} \neq 0$; ‘extr’ in Table 5), and (2) as a constant ($\Delta T_{center} = 0$; ‘flat’ in Table 5). Shown in Figure 2 is the ratio of best-fit core entropy, K_0 , using the above two methods. The five points lying below the line of equality are clusters which are best-fit by a power-law or have K_0 statistically consistent with zero. It is worth noting that both schemes yield statistically consistent values for K_0 except for the clusters marked by black squares which have a ratio significantly different from unity.

⁵<http://cxc.harvard.edu/ciao3.4/ahelp/ftest.html>

The clusters for which the two methods give K_0 values that significantly differ all have steep temperature gradients with the maximum and minimum radial temperatures differing by a factor of 1.3-5.0. Extrapolation of a steep temperature gradient as $r \rightarrow 0$ results in very low central temperatures (typically $T_X \leq T_{\text{virial}}/3$) which are inconsistent with observations, most notably Peterson et al. (2003). Most important however, is that the flattening of entropy we observe in the cores of our sample (discussed in §5.1) is **not** a result of the method chosen for interpolating the temperature profile. For this paper, we therefore focus on the entropy results derived assuming a constant temperature for the central density bins covered by a single temperature bin.

Uncertainty in $K(r)$ arising from using a single-component temperature model for each annulus during spectral analysis contributes negligibly to our final fits and is discussed in detail in the Appendix of D06. Briefly summarizing D06: the entropy values we measure at each radius are dominated by the most X-ray luminous component, which is generally the lowest entropy gas at that radius. For the best-fit entropy values to be significantly changed, the volume filling fraction of a higher-entropy component must be non-trivial ($> 50\%$). As discussed in D06, our results are not strongly affected by the presence of multiple, low-luminosity gas phases and are mostly insensitive to X-ray surface brightness decrements, such as X-ray cavities and bubbles, although in extreme cases their influence on an entropy profile can be detected (for an example, see the cluster A2052, also analyzed in D06).

Each entropy profile was fit with two models: a simple model which is a power-law at large radii and approaches a constant value at small radii (eq. 4), and a model which is a power-law only (eq. 5):

$$K(r) = K_0 + K_{100} \left(\frac{r}{100 \text{ kpc}} \right)^\alpha \quad (4)$$

$$K(r) = K_{100} \left(\frac{r}{100 \text{ kpc}} \right)^\alpha. \quad (5)$$

In our entropy models, K_0 is what we call core entropy, K_{100} is a normalization for entropy at 100 kpc, and α is the power-law index. Later in this paper, and in Cavagnolo et al. (2008a), we focus much of our discussion on the parameter K_0 so it is worth clarifying what K_0 does not represent. K_0 is not intended to represent the minimum core entropy or the entropy at $r = 0$. Nor does K_0 capture the gas entropy which would be measured immediately around an AGN or in a compact but extended BCG X-ray corona. Instead, K_0 represents the typical excess of core entropy above the best fitting power-law at larger radii. The intentionally simplistic characterization of cluster core entropy via K_0 was implemented to make comparing a large sample of cluster cores less ambiguous. The entropy models were fitted to the data using Craig Markwardt’s IDL routines in the package MPFIT. The

output best-fit parameters and associated errors were checked using a bootstrap Monte Carlo analysis of 5000 entropy profile realizations.

The radial range of fitting was truncated at a maximum radius (determined by eye) to avoid the influence of noisy bins and profile turnover at large radii which result from instability of our deprojection method. All the best-fit parameters for each cluster are listed in Table 5. The mean best-fit parameters for the full *ACCEPT* sample are given in Table 4. Also given in Table 4 are the mean best-fit parameters for clusters below and above $K_0 = 50 \text{ keV cm}^2$. We show in §5.2 that the cut at $K_0 = 50 \text{ keV cm}^2$ is not completely arbitrary as it approximately demarcates the division between two distinct populations in the K_0 distribution.

Some clusters have a surface brightness profile which is comparable to a double β -model. Our models for the behavior of $K(r)$ are intentionally simplistic and are not intended to fully describe all the features of $K(r)$. Thus, for the small number of clusters with discernible double- β behavior, fitting of the entropy profiles was restricted to the innermost of the two β -like features. These clusters have been flagged in Table 1 with the note letter ‘b.’ The best-fit power-law index is typically much steeper for these clusters, but the outer regions, which we do not discuss here, have power-law indices which are typical of the rest of the sample, *i.e.* $\alpha \sim 1.2$.

3.5. Exclusion of Central Sources

For many clusters in our sample the ICM X-ray peak, ICM X-ray centroid, BCG optical emission, and BCG infrared emission are coincident or well within 70 kpc of one another. This made identification of the cluster center unambiguous in those cases. However, in some clusters, there is an X-ray point source or compact X-ray source ($r \lesssim 5 \text{ kpc}$) found very near ($r < 10 \text{ kpc}$) the cluster center and always associated with a galaxy. We identified 37 clusters with central sources and have flagged them in Table 1 with the note letter ‘d’ for AGN and ‘e’ for compact but resolved sources. The mean best-fit parameters for these clusters are given in Table 4 under the sample name ‘CSE’ for “central source excluded.” These clusters cover the redshift range $z = 0.0044 - 0.4641$ with mean $z = 0.1196 \pm 0.1234$, and temperature range $kT_X = 1 - 12 \text{ keV}$ with mean $kT_X = 4.43 \pm 2.53 \text{ keV}$. For some objects – such as 3C 295, A2052, A426, Cygnus A, Hydra A, or M87 – the source is an AGN and there was no question the source must be removed.

However, determining how to handle the compact X-ray sources was not so straightforward. These compact sources are larger than the PSF, fainter than an AGN, but typically

have significantly higher surface brightness than the surrounding ICM such that the compact source’s extent was distinguishable from the ICM. These sources are most prominent, and thus the most troublesome, in non-cool core clusters (*i.e.* clusters which are approximately isothermal). They are troublesome because the compact source is typically much cooler and denser than the surrounding ICM and hence has an entropy much lower than the ambient ICM. We believe most of these compact sources to be X-ray coronae associated with the BCG (see Sun et al. 2007, for discussion of BCG coronae).

Without removing the compact sources, we measured radial entropy profiles and found, for all cases, that $K(r)$ abruptly changes at the outer edge of the compact source. Including the compact sources in the measurement of $K(r)$ results in the central cluster region(s) appearing overdense, and at a given temperature the region will have a much lower entropy than if the source were excluded. Such a discontinuity in $K(r)$ results in our simple models of $K(r)$ not being a good description of the profiles. Aside from producing poor fits, a significantly lower entropy influences the value of best-fit parameters because the shape of $K(r)$ is drastically changed. Obviously, two solutions are available: exclude or keep the compact sources during analysis. Deciding what to do with these sources depends upon what cluster properties we are specifically interested in quantifying.

The compact X-ray sources discussed in this section are not representative of the cluster’s core entropy; these sources are representative of the entropy within and immediately surrounding peculiar BCGs. Our focus for the *ACCEPT* project was to quantify the entropy structure of the cluster core region and surrounding ICM, not to determine the minimum entropy of cluster cores or to quantify the entropy of peculiar core objects such as BCG coronae. Thus, we opted to exclude these compact sources during our analysis. For a few extraordinary sources, it was simpler to ignore the central bin of the surface brightness profile during analysis because of imperfect exclusion of a compact source’s extended emission. These clusters have been flagged in Table 1 with the note letter ‘f.’

It is worth noting that when any source is excluded from the data, the empty pixels where the source once was were not included in the calculation of the surface brightness (counts and pixels are both excluded). Thus, the decrease in surface brightness of a bin where a source has been removed is not a result of the count to area ratio being artificially reduced.

4. Systematics

Our models for $K(r)$ were designed so that the best-fit K_0 values are a good measure of the entropy profile flattening at small radii. This flattening could potentially be altered through the effects of systematics such as PSF smearing and binning of the surface brightness profile. To quantify the extent to which our K_0 values are being affected by these systematics, we have analyzed mock *Chandra* observations created using the ray-tracing program MARX⁶, and also by analyzing degraded entropy profiles generated from artificially red-shifting well-resolved clusters. In the analysis below, we show that the lack of clusters with $K_0 \lesssim 10 \text{ keV cm}^2$ at $z \gtrsim 0.1$ is attributable to resolution effects, but that deviation of an entropy profile from a power-law, even if only in the central-most bin, cannot be accounted for by PSF effects. We also discuss the number of profiles which are reasonably well-represented by the power-law only profile, and establish that no more than $\sim 10\%$ of the entropy profiles in *ACCEPT* are consistent with a power-law.

4.1. PSF Effects

To assess the effect of PSF smearing on our entropy profiles, we have updated the analysis presented in §4.1 of D06 to use MARX simulations. In the D06 analysis, we assumed the density and temperature structure of the cluster core obeyed power-laws with $n_e \propto r^{-1}$ and $T_X \propto r^{1/3}$. This results in a power-law entropy profile with $K \propto r$. Further assuming the main emission mechanism is thermal bremsstrahlung, *i.e.* $\epsilon_X \propto T_X^{1/2}$, yields a surface brightness profile which has the form $S_X \propto r^{-5/6}$. A source image consistent with these parameters was created in IDL and then input to MARX to create the mock *Chandra* observations.

The MARX simulations were performed using the spectrum of a 4.0 keV, $0.3 \approx Z_\odot$ abundance MEKAL model. We have tested using input spectra with $kT_X = 2 - 10 \text{ keV}$ with varying abundances and find the effect of temperature and metallicity on the distribution of photons in MARX to be insignificant for our discussion here. We have neglected the X-ray background in this analysis as it is overwhelmed by cluster emission in the core and is only important at large radii. Observations for both ACIS-S and ACIS-I instruments were simulated using an exposure time of 40 ksec. A surface brightness profile was then extracted from the mock observations using the same $5''$ bins used on the real data.

For $5''$ bins, we find the difference between the central bins of the input surface brightness

⁶<http://space.mit.edu/CXC/MARX/>

and the output MARX observations to be less than the statistical uncertainty. One should expect this result, as the on-axis *Chandra* PSF is $\lesssim 1''$ and the surface brightness bins we have used on the data are five times this size. What is most interesting and important though, is that our analysis using MARX suggests any deviation of the surface brightness – and consequently the entropy profile – from a power-law, even if only in the central bin, is real and cannot be attributed to PSF effects. Even for the most poorly resolved clusters, the deviation away from a power-law we observe in a large majority of our entropy profiles is not a result of our deprojection technique or systematics.

4.2. Angular Resolution Effects

Another possible limitation in measuring K_0 is the effect of using discrete, fixed angular size bins when extracting surface brightness profiles. This choice may introduce a redshift-dependence into the best-fit K_0 values because as redshift increases, a fixed angular size encompasses a larger physical volume and the value of K_0 may increase if the bin includes a broad range of gas entropy. Shown in Figure 3 is a plot of the best-fit K_0 values for our entire sample versus redshift.

In the full archival sample, we have a few nearby objects ($z < 0.02$) with $K_0 < 10 \text{ keV cm}^2$ (numbered in Fig. 3) and only one at higher redshift – A1991 ($K_0 = 1.53 \pm 0.32$, $z = 0.0587$), which is a very peculiar cluster (Sharma et al. 2004). These low- z , low- K_0 group-scale objects have been included in our archival sample because they are well-known. Ignoring those systems, one can see from Fig. 3 that out to $z \approx 0.5$ clusters with $K_0 \geq 10 \text{ keV cm}^2$ are found at all redshifts. The completeness down to $K_0 \approx 10 \text{ keV cm}^2$ at most redshifts combined with the low- K_0 nearby systems raises the question: could the lack of clusters with $K_0 \lesssim 10 \text{ keV cm}^2$ at $z > 0.02$ be plausibly explained by resolution effects?

To investigate this question we tested the effect redshift has on our measurements of K_0 by culling out the subsample of objects with $K_0 \leq 10 \text{ keV cm}^2$ and $z \leq 0.1$ and degrading their surface brightness profiles to mimic the effect of increasing the cluster redshift. Our test is best illustrated using an example: consider a cluster at $z = 0.1$. For this cluster, $5'' \approx 9 \text{ kpc}$. Were the cluster at $z = 0.2$, $5''$ would be $\approx 17 \text{ kpc}$. To mimic moving this example cluster from $z = 0.1 \rightarrow 0.2$, we can extract a new surface brightness profile using a bin size of 17 kpc instead of $5''$. This procedure will result in a new surface brightness profile which has the angular resolution for a cluster at a higher redshift, and subsequent analysis of the entropy profile should yield information about how redshift affects the best-fit K_0 . The preceding method was used to degrade the profiles of the $K_0 \leq 10 \text{ keV cm}^2$ and $z \leq 0.1$ subsample objects. New surface-brightness bin sizes were calculated for each cluster over an

evenly distributed grid of redshifts in the range $z = 0.1 - 0.4$ using step sizes of 0.02.

Our temperature profiles were created using a minimum number of counts per annulus. Hence, clusters with peaked central surface brightness will have higher resolution temperature profiles. Thus, in addition to degrading the surface brightness profiles, the temperature profiles for each cluster were degraded by starting at the innermost temperature profile annulus and combining neighboring annuli moving outward. For each 0.1 step in our redshift grid the number of annuli which were combined was increased. For $z = 0.1$ two neighboring annuli were combined, for $z = 0.2$ three annuli were combined, for $z = 0.3$ four annuli, and five annuli at $z = 0.4$. In concordance with our criterion for creating the original temperature profiles, the number of annuli in the degraded profiles was not allowed to fall below 3. New spectra were extracted for these enlarged regions and analyzed following the same procedure detailed in §3.1.

The ensemble of artificially redshifted clusters was analyzed using the procedure outlined in §3.4. As artificial redshift increases, the number of radial bins decreases while the size of each bin increases. Fewer radial bins results in a less detailed sampling of an entropy profile’s overall curvature, while the larger bins mask the entropy-profile flattening because each bin, particularly the bins nearest the elbow of an entropy profile, encompass a broad range of entropy. Over the redshift range $z = 0.1 - 0.3$, the increased size of the radial bins (and hence broader range of entropy per bin) dominates, resulting in entropy profiles which have obvious flattened cores, but the entropy measured in each bin has increased. Consequently, best-fit K_0 also increases, on average, as $(K'_0 - K_0)/K_0 = 2.12 \pm 1.84$ where K_0 is the original best-fit value and K'_0 is the best-fit value of the degraded profiles. But, when $z > 0.3$, the degraded entropy profiles severely under sample both the core flattening and overall profile curvature, resulting in most entropy profiles resembling power-laws with a centralmost bin that deviates only slightly from the power-law at larger radii. This translates into a modest increase of best-fit K_0 which, on average, is $(K'_0 - K_0)/K_0 = 0.71 \pm 0.57$. However, there is a caveat to our analysis of the degraded entropy profiles: the size of the region over which the original entropy profiles flatten is not uniform. Hence, for clusters with small flattened cores ($r \lesssim 20$ kpc), degradation of the profiles will more quickly mask out the flattening, and vice versa for the clusters with large cores. It is also worth noting that as redshift increases the best-fit power law indices (α) become shallower (*i.e.* significantly less than 1.1), the errors on K_0 and α increase, and based on χ^2 , the power-law only model fits drastically improve – though it is still not a better fit than the model with K_0 .

4.3. Profile Curvature, Number of Bins, and Exposure Time

Our analysis of the degraded entropy profiles suggests that K_0 is more sensitive to the value of $K(r)$ in the central bins than it is to the shape of the profile or the number of radial bins. However, for completeness we investigate in this section: (1) if there is a correlation between best-fit K_0 and the curvature of an entropy profile, and (2) if the number of radial bins correlates with best-fit K_0 . A systematic correlation of K_0 with these quantities means the estimates of K_0 might be biased by, for example, the curvature of the temperature profile outside the core or by the signal-to-noise of an observation.

To check for a possible correlation between best-fit K_0 and profile curvature we first calculated average profile curvatures, κ_A . For each profile, κ_A was calculated using the standard formulation for the curvature of a function, $\kappa = \|y''\|/(1 + y'^2)^{3/2}$, where we set $y = K(r) = K_0 + K_{100}(r/100 \text{ kpc})^\alpha$. This derivation yields,

$$\kappa_A = \frac{\int \frac{\|100^{-\alpha}(\alpha-1)\alpha K_{100}r^{\alpha-2}\|}{[1+(100^{-\alpha}\alpha K_{100}r^{\alpha-1})^2]^{3/2}} dr}{\int dr} \quad (6)$$

where α and K_{100} are the best-fit parameters unique to each entropy profile. The integral over all space ensures we evaluate the curvature of each profile in the limit where the profiles have asymptotically approached a constant at small radii and a power law at large radii. We find that at any value of K_0 a large range of curvatures are covered and that there is no systematic trend in K_0 associated with κ_A (top left panel of Fig. 4). In addition, plots of best-fit K_0 versus the number of bins fit in each entropy profile do not reveal any trends, only scatter (top right panel of Fig. 4).

Our temperature profiles were created using a minimum number of counts per annulus criterion. One can therefore ask if the length of an observation or the number of bins in the temperature profile correlates with best-fit K_0 . Shown in the bottom left and right panels of Fig. 4 are K_0 versus the total used exposure time for that cluster and K_0 versus number of bins in the temperature profile, respectively. We do not find trends with K_0 in either comparison.

As expected, we do not find any systematic trends with profile shape, number of bins fit in $K(r)$, exposure time, or number of bins in $T_X(r)$ which would significantly affect our best-fit K_0 values. Thus, we conclude that the K_0 values discussed in this paper are, as intended, an adequate measure of the core entropy, and that any undetected dependence of K_0 on profile shape or radial resolution affect our results at significance levels much smaller than the measured uncertainties.

4.4. Power-law Profiles

Equation 4 is a special case of eq. 5 with $K_0 = 0$, meaning that the models we fit to $K(r)$ are nested. A comparison between the p-values (shown in Table 5) of each cluster’s best-fit models shows which model exhibits more agreement with the data. In addition, for each fit in Table 5 we show the deviation in units of sigma, σ_{K_0} , of the best-fit K_0 value from zero. We also show in Table 4 the number of clusters and the percentage of the sample which have a K_0 statistically consistent with zero at various confidence levels. Table 4 shows that at the 3σ significance level $\sim 10\%$ of the full *ACCEPT* sample has a best-fit K_0 value which is consistent with zero. Moreover, that there is a systematic trend for a single power-law to be a poor fit mainly at the smallest radii suggests non-zero K_0 is not random.

5. Results and Discussion

Presented in Figure 5 is a montage of *ACCEPT* entropy profiles for different temperature ranges. These figures highlight the cornerstone result of *ACCEPT*: a uniformly analyzed collection of entropy profiles covering a broad range of core entropy. Each profile is color-coded to represent the global cluster temperature. Plotted in each panel of Fig. 5 are the mean profiles representing $K_0 \leq 50 \text{ keV cm}^2$ clusters (dashed-line) and $K_0 > 50 \text{ keV cm}^2$ clusters (dashed-dotted line), in addition to the pure-cooling model of Voit et al. (2002) (solid black line). The theoretical pure-cooling curve represents the entropy profile of a 5 keV cluster simulated with radiative cooling but no feedback and gives us a useful baseline against which to compare *ACCEPT* profiles.

In the following sections we discuss results gleaned from analysis of our library of entropy profiles. These results include the departure of most entropy profiles from a simple radial power-law profile, the bimodal distribution of core entropy, and the asymptotic convergence of the entropy profiles to the self-similar $K(r) \propto r^{1.1-1.2}$ power-law at $r \geq 100 \text{ kpc}$.

5.1. Non-Zero Core Entropy

Arguably the most striking feature of Figure 5 is the departure of most profiles from a simple power-law. Core flattening of surface brightness profiles (and consequently density profiles) is a well known feature of clusters (*e.g.* Jones & Forman 1984, Mohr et al. 1999 and Xue & Wu 2000). What is notable in our work however is that, based on comparison of reduced χ^2 and significance of K_0 , very few of the clusters in our sample have an entropy distribution which is best-fit by the power-law only model (eq. 5), rather they are sufficiently

well-described by the model which flattens in the core (eq. 4).

For clusters with central cooling times shorter than the age of the cluster, non-zero core entropy is an expected consequence of episodic heating of the ICM (Voit & Donahue 2005), with AGN as one possible heating source (Bower 1997; Loewenstein 2000; Voit & Bryan 2001; Soker et al. 2001; Churazov et al. 2002; Brüggen & Kaiser 2002; Brüggen et al. 2002; Nath & Roychowdhury 2002; Ruszkowski & Begelman 2002; Alexander 2002; Omma et al. 2004; McCarthy et al. 2004; Roychowdhury et al. 2004; Hoeft & Brüggen 2004; Dalla Vecchia et al. 2004; Soker & Pizzolato 2005; Pizzolato & Soker 2005; Brighenti & Mathews 2006; Mathews et al. 2006). Clusters with cooling times of order the age of the Universe, however, require other mechanisms to generate their core entropy, for example via mergers or extremely energetic AGN outbursts. For the very highest K_0 values, $K_0 > 100 \text{ keV cm}^2$, the mechanism by which the core entropy came to be so large is not well understood as it is difficult to boost the entropy of a gas parcel to $> 100 \text{ keV cm}^2$ via merger shocks (McCarthy et al. 2008) and would require AGN outburst energies which have never been observed. We are providing the data and results of *ACCEPT* to the public with the hope that the research community finds it a useful new resource to further understand the processes which result in non-zero cluster core entropy.

5.2. Bimodality of Core Entropy Distribution

The time required for a gas parcel to radiate away its thermal energy is a function of the gas entropy. Low entropy gas radiates profusely and is thus subject to rapid cooling, and vice versa for high entropy gas. Hence, the distribution of K_0 is of particular interest because it is an approximate indicator of the cooling timescale in the cluster core. The K_0 distribution is also interesting because it may be useful in better understanding the physical processes operating in cluster cores. For example, if processes such as thermal conduction and AGN feedback are important in establishing the entropy state of cluster cores, then models which properly incorporate these processes should approximately reproduce the observed K_0 distribution.

In the top panel of Figure 6 is plotted the logarithmically binned distribution of K_0 . In the bottom panel of Figure 6 is plotted the cumulative distribution of K_0 . One can immediately see from these distributions that there are at least two distinct populations separated by a smaller number of clusters with $K_0 \approx 30 - 50 \text{ keV cm}^2$. If the distinct bimodality of the K_0 distribution seen in the binned histogram were an artifact of binning, then the cumulative distribution should be relatively smooth. But, there is clearly a plateau in the cumulative distribution which coincides with the division between the two populations

at $K_0 \approx 30 - 50 \text{ keV cm}^2$. We have tested re-binning the K_0 histogram using the optimized binning techniques outlined in Knuth (2006) and Hogg (2008) and find no change in the bimodality or range of the gap in K_0 versus using naive fixed-width bins.

To further test for the presence of a bimodal population, we utilized the KMM test of Ashman et al. (1994). The KMM test estimates the probability that a set of data points is better described by the sum of multiple Gaussians than by a single Gaussian. We tested the unimodal case versus the bimodal case under the assumption that the dispersion of the two Gaussian components are not the same. We have used the updated KMM code of Waters et al. (2008) which incorporates bootstrap resampling to determine uncertainties for all parameters. A post-analysis comparison of fits assuming the populations have the same and different dispersions confirms our initial guess that the dispersions are different is a better model.

The KMM test, as with any statistical test, is very specific. At zeroth order, the KMM test simply determines if a population is unimodal or not, and finds the means of these populations. However, the dispersions of these populations are subject to the quality of sampling and the presence of outliers (*e.g.* KMM must assign all data points to a population). The outputs of the KMM test are the best-fit populations to the data, not necessarily the best-fit populations of the underlying distribution (hence no goodness of fit is output). However, the KMM test does output a p-value, and with the assumption that χ^2 describes the distribution of the likelihood ratio statistic, p is the confidence interval for the null hypothesis.

There are a small number of clusters with $K_0 \leq 4 \text{ keV cm}^2$ that when included in the KMM test significantly change the results. Thus, we conducted tests including and excluding $K_0 \leq 4 \text{ keV cm}^2$ clusters and provide two sets of best-fit parameters. The results of the bimodal KMM test neglecting $K_0 \leq 4 \text{ keV cm}^2$ clusters were two statistically distinct peaks at $K_1 = 17.8 \pm 6.6 \text{ keV cm}^2$ and $K_2 = 154 \pm 52 \text{ keV cm}^2$. 124 clusters were assigned to the first distribution, while 109 were assigned to the second. Including $K_0 \leq 4 \text{ keV cm}^2$ clusters, the bimodal KMM test found populations at $K_1 = 15.0 \pm 5.0 \text{ keV cm}^2$ (89 clusters) and $K_2 = 129 \pm 45 \text{ keV cm}^2$ (136 clusters). The bimodal KMM test neglecting $K_0 \leq 4 \text{ keV cm}^2$ clusters returned $p = 1.16 \times 10^{-7}$, while the test including all clusters returned $p = 1.90 \times 10^{-13}$. These tiny p -values indicate the unimodal distribution is significantly rejected as the parent distribution of the observed K_0 distribution. We also checked for bimodality as a function of redshift by making cuts in redshift space and running the KMM test using each new distribution. The KMM test indicated that two statistically distinct populations were not present when the redshift range was restricted to clusters with $z > 0.4$. For all other redshift cuts the K_0 distribution was bimodal. There are 20 clusters with $z > 0.4$, and we suspected

this was too few clusters to detect two populations. As a test, we randomly selected 20 clusters from our full sample 1000 times and ran the KMM test. A bimodal population was found in 2% of the trials, suggesting the lack of bimodality at $z > 0.4$ is a result of poor statistics.

We pointed out in §3.4 that for some clusters in our archival sample, the different interpolation schemes for the centralmost bins of the cluster temperature profiles yielded significantly different K_0 values (see Fig. 2). Using the K_0 values derived using temperature profiles which were allowed to decline in the centralmost bins (see §3.4), we repeated the above analysis checking for bimodality. We find that bimodality is present using these K_0 values and that the best-fit values from the KMM test are not significantly different for either scheme. Our result of finding bimodality in the K_0 population is robust to the choice of temperature profile interpolation scheme.

One possible explanation for a bimodal core entropy distribution is that it arises from the effects of episodic AGN feedback and electron thermal conduction in the cluster core. Voit & Donahue (2005) outlined a model of AGN feedback whereby outbursts of $\sim 10^{45}$ ergs s^{-1} occurring every $\sim 10^8$ yrs can maintain a quasi-steady core entropy of $\approx 10 - 30$ keV cm^2 . In addition, very energetic and infrequent AGN outbursts of $\geq 10^{61}$ ergs can increase the core entropy into the $\approx 30 - 50$ keV cm^2 range (Voit & Donahue 2005). This model of AGN feedback satisfactorily explains the distribution of $K_0 \lesssim 50$ keV cm^2 , but depletion of the $K_0 = 30 - 50$ keV cm^2 region and populating $K_0 > 50$ keV cm^2 requires more physics. Voit et al. (2008) have recently suggested that the dramatic fall-off of clusters beginning at $K_0 \approx 30$ keV cm^2 may be the result of electron thermal conduction. After K_0 has exceeded ≈ 30 keV cm^2 , conduction could severely slow, if not halt, a cluster's core from appreciably cooling and returning to a core entropy state with $K_0 < 30$ keV cm^2 . Merger shocks can then readily raise K_0 values to $\gtrsim 100$ keV cm^2 . This model is supported by results presented in Cavagnolo et al. (2008a), Guo et al. (2008), and Rafferty et al. (2008) which find that the formation of thermal instabilities and signatures of ongoing feedback and star formation are extremely sensitive to the core entropy state of a cluster.

We acknowledge that *ACCEPT* is not a complete, uniformly selected sample of clusters. This raises the possibility that our sample is biased towards clusters that have historically drawn the attention of observers, such as cooling flows or mergers. If that were the case, then one reasonable explanation of the K_0 bimodality is that $K_0 = 30 - 50$ keV cm^2 clusters have not been the focus of much scientific interest and thus go unobserved. However, as we show in §5.4, the complete flux-limited *HIFLUGCS* sample is also bimodal. Nevertheless, flux-limited samples do suffer from some inadequacies and further study of a carefully selected sample of clusters, chosen either from our own archival sample or using representative, rather

than complete, samples such as REXCESS (Böhringer et al. 2007), may be warranted.

5.3. The *HIFLUGCS* Sub-Sample

ACCEPT is not a flux-limited or volume-limited sample. To ensure our results are not affected by an unknown selection bias, we culled the *HIFLUGCS* sample from *ACCEPT* for separate analysis. *HIFLUGCS* is a flux-limited sample ($f_X \geq 2 \times 10^{-11}$ ergs s $^{-1}$ cm $^{-2}$) selected from the *REFLEX* sample (Böhringer et al. 2004) with no consideration of morphology. Thus, at any given luminosity in *HIFLUGCS* there is a good sampling of different morphologies, *i.e.* possible bias toward cool-core clusters or mergers has been removed. The sample also covers most of the sky with holes near Virgo and the Large and Small Magellanic Clouds, and has no known incompleteness (Chen et al. 2007). There are a total of 106 objects in *HIFLUGCS*: 63 in the primary sample and 43 in the extended sample. Of these 106 objects, no public *Chandra* observations were available for 16 objects (A548e, A548w, A1775, A1800, A3528n, A3530, A3532, A3560, A3695, A3827, A3888, AS0636, HCG 94, IC 1365, NGC 499, RXCJ 2344.2-0422), 6 objects did not meet our minimum analysis requirements and were thus insufficient for study (3C 129, A1367, A2634, A2877, A3627, Triangulum Australis), and as discussed in §2, Coma and Fornax were intentionally ignored. This left a total of 82 *HIFLUGCS* objects which we analyzed, 59 from the primary sample ($\sim 94\%$ complete) and 23 from the extended sample ($\sim 50\%$ complete). The primary sample is the more complete of the two, thus we focus our following discussion on the primary sample only.

The clusters missing from the primary *HIFLUGCS* sample are A1367, A2634, Coma, and Fornax. The extent to which these 4 clusters can change our analysis of the K_0 distribution for *HIFLUGCS* is limited. To alter or wash-out bimodality, all 4 clusters would need to fall in the range $K_0 = 30 - 50$ keV cm 2 , which is certainly not the case for any of these clusters. A1367 has been studied by Donnelly et al. (1998) and Sun & Murray (2002), with both finding that two sub-clusters are merging in the cluster. The merger process, and the potential for associated shock formation, is known to create large increases of gas entropy (McCarthy et al. 2007). Given the combination of low surface brightness, moderate temperatures ($kT_X = 3.5 - 5.0$ keV), lack of a temperature gradient, ongoing merger, and presence of a shock, it is unlikely A1367 has a core entropy $\lesssim 50$ keV cm 2 . A2634 is a very low surface brightness cluster with the bright radio source 3C 465 at the center of an X-ray corone (Sun et al. 2007). Clusters with comparable properties to A2634 are not found to have $K_0 \lesssim 50$ keV cm 2 . Coma and Fornax are known to have core entropy > 50 keV cm 2 (Rafferty et al. 2008).

Shown in Figure 7 are the log-binned (top panel) and cumulative (bottom panel) K_0 distributions of the *HIFLUGCS* primary sample. The bimodality seen in the full *ACCEPT* collection is also present in the *HIFLUGCS* sub-sample. Mean best-fit parameters are given in Table 4. We again performed two KMM tests: one test with, and another test without, clusters having $K_0 \leq 4 \text{ keV cm}^2$. For the test including $K_0 \leq 4 \text{ keV cm}^2$ clusters we find populations at $K_1 = 9.7 \pm 3.5 \text{ keV cm}^2$ (28 clusters) and $K_2 = 131 \pm 46 \text{ keV cm}^2$ (31 clusters) with $p = 3.34 \times 10^{-3}$. Excluding clusters with $K_0 \leq 4 \text{ keV cm}^2$ we find peaks at $K_1 = 10.5 \pm 3.4 \text{ keV cm}^2$ and $K_2 = 116 \pm 42 \text{ keV cm}^2$, each having 21 and 34 clusters, respectively, and $p = 1.55 \times 10^{-5}$.

Hudson & Reiprich (2007) note a similar core entropy bimodality to the one we find here. Hudson & Reiprich (2007) discuss two distinct groupings of objects in a plot of average cluster temperature versus core entropy, with the dividing point being $K \approx 40 \text{ keV cm}^2$. Our results agree with the findings of Hudson & Reiprich (2007). While the gaps of *ACCEPT* and *HIFLUGCS* do not cover the same K_0 range, it is interesting that both gaps appear to be the deepest around $K_0 \approx 30 \text{ keV cm}^2$. That bimodality is present in both *ACCEPT* and the unbiased *HIFLUGCS* sub-sample suggests bimodality is not the result of simple archival bias.

5.4. Distribution of Core Cooling Times

In the X-ray regime, cooling time and entropy are related in that decreasing gas entropy also means shorter cooling time. Thus, if the K_0 distribution is bimodal, the distribution of cooling times should also be bimodal. We have calculated cooling time profiles from the spectral analysis using the relation

$$t_{\text{cool}} = \frac{3nkT_X}{2n_e n_H \Lambda(T, Z)} \quad (7)$$

where n is the total number density ($\approx 2.3n_H$ for a fully ionized plasma), n_e and n_H are the electron and proton densities respectively, $\Lambda(T, Z)$ is the cooling function for a given temperature and metal abundance, and $3/2$ is a constant associated with isochoric cooling. The values of the cooling function for each temperature profile bin were calculated in XSPEC using the flux of the best-fit spectral model. Following the procedure discussed in §3.4, Λ and kT_X were interpolated across the radial grid of the electron density profile. The cooling time profiles were then fit with a simple model analogous to that used for fitting $K(r)$:

$$t_{\text{cool}}(r) = t_{c0} + t_{100} \left(\frac{r}{100 \text{ kpc}} \right)^\alpha \quad (8)$$

where t_{c0} is core cooling time and t_{100} is a normalization at 100 kpc.

The K_0 distribution can also be used to explore the distribution of core cooling times. Assuming free-free interactions are the dominant gas cooling mechanism (*i.e.* $\epsilon \propto T^{1/2}$), Donahue et al. (2005) show that entropy is related to cooling time via the formulation:

$$t_{c0}(K_0) \approx 10^8 \text{ yrs} \left(\frac{K_0}{10 \text{ keV cm}^2} \right)^{3/2} \left(\frac{kT_X}{5 \text{ keV}} \right)^{-1}. \quad (9)$$

Shown in Figure 8 is the logarithmically binned and cumulative distributions of best-fit core cooling times from eq. 8 (top panel) and core cooling times calculated using eq. 9 (bottom panel). The bin widths in both histograms are 0.20 in log-space. The pile-up of cluster core cooling times below 1 Gyr is well known, for example in Hu et al. (1985) or more recently in Dunn & Fabian (2008). In addition, the core cooling times we calculate are consistent with the results of other cooling time studies, such as Peres et al. (1998) or Rafferty et al. (2008). However, what is most important about Fig. 8 is that the distinct bimodality of the K_0 distribution is also present in best-fit core cooling time, t_{c0} . A KMM bimodality test using t_{c0} found peaks at $t_{c1} = 0.60 \pm 0.24$ Gyr and $t_{c2} = 6.23 \pm 2.19$ Gyr with 132 and 101 objects in each respective population. The probability that the unimodal distribution is a better fit was once again exceedingly small, $p = 8.77 \times 10^{-7}$.

The bimodality we observe in the cooling-time distribution is not as pronounced as what we see in the K_0 distribution, suggesting that the bimodality in entropy might be easier to observe. Since cooling time profiles are more sensitive to the resolution of the temperature profiles than are the entropy profiles, it may be that resolution effects more seriously limit the quantification of the true cooling time of the core. For example, if our temperature interpolation scheme is too coarse, or averaging over many small-scale temperature fluctuations significantly increases t_{c0} , then t_{c0} would not be the best approximation of true core cooling time. In which case, the core cooling times might be shorter and the sharpness and offset of the distribution gaps may not be as distinct.

5.5. Slope and Normalization of Power-law Components

Beyond $r \approx 100$ kpc the entropy profiles show a striking similarity in the slope of the power-law component which is independent of K_0 . For the full sample, the mean value of the power-law normalization at large radii, $\alpha = 1.21 \pm 0.39$. For clusters with $K_0 < 50 \text{ keV cm}^2$, the mean $\alpha = 1.20 \pm 0.38$, and for clusters with $K_0 \geq 50 \text{ keV cm}^2$, the mean $\alpha = 1.23 \pm 0.40$. Our mean slope of $\alpha \approx 1.2$ is not statistically different from the theoretical value of $\alpha = 1.1$ found by Tozzi & Norman (2001) using semi-analytic models and $\alpha = 1.2$ found by Voit

et al. (2005) using models with gravitational effects only. For the full sample, the mean value of $K_{100} = 126 \pm 45 \text{ keV cm}^2$. Again distinguishing between clusters below and above $K_0 = 50 \text{ keV cm}^2$, we find $K_{100} = 150 \pm 50 \text{ keV cm}^2$ and $K_{100} = 107 \pm 39 \text{ keV cm}^2$, respectively. Scaling each entropy profile by the cluster virial temperature and virial radius considerably reduces the dispersion in K_{100} , but we reserve detailed discussion of scaling relations for a future paper.

5.6. Comparison of *ACCEPT* with Other Entropy Studies

5.6.1. Studies Using *XMM-Newton*

In §4.2 we presented our analysis of the angular resolution effects on entropy profiles. In addition to the analysis shown there, we chose to evaluate the extent to which *XMM-Newton*’s comparatively lower angular resolution might be the reason entropy profiles appeared to be power laws in previous studies. Thus, we have also performed the degradation analysis presented in §4.2 on all clusters which have a published entropy profile derived using *XMM-Newton* data and have been observed with *Chandra*. These clusters are: 2A 0335+096, A262, A399, A426, A478, A496, A1068, A1413, A1795, A1835, A1991, A2034, A2052, A2204, A2597, A2717, A3112, A4059, Hydra A, MKW3S, PKS 0745-191, and Sersic 159-03. These clusters are taken primarily from two studies, Piffaretti et al. (2005) and Pratt et al. (2006), below we briefly highlight some of the important analysis methods used in these two studies.

In Piffaretti et al. (2005) they used *XMM-Newton* data for a sample of 17 cooling flow clusters in the temperature range $kT_X = 1 - 7 \text{ keV}$ taken from Kaastra et al. (2004). The entropy profiles presented in Piffaretti et al. (2005) were derived using PSF-corrected, de-projected spectral analysis presented in Kaastra et al. (2004). The temperature and density profiles were generated using approximately 8 radial annuli per cluster, where the spectral analysis was restricted to the energy range 0.2-10.0 keV. Hence, the Piffaretti et al. (2005) analysis was on a much coarser angular scale than is presented in *ACCEPT*. Piffaretti et al. (2005) found no isentropic cores for their sample, that the entropy profiles increased monotonically outward, and that the profiles had a mean power law index of $\alpha = 0.95 \pm 0.02$, which is much shallower than the mean α we find in *ACCEPT*. However, *XMM-Newton*’s angular resolution limited the radial analysis to no less than $0.01r_{\text{virial}}$, and Piffaretti et al. (2005) did find the dispersion of entropy in the central-most bins to be greater than at larger radii, a strong indicator that profile flattening in the core was not resolved.

Pratt et al. (2006) used a sample of 10 relaxed systems observed with *XMM-Newton* at

$z < 0.2$ with temperatures in the range $kT_X \approx 2.5 - 8$ keV. Entropy profiles were derived by Pratt et al. (2006) using PSF-corrected, deprojected temperature profiles and gas density profiles calculated from an analytical model fit to PSF deconvolved surface brightness profiles presented in Pointecouteau et al. (2005). The analytics models used by Pointecouteau et al. (2005) were a double β -model, β -model modified to allow for more centrally concentrated gas densities, and a triple β -model with all components having a common β value. The temperature profiles had bin sizes of at least $15''$. Use of the surface brightness models by Pratt et al. (2006) in deriving $K(r)$ places their entropy profiles on an angular scale which is close to our work. Like Piffaretti et al. (2005), Pratt et al. (2006) found no isentropic cores and that all their profiles increased monotonically outward. However, Pratt et al. (2006) do note that, “the slope of the [entropy] profile becomes shallower towards the centre in some of the clusters.” This suggests that had a power-law model with a core term, such as K_0 , been used, the flattening might have been detected (a point addressed further in the next paragraph). Pratt et al. (2006) did however find $< 20\%$ dispersion in entropy at $r > 0.1r_{200}$ and $> 60\%$ dispersion at $r \sim 0.02r_{200}$ in addition to a mean power law index of $\alpha = 1.08 \pm 0.04$. Again, both of these results are consistent with unresolved flattened cores.

After repeating the degradation analysis presented in §4.2 using the subsample of clusters which have published entropy profiles derived from *XMM-Newton* data, we note several important results:

1. When the degradation procedure produced profiles with approximately the same angular resolution as *XMM-Newton*, our entropy profiles are mostly, though not all, very similar to power-laws. Only the clusters with the largest flattened cores (*e.g.* 2A0335, Sersic159, A1413) still had noticeable curvature, while in contrast, clusters with the smallest cores (*e.g.* A3112, A1991, A4059) were as well fit by the power-law model as a model with K_0 . It is worth noting that the aforementioned *XMM-Newton* studies which utilized the PSF deconvolution of Croston et al. (2006) should successfully recover the core properties of most clusters. Thus, this result of small, flattened entropy cores being washed out at angular resolutions comparable to that of *XMM-Newton*~~s~~ ~~should be interpreted in the context of only applying~~ to those *XMM-Newton* results which did not utilize PSF deconvolution.
2. *XMM-Newton* profiles from the literature have, on average, higher entropy values per radial bin, specifically in the core region, than our fiducial or slightly degraded entropy profiles. One should expect this result as, on average, the angular size of the bins we use for calculating density profiles is smaller, thus for a given cluster, each of our profile’s bins will encompass a narrower range of entropy than the bins of an *XMM-Newton* profile.

3. While *XMM-Newton* entropy profiles from the literature were all fit with power laws, during comparison with our degraded profiles, it appears that the published *XMM-Newton* profiles may not be intrinsically power laws. Upon close examination of some *XMM-Newton* profiles, ~~take~~ for example A2204 or A2597 in Pratt et al. (2006), the profiles clearly lie below the best-fit power law as they enter the cluster core and then flatten back out in the central bin.

In addition to the comparisons presented above, the primary differences between the work presented in this paper and that of previous *XMM-Newton* work is that we have considered the behavior of the temperature profile across the central temperature bin, and included a K_0 term in our fitting model to quantify entropy profile flattening.

5.6.2. General Comparison of Results

There are many published studies of ICM entropy, and in this section we compare the general trends we find with the results of a few other studies. The studies with which we compare our results are:

1. Lloyd-Davies et al. (2000): *ROSAT* and *ASCA* data for 20 bound galaxy systems in the redshift range $z \approx 0.08 - 0.2$ and temperature range $kT_X \approx 0.5 - 14$ keV was used in this study. Lloyd-Davies et al. (2000) clearly show flattened entropy profiles for clusters with $K(r) > 100$ keV cm² at $r \approx 0.01r_{\text{virial}}$, while below this limit they find the entropy profiles trend downward like power laws. As we showed in §4.2 using degraded *XMM-Newton* data, the finding of power-law entropy profile behavior at small radii is most likely the result of not resolving the small flattened entropy cores in cool core clusters.
2. Ponman et al. (2003): This study used a sample of 66 systems, observed with *ROSAT* and *ASCA*, in the redshift range $z = 0.0036 - 0.208$ and temperature range $kT_X = 0.5 - 17$ keV and was the largest sample with which we compared our results. In general, the entropy profiles presented by Ponman et al. (2003) flatten inside $0.1r_{200}$ irrespective of cluster temperature.
3. Morandi & Ettori (2007): Using *Chandra* data, this study examined 24 galaxy clusters with $kT_X > 6$ keV in the redshift range $z = 0.14 - 0.82$. Morandi & Ettori (2007) found the power law indices for various subsamples to be in the range $\alpha = 1 - 1.18$, and that all of the entropy profiles flatten at $r < 0.5r_{2500}$. They also found best-fit K_0 values in the range $20 - 300$ keV cm².

In general, we find good agreement between the properties of our entropy profiles and the profiles presented in the papers cited above, specifically that:

1. Cluster entropy profiles at $r \gtrsim 0.1r_{\text{virial}}$ are well described by an entropy distribution which goes as $K(r) \propto r^{1.1-1.2}$.
2. The core regions ($r \lesssim 0.1r_{\text{virial}}$) of clusters approach isentropic behavior as $r \rightarrow 0$, or in the cases where the observations do not resolve the core regions, the dispersion of entropy within the core region is considerably larger than the dispersion of the entropy at larger ($r \gtrsim 0.1r_{\text{virial}}$) radii.
3. The above two properties are seen in the entropy profiles of clusters over a large range of redshifts ($0.05 \lesssim z \lesssim 0.5$), temperatures ($0.5 \text{ keV} \lesssim kT_X \lesssim 15 \text{ keV}$), and luminosities ($10^{43-45} \text{ ergs s}^{-1}$).

6. Summary and Conclusions

We have presented intracluster medium entropy profiles for a sample of 239 galaxy clusters (9.86 Msec) taken from the *Chandra* Data Archive. We have named this project *ACCEPT* for “Archive of Chandra Cluster Entropy Profile Tables.” The reduced data products, data tables, figures, cluster images, and results of our analysis for all clusters and observations are freely available at the *ACCEPT* web site: <http://www.pa.msu.edu/astro/MC2/accept>. We encourage observers and theorists to utilize this library of entropy profiles in their own work.

We created radial temperature profiles using spectra extracted from a minimum of three concentric annuli containing 2500 counts each and extending to either the chip edge or $0.5r_{180}$, whichever was smaller. We deprojected surface brightness profiles extracted from $5''$ bins over the energy range 0.7-2.0 keV to obtain the electron gas density as a function of radius. Entropy profiles were calculated from the density and temperature profiles as $K(r) = T(r)n(r)^{-2/3}$. Two models for the entropy distribution were then fit to each profile: a power-law only model (eq. 5) and a power-law which approaches a constant value at small radii (eq. 4).

We have demonstrated that the entropy profiles for the majority of *ACCEPT* clusters are well-represented by the model which approaches a constant entropy, K_0 , in the core. The entropy profiles of *ACCEPT* are also remarkably similar at radii greater than 100 kpc, and asymptotically approach the self-similar pure-cooling curve ($r \propto 1.2$) with a slope of $\alpha = 1.21 \pm 0.39$ (the dispersion here is in the sample, not in the uncertainty of the measurement).

We also find that the distribution of K_0 for the full archival sample is bimodal with the two populations separated by a poorly populated region between $K_0 \approx 30 - 50 \text{ keV cm}^2$. After culling out the primary *HIFLUGCS* sub-sample of Reiprich (2001), we find the K_0 distribution of this complete sub-sample also to be bimodal, indicating that the bimodality we find in our larger sample does not result from archival bias.

When we compared our results with those of a few other entropy studies, specifically Lloyd-Davies et al. (2000), Ponman et al. (2003), Piffaretti et al. (2005), Pratt et al. (2006), and Morandi & Ettori (2007), we found the same general trends, noting however that Piffaretti et al. (2005) and Pratt et al. (2006) did not specifically find isentropic cores. However, those two studies did find large dispersion of entropy in the core region ($r < 0.1r_{\text{virial}}$), suggesting that *XMM-Newton* did not resolve the flattened entropy profiles we measure with the finer angular resolution of *Chandra*.

Two core cooling times were derived for each cluster: (1) cooling time profiles were calculated using eq. 7 and each cooling time profile was then fit with eq. 8 returning a best-fit core cooling time, t_{c0} ; (2) Using best-fit K_0 values, entropy was converted to a core cooling time, $t_{c0}(K_0)$ using eq. 9. We find the distributions of both core cooling times to be bimodal. Comparison of the core cooling times from method (1) and (2) reveals that the gap in the bimodal cooling time distributions occur over different timescales, $\sim 2 - 3 \text{ Gyrs}$ for t_{c0} , and $\sim 0.7 - 1$ for $t_{c0}(K_0)$, but this offset may be the result of resolution limitations.

After analyzing an ensemble of artificially redshifted entropy profiles, we find the lack of $K_0 \lesssim 10 \text{ keV cm}^2$ clusters at $z > 0.1$ is most likely a result of resolution effects. Investigation of possible systematics affecting best-fit K_0 values, such as profile curvature and number of profile bins, revealed no trends which would significantly affect our results. We came to the conclusion that K_0 is an acceptable measure of average core entropy and is not overly influenced by profile shape or radial resolution. We also find that $\sim 90\%$ of the sample clusters have a best-fit K_0 more than 3σ away from zero.

Our results regarding non-zero core entropy and K_0 bimodality support the sharpening picture of how feedback and radiative cooling in clusters alter global cluster properties and affect massive galaxy formation. Among the many models of AGN feedback, Voit & Donahue (2005) outlined a model which specifically addresses how AGN outbursts generate and sustain non-zero core entropy in the regime of $K_0 \lesssim 30 \text{ keV cm}^2$ (see also Kaiser & Binney 2003). In addition, if electron thermal conduction is an important process in clusters, then there exists a critical entropy threshold below which conduction is no longer efficient at wiping out thermal instabilities, the consequences of which should be a bimodal core entropy distribution and a sensitivity of cooling by-product formation (like star formation and AGN activity) to this entropy threshold (Voit et al. 2008; Guo et al. 2008). We show in Cavagnolo et al.

(2008a) that indicators of feedback like $H\alpha$ and radio emission are extremely sensitive to the lower bound of the gap in the bimodal distribution at $K_0 \approx 30 \text{ keV cm}^2$.

Many details are still missing from the emerging picture of the entropy life cycle in clusters, and there are many open questions regarding the evolution of the ICM and how thermal instabilities form in cluster cores. It is still unclear how clusters with very high core entropy ($K_0 > 100 \text{ keV cm}^2$) are produced. Is an early episode of preheating necessary? And while resolution has restricted our ability to investigate a possible evolution of K_0 with redshift (which would suggest evolution in the cool-core cluster population), there may be other observational proxies which tightly correlate with K_0 and could then be used to study cluster cores at high- z . It is also becoming clear that the role of ICM magnetic fields can no longer be ignored. More specifically, how magnetohydrodynamic instabilities, such as MTI (Balbus 2000; Quataert 2008) and HBI (Parrish & Quataert 2008), might impact the entropy structure of the ICM and formation of thermal instabilities needs to be investigated more thoroughly. We hope *ACCEPT* will be a useful resource in studying these questions.

KWC was supported in this work through *Chandra* X-ray Observatory Archive grants AR-6016X and AR-4017A. MD and MS acknowledge support from the NASA LTSA program NNG-05GD82G. The *Chandra* X-ray Observatory Center is operated by the Smithsonian Astrophysical Observatory for and on behalf of NASA under contract NAS8-03060. KWC thanks Chris Waters for supplying and supporting his new KMM code, Jim Linnemann for helpful suggestions regarding the error and statistical analysis presented in this paper, Brian McNamara for useful discussion, and Gabriel Pratt for sharing entropy profiles. We also thank the anonymous referee who's comments greatly improved the content of the paper. This research has made use of software provided by the Chandra X-ray Center in the application packages CIAO, CHIPS, and SHERPA. This research has made use of the NASA/IPAC Extragalactic Database which is operated by the Jet Propulsion Laboratory, California Institute of Technology, under contract with NASA. This research has also made use of NASA's Astrophysics Data System. Some software was obtained from the High Energy Astrophysics Science Archive Research Center, provided by NASA's Goddard Space Flight Center.

Facilities: CXO (ACIS), Du Pont (Modular Spectrograph), Hale (Double Spectrograph)

REFERENCES

Alexander, P. 2002, MNRAS, 335, 610

- Allen, S. W., & Fabian, A. C. 1998, *MNRAS*, 297, L57
- Anders, E., & Grevesse, N. 1989, *Geochim. Cosmochim. Acta*, 53, 197
- Arnaud, K. A. 1996, in *Astronomical Society of the Pacific Conference Series*, Vol. 101, *Astronomical Data Analysis Software and Systems V*, ed. G. H. Jacoby & J. Barnes, 17–+
- Arnaud, M., & Evrard, A. E. 1999, *MNRAS*, 305, 631
- Ashman, K. M., Bird, C. M., & Zepf, S. E. 1994, *AJ*, 108, 2348
- Balbus, S. A. 2000, *ApJ*, 534, 420
- Bauer, F. E., Fabian, A. C., Sanders, J. S., Allen, S. W., & Johnstone, R. M. 2005, *MNRAS*, 359, 1481
- Bîrzan, L., Rafferty, D. A., McNamara, B. R., Wise, M. W., & Nulsen, P. E. J. 2004, *ApJ*, 607, 800
- Böhringer, H., Schuecker, P., Guzzo, L., Collins, C. A., Voges, W., Cruddace, R. G., Ortiz-Gil, A., Chincarini, G., De Grandi, S., Edge, A. C., MacGillivray, H. T., Neumann, D. M., Schindler, S., & Shaver, P. 2004, *A&A*, 425, 367
- Böhringer, H., Schuecker, P., Pratt, G. W., Arnaud, M., Ponman, T. J., Croston, J. H., Borgani, S., Bower, R. G., Briel, U. G., Collins, C. A., Donahue, M., Forman, W. R., Finoguenov, A., Geller, M. J., Guzzo, L., Henry, J. P., Kneissl, R., Mohr, J. J., Matsushita, K., Mullis, C. R., Ohashi, T., Pedersen, K., Pierini, D., Quintana, H., Raychaudhury, S., Reiprich, T. H., Romer, A. K., Rosati, P., Sabirli, K., Temple, R. F., Viana, P. T. P., Vikhlinin, A., Voit, G. M., & Zhang, Y.-Y. 2007, *A&A*, 469, 363
- Borgani, S., Governato, F., Wadsley, J., Menci, N., Tozzi, P., Quinn, T., Stadel, J., & Lake, G. 2002, *MNRAS*, 336, 409
- Bower, R. G. 1997, *MNRAS*, 288, 355
- Bower, R. G., Benson, A. J., Malbon, R., Helly, J. C., Frenk, C. S., Baugh, C. M., Cole, S., & Lacey, C. G. 2006, *MNRAS*, 370, 645
- Bower, R. G., McCarthy, I. G., & Benson, A. J. 2008, *ArXiv e-prints*, 808
- Brighenti, F., & Mathews, W. G. 2006, *ApJ*, 643, 120

- Brüggen, M., & Kaiser, C. R. 2002, *Nature*, 418, 301
- Brüggen, M., Kaiser, C. R., Churazov, E., & Enßlin, T. A. 2002, *MNRAS*, 331, 545
- Bryan, G. L., & Norman, M. L. 1998, *ApJ*, 495, 80
- Buote, D. A., & Tsai, J. C. 1996, *ApJ*, 458, 27
- Burns, J. O., Roettiger, K., Pinkney, J., Perley, R. A., Owen, F. N., & Voges, W. 1995, *ApJ*, 446, 583
- Cavagnolo, K. W., Donahue, M., Voit, G. M., & Sun, M. 2008a, *ApJ*, 683, L107
- . 2008b, *ApJ*, 682, 821
- Cavaliere, A., & Fusco-Femiano, R. 1978, *A&A*, 70, 677
- Chen, Y., Reiprich, T. H., Böhringer, H., Ikebe, Y., & Zhang, Y.-Y. 2007, *A&A*, 466, 805
- Churazov, E., Sunyaev, R., Forman, W., & Böhringer, H. 2002, *MNRAS*, 332, 729
- Croston, J. H., Arnaud, M., Pointecouteau, E., & Pratt, G. W. 2006, *A&A*, 459, 1007
- Croton, D. J., Springel, V., White, S. D. M., De Lucia, G., Frenk, C. S., Gao, L., Jenkins, A., Kauffmann, G., Navarro, J. F., & Yoshida, N. 2006, *MNRAS*, 365, 11
- Dalla Vecchia, C., Bower, R. G., Theuns, T., Balogh, M. L., Mazzotta, P., & Frenk, C. S. 2004, *MNRAS*, 355, 995
- David, L. P., Jones, C., & Forman, W. 1996, *ApJ*, 473, 692
- Dickey, J. M., & Lockman, F. J. 1990, *ARA&A*, 28, 215
- Donahue, M., Gaskin, J. A., Patel, S. K., Joy, M., Clowe, D., & Hughes, J. P. 2003, *ApJ*, 598, 190
- Donahue, M., Horner, D. J., Cavagnolo, K. W., & Voit, G. M. 2006, *ApJ*, 643, 730
- Donahue, M., Voit, G. M., O’Dea, C. P., Baum, S. A., & Sparks, W. B. 2005, *ApJ*, 630, L13
- Donnelly, R. H., Markevitch, M., Forman, W., Jones, C., David, L. P., Churazov, E., & Gilfanov, M. 1998, *ApJ*, 500, 138
- Dunn, R. J. H., & Fabian, A. C. 2008, *MNRAS*, 385, 757

- Edge, A. C., Fabian, A. C., Allen, S. W., Crawford, C. S., White, D. A., Bohringer, H., & Voges, W. 1994, MNRAS, 270, L1+
- Edge, A. C., & Stewart, G. C. 1991, MNRAS, 252, 414
- Edge, A. C., Stewart, G. C., & Fabian, A. C. 1992, MNRAS, 258, 177
- Eke, V. R., Navarro, J. F., & Frenk, C. S. 1998, ApJ, 503, 569
- Ettori, S. 2000, MNRAS, 311, 313
- Evrard, A. E. 1997, MNRAS, 292, 289
- Evrard, A. E., & Henry, J. P. 1991, ApJ, 383, 95
- Evrard, A. E., Metzler, C. A., & Navarro, J. F. 1996, ApJ, 469, 494
- Fabian, A. C. 1994, ARA&A, 32, 277
- Fabian, A. C., Sanders, J. S., Allen, S. W., Crawford, C. S., Iwasawa, K., Johnstone, R. M., Schmidt, R. W., & Taylor, G. B. 2003, MNRAS, 344, L43
- Feretti, L., Boehringer, H., Giovannini, G., & Neumann, D. 1997a, A&A, 317, 432
- Feretti, L., Giovannini, G., & Bohringer, H. 1997b, New Astronomy, 2, 501
- Finoguenov, A., Reiprich, T. H., & Böhringer, H. 2001, A&A, 368, 749
- Forman, W., Nulsen, P., Heinz, S., Owen, F., Eilek, J., Vikhlinin, A., Markevitch, M., Kraft, R., Churazov, E., & Jones, C. 2005, ApJ, 635, 894
- Garmire, G. P., Bautz, M. W., Ford, P. G., Nousek, J. A., & Ricker, Jr., G. R. 2003, in Presented at the Society of Photo-Optical Instrumentation Engineers (SPIE) Conference, Vol. 4851, Society of Photo-Optical Instrumentation Engineers (SPIE) Conference Series, ed. J. E. Truemper & H. D. Tananbaum, 28–44
- Guo, F., Oh, S. P., & Ruszkowski, M. 2008, ArXiv e-prints, arxiv:0804.3823
- Hallman, E. J., Burns, J. O., Motl, P. M., & Norman, M. L. 2007, ApJ, 665, 911
- Heckman, T. M., Baum, S. A., van Breugel, W. J. M., & McCarthy, P. 1989, ApJ, 338, 48
- Hoeft, M., & Brüggen, M. 2004, ApJ, 617, 896
- Hogg, D. W. 2008, ArXiv e-prints, 807

- Horner, D. J., Mushotzky, R. F., & Scharf, C. A. 1999, *ApJ*, 520, 78
- Hu, E. M., Cowie, L. L., & Wang, Z. 1985, *ApJS*, 59, 447
- Hudson, D. S., & Reiprich, T. H. 2007, in *Heating versus Cooling in Galaxies and Clusters of Galaxies*, ed. H. Böhringer, G. W. Pratt, A. Finoguenov, & P. Schuecker, 42–+
- Hudson, D. S., Reiprich, T. H., Clarke, T. E., & Sarazin, C. L. 2006, *A&A*, 453, 433
- Jeltema, T. E., Canizares, C. R., Bautz, M. W., & Buote, D. A. 2005, *ApJ*, 624, 606
- Jones, C., & Forman, W. 1984, *ApJ*, 276, 38
- Kaastra, J. S., Tamura, T., Peterson, J. R., Bleeker, J. A. M., Ferrigno, C., Kahn, S. M., Paerels, F. B. S., Piffaretti, R., Branduardi-Raymont, G., & Böhringer, H. 2004, *A&A*, 413, 415
- Kaiser, C. R., & Binney, J. 2003, *MNRAS*, 338, 837
- Kaiser, N. 1986, *MNRAS*, 222, 323
- . 1991, *ApJ*, 383, 104
- Kalberla, P. M. W., Burton, W. B., Hartmann, D., Arnal, E. M., Bajaja, E., Morras, R., & Pöppel, W. G. L. 2005, *A&A*, 440, 775
- Knuth, K. H. 2006, *ArXiv e-prints*, 605
- Kravtsov, A. V., Vikhlinin, A., & Nagai, D. 2006, *ApJ*, 650, 128
- Kriss, G. A., Cioffi, D. F., & Canizares, C. R. 1983, *ApJ*, 272, 439
- Lloyd-Davies, E. J., Ponman, T. J., & Cannon, D. B. 2000, *MNRAS*, 315, 689
- Loewenstein, M. 2000, *ApJ*, 532, 17
- Loken, C., Norman, M. L., Nelson, E., Burns, J., Bryan, G. L., & Motl, P. 2002, *ApJ*, 579, 571
- Markevitch, M. 1998, *ApJ*, 504, 27
- Mathews, W. G., Faltenbacher, A., & Brighenti, F. 2006, *ApJ*, 638, 659
- Maughan, B. J., Jones, C., Jones, L. R., & Van Speybroeck, L. 2007, *ApJ*, 659, 1125
- McCarthy, I. G., Babul, A., Bower, R. G., & Balogh, M. L. 2008, *MNRAS*, 386, 1309

- McCarthy, I. G., Balogh, M. L., Babul, A., Poole, G. B., & Horner, D. J. 2004, *ApJ*, 613, 811
- McCarthy, I. G., Bower, R. G., Balogh, M. L., Voit, G. M., Pearce, F. R., Theuns, T., Babul, A., Lacey, C. G., & Frenk, C. S. 2007, *MNRAS*, 376, 497
- McNamara, B. R., & Nulsen, P. E. J. 2007, *ARA&A*, 45, 117
- McNamara, B. R., Nulsen, P. E. J., Wise, M. W., Rafferty, D. A., Carilli, C., Sarazin, C. L., & Blanton, E. L. 2005, *Nature*, 433, 45
- McNamara, B. R., O’Connell, R. W., & Bregman, J. N. 1990, *ApJ*, 360, 20
- Mewe, R., Gronenschild, E. H. B. M., & van den Oord, G. H. J. 1985, *A&AS*, 62, 197
- Mewe, R., Lemen, J. R., & van den Oord, G. H. J. 1986, *A&AS*, 65, 511
- Mohr, J. J., Mathiesen, B., & Evrard, A. E. 1999, *ApJ*, 517, 627
- Molendi, S., de Grandi, S., Fusco-Femiano, R., Colafrancesco, S., Fiore, F., Nesci, R., & Tamburelli, F. 1999, *ApJ*, 525, L73
- Morandi, A., & Etti, S. 2007, *MNRAS*, 380, 1521
- Nagai, D., Kravtsov, A. V., & Vikhlinin, A. 2007, *ApJ*, 668, 1
- Nath, B. B., & Roychowdhury, S. 2002, *MNRAS*, 333, 145
- Navarro, J. F., Frenk, C. S., & White, S. D. M. 1995, *MNRAS*, 275, 720
- . 1997, *ApJ*, 490, 493
- Nevalainen, J., Markevitch, M., & Forman, W. 2000, *ApJ*, 536, 73
- Nulsen, P. E. J., McNamara, B. R., Wise, M. W., & David, L. P. 2005, *ApJ*, 628, 629
- O’Dea, C. P., Baum, S. A., Maloney, P. R., Tacconi, L. J., & Sparks, W. B. 1994, *ApJ*, 422, 467
- O’Hara, T. B., Mohr, J. J., Bialek, J. J., & Evrard, A. E. 2006, *ApJ*, 639, 64
- O’Hara, T. B., Mohr, J. J., & Guerrero, M. A. 2004, *ApJ*, 604, 604
- Omma, H., Binney, J., Bryan, G., & Slyz, A. 2004, *MNRAS*, 348, 1105
- Parrish, I. J., & Quataert, E. 2008, *ApJ*, 677, L9

- Peres, C. B., Fabian, A. C., Edge, A. C., Allen, S. W., Johnstone, R. M., & White, D. A. 1998, *MNRAS*, 298, 416
- Peterson, J. R., Kahn, S. M., Paerels, F. B. S., Kaastra, J. S., Tamura, T., Bleeker, J. A. M., Ferrigno, C., & Jernigan, J. G. 2003, *ApJ*, 590, 207
- Peterson, J. R., Paerels, F. B. S., Kaastra, J. S., Arnaud, M., Reiprich, T. H., Fabian, A. C., Mushotzky, R. F., Jernigan, J. G., & Sakelliou, I. 2001, *A&A*, 365, L104
- Piffaretti, R., Jetzer, P., Kaastra, J. S., & Tamura, T. 2005, *A&A*, 433, 101
- Pizzolato, F., & Soker, N. 2005, *ApJ*, 632, 821
- Pointecouteau, E., Arnaud, M., & Pratt, G. W. 2005, *A&A*, 435, 1
- Ponman, T. J., Cannon, D. B., & Navarro, J. F. 1999, *Nature*, 397, 135
- Ponman, T. J., Sanderson, A. J. R., & Finoguenov, A. 2003, *MNRAS*, 343, 331
- Pratt, G. W., Arnaud, M., & Pointecouteau, E. 2006, *A&A*, 446, 429
- Quataert, E. 2008, *ApJ*, 673, 758
- Rafferty, D., McNamara, B., & Nulsen, P. 2008, *ArXiv e-prints*, arxiv:0802.1864
- Reiprich, T. H. 2001, PhD thesis, AA(Max-Planck-Institut für extraterrestrische Physik, P.O. Box 1312, 85741 Garching, Germany)
- Reiprich, T. H., & Böhringer, H. 2002, *ApJ*, 567, 716
- Roychowdhury, S., Ruszkowski, M., Nath, B. B., & Begelman, M. C. 2004, *ApJ*, 615, 681
- Ruszkowski, M., & Begelman, M. C. 2002, *ApJ*, 581, 223
- Sanders, J. S., & Fabian, A. C. 2008, *ArXiv e-prints*, 808
- Saro, A., Borgani, S., Tornatore, L., Dolag, K., Murante, G., Biviano, A., Calura, F., & Charlot, S. 2006, *MNRAS*, 373, 397
- Sharma, M., McNamara, B. R., Nulsen, P. E. J., Owers, M., Wise, M. W., Blanton, E. L., Sarazin, C. L., Owen, F. N., & David, L. P. 2004, *ApJ*, 613, 180
- Soker, N., & Pizzolato, F. 2005, *ApJ*, 622, 847
- Soker, N., White, III, R. E., David, L. P., & McNamara, B. R. 2001, *ApJ*, 549, 832

- Stewart, G. C., Fabian, A. C., Jones, C., & Forman, W. 1984, *ApJ*, 285, 1
- Sun, M., Jones, C., Forman, W., Vikhlinin, A., Donahue, M., & Voit, M. 2007, *ApJ*, 657, 197
- Sun, M., & Murray, S. S. 2002, *ApJ*, 576, 708
- Sun, M., Voit, G. M., Donahue, M., Jones, C., & Forman, W. 2008, ArXiv e-prints, arxiv:0805.2320
- Tamura, T., Kaastra, J. S., Peterson, J. R., Paerels, F. B. S., Mittaz, J. P. D., Trudolyubov, S. P., Stewart, G., Fabian, A. C., Mushotzky, R. F., Lumb, D. H., & Ikebe, Y. 2001, *A&A*, 365, L87
- Teyssier, R., Chieze, J.-P., & Alimi, J.-M. 1997, *ApJ*, 480, 36
- Tozzi, P., & Norman, C. 2001, *ApJ*, 546, 63
- Ventimiglia, D. A., Voit, G. M., Donahue, M., & Ameglio, S. 2008, ArXiv e-prints, arxiv:0806.0850
- Vikhlinin, A., Markevitch, M., Murray, S. S., Jones, C., Forman, W., & Van Speybroeck, L. 2005, *ApJ*, 628, 655
- Voit, G. M., & Bryan, G. L. 2001, *Nature*, 414, 425
- Voit, G. M., Bryan, G. L., Balogh, M. L., & Bower, R. G. 2002, *ApJ*, 576, 601
- Voit, G. M., Cavagnolo, K. W., Donahue, M., Rafferty, D. A., McNamara, B. R., & Nulsen, P. E. J. 2008, *ApJ*, 681, L5
- Voit, G. M., & Donahue, M. 1995, *ApJ*, 452, 164
- . 2005, *ApJ*, 634, 955
- Voit, G. M., Kay, S. T., & Bryan, G. L. 2005, *MNRAS*, 364, 909
- Wang, Q. D., Connolly, A., & Brunner, R. 1997, *ApJ*, 487, L13+
- Wang, Q. D., Owen, F., & Ledlow, M. 2004, *ApJ*, 611, 821
- Waters, C. Z., Zepf, S. E., Lauer, T. R., & Baltz, E. A. 2008, Submitted to *ApJ*

- Weisskopf, M. C., Tananbaum, H. D., Van Speybroeck, L. P., & O'Dell, S. L. 2000, in Presented at the Society of Photo-Optical Instrumentation Engineers (SPIE) Conference, Vol. 4012, Proc. SPIE Vol. 4012, p. 2-16, X-Ray Optics, Instruments, and Missions III, Joachim E. Truemper; Bernd Aschenbach; Eds., ed. J. E. Truemper & B. Aschenbach, 2–16
- White, D. A., Jones, C., & Forman, W. 1997, MNRAS, 292, 419
- Xue, Y.-J., & Wu, X.-P. 2000, MNRAS, 318, 715

A. Notes on clusters requiring β -model fit

- Abell 119** ($z = 0.0442$): This is a highly diffuse cluster without a prominent cool core. The large core region and slowly varying surface brightness made deprojection highly unstable. We have excluded a small source at the very center of the BCG. The exclusion region for the source is $\approx 2.2''$ in radius which at the redshift of the cluster is ~ 2 kpc. This cluster required a double β -model.
- Abell 160** ($z = 0.0447$): The highly asymmetric, low surface brightness of this cluster resulted in a noisy surface brightness profile that could not be deprojected. This cluster required a double β -model. The BCG hosts a compact X-ray source. The exclusion region for the compact source has a radius of $\sim 5''$ or ~ 4.3 kpc. The BCG for this cluster is not coincident with the X-ray centroid and hence is not at the zero-point of our radial analysis.
- Abell 193** ($z = 0.0485$): This cluster has an azimuthally symmetric and a very diffuse ICM centered on a BCG which is interacting with a companion galaxy. In Fig. 1 one can see that the central three bins of this cluster's surface brightness profile are highly discrepant from the best-fit β -model. This is a result of the BCG being coincident with a bright, compact X-ray source. As we have concluded in 3.5, compact X-ray sources are excluded from our analysis as they are not the focus of our study here. Hence we have used the best-fit β -model in deriving $K(r)$ instead of the raw surface brightness.
- Abell 400** ($z = 0.0240$): The two ellipticals at the center of this cluster have compact X-ray sources which are excluded during analysis. The core entropy we derive for this

cluster is in agreement with that found by Hudson et al. (2006) which supports the accuracy of the β -model we have used.

Abell 1060 ($z = 0.0125$): There is a distinct compact source associated with the BCG in this cluster. The ICM is also very faint and uniform in surface brightness making the compact source that much more obvious. Deprojection was unstable because of imperfect exclusion of the source.

Abell 1240 ($z = 0.1590$): The surface brightness of this cluster is well-modeled by a β -model. There is nothing peculiar worth noting about the BCG or the core of this cluster.

Abell 1736 ($z = 0.0338$): Another “boring” cluster with a very diffuse low surface brightness ICM, no peaky core, and no signs of merger activity in the X-ray. The noisy surface brightness profile necessitated the use of a double β -model. The BCG is coincident with a very compact X-ray source, but the BCG is offset from the X-ray centroid and thus the central bins are not adversely affected. The radius of the exclusion region for the compact source is $\approx 2.3''$ or 1.5 kpc.

Abell 2125 ($z = 0.2465$): Although the ICM of this cluster is very similar to the other clusters listed here (*i.e.* diffuse, large cores), A2125 is one of the more compact clusters. The presence of several merging sub-clusters (Wang et al. 1997, 2004) to the NW of the main cluster form a diffuse mass which cannot rightly be excluded. This complication yields inversions of the deprojected surface brightness profile if a double β -model is not used.

Abell 2255 ($z = 0.0805$): This is a very well studied merger cluster (Burns et al. 1995; Feretti et al. 1997a). The core of this cluster is very large ($r > 200$ kpc). Such large extended cores cannot be deprojected using our methods because if too many neighboring bins have approximately the same surface brightness, deprojection results in bins with negative or zero value. The surface brightness for this cluster is well modeled as a β function.

Abell 2319 ($z = 0.0562$): A2319 is another well studied merger cluster (Feretti et al. 1997b; Molendi et al. 1999) with a very large core region ($r > 100$ kpc) and a prominent cold front (O’Hara et al. 2004). Once again, the surface brightness profile is well-fit by a β -model.

Abell 2462 ($z = 0.0737$): This cluster is very similar in appearance to A193: highly symmetric ICM with a bright, compact X-ray source embedded at the center of an extended diffuse ICM. The central compact source has been excluded from our analysis with a

region of radius $\approx 1.5''$ or ~ 3 kpc. The central bin of the surface brightness profile is most likely boosted above the best-fit double β -model because of faint extended emission from the compact source which cannot be discerned from the ambient ICM.

Abell 2631 ($z = 0.2779$): The surface brightness profile for this cluster is rather regular, but because the cluster has a large core it suffers from the same unstable deprojection as A2255 and A2319. The ICM is symmetric about the BCG and is incredibly uniform in the core region. We did not detect or exclude a source at the center of this cluster, but under heavy binning the cluster image appears to have a source coincident with the BCG, and the slightly higher flux in central bin of the surface brightness profile may be a result of an unresolved source.

Abell 3376 ($z = 0.0456$): The large core of this cluster ($r > 120$ kpc) makes deprojection unstable and a β -model must be used.

Abell 3391 ($z = 0.0560$): The BCG is coincident with a compact X-ray source. The source is excluded using a region with radius $\approx 2''$ or ~ 2 kpc. The large uniform core region made deprojection unstable and thus required a β -model fit.

Abell 3395 ($z = 0.0510$): The surface brightness profile for this cluster is noisy resulting in deprojection inversions and requiring a β -model fit. The BCG of this cluster has a compact X-ray source and this source was excluded using a region with radius $\approx 1.9''$ or ~ 2 kpc.

MKW 08 ($z = 0.0270$): MKW 08 is a nearby large group/poor cluster with a pair of interacting elliptical galaxies in the core. The BCG falls directly in the middle of the ACIS-I detector gap. However, despite the lack of proper exposure, CCD dithering reveals that a very bright X-ray source is associated with the BCG. A double β -model was necessary for this cluster because the low surface brightness of the ICM is noisy and deprojection is unstable.

RBS 461 ($z = 0.0290$): This is another nearby large group/poor cluster with an extended, diffuse, axisymmetric, featureless ICM centered on the BCG. The BCG is coincident with a compact source with size $r \approx 1.7$ kpc. This source was excluded during reduction. The β -model is a good fit to the surface brightness profile.

Table 1. Summary of Sample

Cluster	Obs. ID	R.A. hr:min:sec	Decl. ° : ' : "	Exposure Time ksec	ACIS	z	kT_X keV	Notes
(1)	(2)	(3)	(4)	(5)	(6)	(7)	(8)	(9)
1E0657 56	3184	06:58:29.627	-55:56:39.79	87.5	I3	0.2960	11.64	...
	5356	97.2	I2
	5361	82.6	I3
2A 335+096	919	03:38:41.105	+09:58:00.66	19.7	S3	0.0347	2.88	...
2PIGG J0011.5-2850	5797	00:11:21.623	-28:51:14.44	19.9	I3	0.0753	5.15	f
2PIGG J2227.0-3041	5798	22:27:54.560	-30:34:34.84	22.3	I2	0.0729	2.79	...
3C 28.0	3233	00:55:50.401	+26:24:36.47	49.7	I3	0.1952	5.53	...
3C 295	2254	14:11:20.280	+52:12:10.55	90.9	I3	0.4641	5.16	d
3C 388	5295	18:44:02.365	+45:33:29.31	30.7	I3	0.0917	3.23	d
4C 55.16	4940	08:34:54.923	+55:34:21.15	96.0	S3	0.2420	4.98	d
Abell 13	4945	00:13:37.883	-19:30:09.10	55.3	S3	0.0940	6.84	...
Abell 68	3250	00:37:06.475	+09:09:32.28	10.0	I3	0.2546	9.01	...
Abell 85	904	00:41:50.406	-09:18:10.79	38.4	I0	0.0558	6.40	...
Abell 119	4180	00:56:15.150	-01:14:59.70	11.9	I3	0.0442	5.86	a,e
Abell 133	2203	01:02:41.756	-21:52:49.79	35.5	S3	0.0558	4.31	...
Abell 141	9410	01:05:34.385	-24:37:58.78	19.9	I3	0.2300	5.31	...
Abell 160	3219	01:13:00.692	+15:29:15.08	58.5	I3	0.0447	1.88	a,e
Abell 193	6931	01:25:07.660	+08:41:57.08	17.9	S3	0.0485	2.50	a,e
Abell 209	3579	01:31:52.565	-13:36:38.79	10.0	I3	0.2060	8.28	...
	522	10.0	I3
Abell 222	4967	01:37:34.562	-12:59:34.88	45.1	I3	0.2130	4.60	...
Abell 223	49671	01:37:55.963	-12:49:10.53	45.1	I0	0.2070	5.28	e
Abell 262	2215	01:52:46.299	+36:09:11.80	28.7	S3	0.0164	2.18	...
	7921	110.7	S3
Abell 267	1448	01:52:42.269	+01:00:45.33	7.9	I3	0.2300	6.79	...
	3580	19.9	I3
Abell 368	9412	02:37:27.640	-26:30:28.99	18.4	I3	0.2200	6.23	...
Abell 370	515	02:39:53.169	-01:34:36.96	88.0	S3	0.3747	7.35	...
Abell 383	2321	02:48:03.364	-03:31:44.69	19.5	S3	0.1871	4.91	...
Abell 399	3230	02:57:53.382	+13:01:30.86	48.6	I0	0.0716	7.95	...
Abell 400	4181	02:57:41.603	+06:01:27.61	21.5	I3	0.0240	2.31	a,e
Abell 401	2309	02:58:56.920	+13:34:14.51	11.6	I2	0.0745	8.07	...
	518	18.0	I3
Abell 426	3209	03:19:48.194	+41:30:40.73	95.8	S3	0.0179	3.55	d
	4289	95.4	S3
Abell 478	1669	04:13:25.345	+10:27:55.15	42.4	S3	0.0883	7.07	...
	6102	10.0	I3
Abell 496	3361	04:33:38.038	-13:15:39.65	10.0	S3	0.0328	5.03	...
Abell 520	4215	04:54:10.303	+02:55:36.48	66.3	I3	0.2020	9.29	...
Abell 521	430	04:54:06.337	-10:13:16.88	39.1	S3	0.2533	7.03	...
Abell 539	5808	05:16:37.335	+06:26:25.18	24.3	I3	0.0288	3.24	b,e
	7209	18.6	I3
Abell 562	6936	06:53:21.524	+69:19:51.19	51.5	S3	0.1100	3.04	e
Abell 576	3289	07:21:30.394	+55:45:41.95	38.6	S3	0.0385	4.43	e

Table 1—Continued

Cluster	Obs. ID	R.A. hr:min:sec	Decl. ° : ' : "	Exposure Time ksec	ACIS	z	kT_X keV	Notes
(1)	(2)	(3)	(4)	(5)	(6)	(7)	(8)	(9)
Abell 586	530	07:32:20.339	+31:37:58.59	10.0	I3	0.1710	6.47	...
Abell 611	3194	08:00:56.832	+36:03:24.09	36.1	S3	0.2880	7.06	e
Abell 644	2211	08:17:25.225	-07:30:40.03	29.7	I3	0.0698	7.73	...
Abell 665	3586	08:30:59.226	+65:50:20.06	29.7	I3	0.1810	7.45	...
Abell 697	4217	08:42:57.549	+36:21:57.65	19.5	I3	0.2820	9.52	...
Abell 744	6947	09:07:20.455	+16:39:06.18	39.5	I3	0.0729	2.50	e
Abell 754	577	09:09:18.188	-09:41:09.56	44.2	I3	0.0543	9.94	...
Abell 773	5006	09:17:52.566	+51:43:38.18	19.8	I3	0.2170	7.83	...
Abell 907	3185	09:58:21.946	-11:03:50.73	48.0	I3	0.1527	5.59	...
	3205	47.1	I3
	535	11.0	I3
Abell 963	903	10:17:03.744	+39:02:49.17	36.3	S3	0.2056	6.73	...
Abell 1060	2220	10:36:42.828	-27:31:42.06	31.9	I3	0.0125	3.29	a,e,f
Abell 1063S	4966	22:48:44.294	-44:31:48.37	26.7	I3	0.3540	11.96	...
Abell 1068	1652	10:40:44.520	+39:57:10.28	26.8	S3	0.1375	4.62	...
Abell 1201	4216	11:12:54.489	+13:26:08.76	39.7	S3	0.1688	5.61	...
Abell 1204	2205	11:13:20.419	+17:35:38.45	23.6	I3	0.1706	3.63	...
Abell 1240	4961	11:23:38.357	+43:05:48.33	51.3	I3	0.1590	4.77	a
Abell 1361	2200	11:43:39.637	+46:21:20.41	16.7	S3	0.1171	5.32	...
Abell 1413	5003	11:55:17.893	+23:24:21.84	75.1	I2	0.1426	7.41	...
Abell 1423	538	11:57:17.263	+33:36:37.44	9.8	I3	0.2130	6.01	...
Abell 1446	4975	12:02:03.744	+58:02:17.93	58.4	S3	0.1035	3.96	...
Abell 1569	6100	12:36:26.015	+16:32:17.81	41.2	I3	0.0735	2.51	...
Abell 1576	7938	12:36:58.274	+63:11:13.88	15.0	I3	0.2790	10.10	...
Abell 1644	2206	12:57:11.665	-17:24:32.86	18.7	I3	0.0471	4.60	b
	7922	51.5	I3
Abell 1650	4178	12:58:41.499	-01:45:44.32	27.3	S3	0.0843	6.17	...
Abell 1651	4185	12:59:22.830	-04:11:45.86	9.6	I3	0.0840	6.26	...
Abell 1664	1648	13:03:42.622	-24:14:41.59	9.8	S3	0.1276	4.39	...
	7901	36.6	S3
Abell 1689	1663	13:11:29.612	-01:20:28.69	10.7	I3	0.1843	10.10	...
	5004	19.9	I3
	540	10.3	I3
Abell 1736	4186	13:26:49.453	-27:09:48.13	14.9	I1	0.0338	3.45	a,e
Abell 1758	2213	13:32:48.398	+50:32:32.53	58.3	S3	0.2792	12.14	...
Abell 1763	3591	13:35:17.957	+40:59:55.80	19.6	I3	0.1866	7.78	...
Abell 1795	493	13:48:52.802	+26:35:23.55	19.6	S3	0.0625	7.80	...
	5289	15.0	I3
Abell 1835	495	14:01:01.951	+02:52:43.18	19.5	S3	0.2532	9.77	...
Abell 1914	3593	14:26:03.060	+37:49:27.84	18.9	I3	0.1712	9.62	...
Abell 1942	3290	14:38:21.878	+03:40:12.97	57.6	I2	0.2240	4.77	...
Abell 1991	3193	14:54:31.620	+18:38:41.48	38.3	S3	0.0587	2.67	...
Abell 1995	7021	14:52:57.410	+58:02:56.84	48.5	I3	0.3186	3.40	...
Abell 2029	4977	15:10:56.139	+05:44:40.47	77.9	S3	0.0765	7.38	...

Table 1—Continued

Cluster	Obs. ID	R.A. hr:min:sec	Decl. ° : ' : "	Exposure Time ksec	ACIS	z	kT_X keV	Notes
(1)	(2)	(3)	(4)	(5)	(6)	(7)	(8)	(9)
	6101	9.9	I3
	891	19.8	S3
Abell 2034	2204	15:10:12.498	+33:30:39.57	53.9	I3	0.1130	7.15	f
Abell 2052	5807	15:16:44.514	+07:01:17.02	127.0	S3	0.0353	2.98	d
	890	36.8	S3
Abell 2063	4187	15:23:04.851	+08:36:20.16	8.8	I3	0.0351	3.61	...
	6263	16.8	S3
Abell 2065	31821	15:22:29.517	+27:42:22.93	27.7	I3	0.0730	5.75	...
Abell 2069	4965	15:24:11.376	+29:52:19.02	55.4	I2	0.1160	6.50	...
Abell 2104	895	15:40:08.131	-03:18:15.02	49.2	S3	0.1554	8.53	...
Abell 2107	4960	15:39:39.113	+21:46:57.66	35.6	I3	0.0411	3.82	b
Abell 2111	544	15:39:40.637	+34:25:28.01	10.3	I3	0.2300	7.13	...
Abell 2124	3238	15:44:59.131	+36:06:34.11	19.4	S3	0.0658	4.73	...
Abell 2125	2207	15:41:14.154	+66:15:57.20	81.5	I3	0.2465	2.88	a
Abell 2142	1196	15:58:20.880	+27:13:44.21	11.4	S3	0.0898	8.24	...
	1228	12.1	S3
	5005	44.6	I3
Abell 2147	3211	16:02:17.025	+15:58:28.32	17.9	I3	0.0356	4.09	...
Abell 2151	4996	16:04:35.887	+17:43:17.36	21.8	I3	0.0366	2.90	e
Abell 2163	1653	16:15:45.705	-06:09:00.62	71.1	I1	0.1695	19.20	...
Abell 2199	497	16:28:38.249	+39:33:04.28	19.5	S3	0.0300	4.55	b
Abell 2204	499	16:32:46.920	+05:34:32.86	10.1	S3	0.1524	6.97	...
	6104	9.6	I3
	7940	77.1	I3
Abell 2218	1666	16:35:50.831	+66:12:42.31	48.6	I0	0.1713	7.35	...
Abell 2219	896	16:40:20.112	+46:42:42.84	42.3	S3	0.2256	12.75	...
Abell 2244	4179	17:02:42.579	+34:03:37.34	57.0	S3	0.0967	5.68	...
Abell 2255	894	17:12:42.935	+64:04:10.81	39.4	I3	0.0805	6.12	a
Abell 2256	1386	17:03:44.567	+78:38:11.51	12.4	I3	0.0579	6.90	a
Abell 2259	3245	17:20:08.299	+27:40:11.53	10.0	I3	0.1640	5.18	...
Abell 2261	5007	17:22:27.254	+32:07:58.60	24.3	I3	0.2240	7.63	...
Abell 2294	3246	17:24:10.149	+85:53:09.77	10.0	I3	0.1780	9.98	...
Abell 2319	3231	19:21:09.638	+43:57:21.53	14.4	I1	0.0562	10.87	a
Abell 2384	4202	21:52:21.178	-19:32:51.90	31.5	I3	0.0945	4.75	...
Abell 2390	4193	21:53:36.825	+17:41:44.38	95.1	S3	0.2301	11.15	...
Abell 2409	3247	22:00:52.567	+20:58:06.55	10.2	I3	0.1479	5.94	...
Abell 2420	8271	22:10:18.792	-12:10:13.35	8.1	I3	0.0846	6.47	...
Abell 2462	4159	22:39:11.367	-17:20:28.33	39.2	S3	0.0737	2.42	a,e
Abell 2537	4962	23:08:22.313	-02:11:29.88	36.2	S3	0.2950	8.40	...
Abell 2554	1696	23:12:19.622	-21:30:11.32	19.9	S3	0.1103	5.29	...
Abell 2556	2226	23:13:01.413	-21:38:04.47	19.9	S3	0.0862	3.50	...
Abell 2589	3210	23:23:57.315	+16:46:38.43	13.7	S3	0.0415	3.65	...
Abell 2597	922	23:25:19.779	-12:07:27.63	39.4	S3	0.0854	4.02	...
Abell 2626	3192	23:36:30.452	+21:08:47.36	24.8	S3	0.0573	3.29	...

Table 1—Continued

Cluster	Obs. ID	R.A. hr:min:sec	Decl. ° : ' : "	Exposure Time ksec	ACIS	z	kT_X keV	Notes
(1)	(2)	(3)	(4)	(5)	(6)	(7)	(8)	(9)
Abell 2631	3248	23:37:38.560	+00:16:05.02	9.2	I3	0.2779	7.06	a
Abell 2657	4941	23:44:57.253	+09:11:30.74	16.1	I3	0.0402	3.77	...
Abell 2667	2214	23:51:39.395	-26:05:02.75	9.6	S3	0.2300	6.75	...
Abell 2717	6974	00:03:12.968	-35:56:00.13	19.8	I3	0.0475	1.69	e
Abell 2744	2212	00:14:19.529	-30:23:30.24	24.8	S3	0.3080	9.18	...
	7915	18.6	I3
	8477	45.9	I3
	8557	27.8	I3
Abell 2813	9409	00:43:24.881	-20:37:25.08	19.9	I3	0.2924	8.96	...
Abell 3084	9413	03:04:03.920	-36:56:27.17	19.9	I3	0.0977	5.30	...
Abell 3088	9414	03:07:01.734	-28:39:55.47	18.9	I3	0.2534	6.71	...
Abell 3112	2516	03:17:57.681	-44:14:17.16	16.9	S3	0.0720	5.17	d
Abell 3120	6951	03:21:56.464	-51:19:35.40	26.8	I3	0.0690	4.40	...
Abell 3158	3201	03:42:54.675	-53:37:24.36	24.8	I3	0.0580	4.94	...
	3712	30.9	I3
Abell 3266	899	04:31:13.304	-61:27:12.59	29.8	I1	0.0590	9.07	...
Abell 3364	9419	05:47:37.698	-31:52:23.61	19.8	I3	0.1483	7.88	...
Abell 3376	3202	06:02:11.756	-39:56:59.07	44.3	I3	0.0456	4.08	a
	3450	19.8	I3
Abell 3391	4943	06:26:21.511	-53:41:44.81	18.4	I3	0.0560	6.07	a,e
Abell 3395	4944	06:26:48.463	-54:32:59.21	21.9	I3	0.0510	5.13	a,e
Abell 3528S	8268	12:54:40.897	-29:13:38.10	8.1	I3	0.0530	5.44	...
Abell 3558	1646	13:27:56.854	-31:29:43.78	14.4	S3	0.0480	6.60	e,f
Abell 3562	4167	13:33:37.800	-31:40:12.04	19.3	I2	0.0490	4.59	...
Abell 3571	4203	13:47:28.434	-32:51:52.45	34.0	S3	0.0391	7.77	...
Abell 3581	1650	14:07:29.777	-27:01:05.88	7.2	S3	0.0218	2.10	d
Abell 3667	5751	20:12:41.231	-56:50:35.70	128.9	I3	0.0556	6.51	...
	5752	60.4	I3
	5753	103.6	I3
	889	50.3	I2
Abell 3822	8269	21:54:04.203	-57:52:02.71	8.1	I3	0.0759	4.89	e
Abell 3827	7920	22:01:53.200	-59:56:43.04	45.6	S3	0.0984	8.05	...
Abell 3921	4973	22:49:57.829	-64:25:42.17	29.4	I3	0.0927	5.69	...
Abell 4038	4992	23:47:43.180	-28:08:34.81	33.5	I2	0.0300	3.11	...
Abell 4059	5785	23:57:01.065	-34:45:33.28	92.1	S3	0.0475	4.69	...
Abell S0405	8272	03:51:32.815	-82:13:10.19	7.9	I3	0.0613	4.11	...
Abell S0592	9420	06:38:48.610	-53:58:26.32	19.9	I3	0.2216	9.08	...
AC 114	1562	22:58:48.316	-34:48:08.20	72.5	S3	0.3120	7.53	...
AWM7	908	02:54:27.631	+41:34:47.07	47.9	I3	0.0172	3.71	b
Centaurus	4190	12:48:49.267	-41:18:39.54	34.3	S3	0.0109	3.96	b
	4191	34.0	S3
	4954	89.1	S3
	4955	44.7	S3
	504	31.8	S3

Table 1—Continued

Cluster	Obs. ID	R.A. hr:min:sec	Decl. ° : ' : "	Exposure Time ksec	ACIS	z	kT_X keV	Notes
(1)	(2)	(3)	(4)	(5)	(6)	(7)	(8)	(9)
CID 72	505	10.0	S3
	5310	49.3	S3
	2018	17:33:03.247	+43:45:37.28	30.7	S3	0.0344	1.91	...
	6949	38.6	I3
	7321	37.5	I3
CL J1226.9+3332	7322	37.5	I3
	3180	12:26:58.373	+33:32:47.36	31.7	I3	0.8900	10.00	...
	5014	32.7	I3
	932	9.8	S3
Cygnus A	360	19:59:28.381	+40:44:01.98	34.7	S3	0.0561	7.68	d
ESO 3060170	3188	05:40:06.687	-40:50:12.82	14.0	I3	0.0358	2.79	b
	3189	14.1	I0
ESO 5520200	3206	04:54:52.318	-18:06:56.52	23.9	I3	0.0314	2.37	...
EXO 422-086	4183	04:25:51.271	-08:33:36.42	10.0	I3	0.0397	3.40	...
HCG 62	921	12:53:05.741	-09:12:15.64	48.5	S3	0.0146	1.10	...
HCG 42	3215	10:00:14.234	-19:38:10.77	31.7	S3	0.0133	0.70	...
Hercules A	1625	16:51:08.161	+04:59:32.44	14.8	S3	0.1541	5.21	...
	5796	47.5	S3
	6257	49.5	S3
Hydra A	4970	09:18:05.985	-12:05:43.94	98.8	S3	0.0549	4.00	d
	576	19.5	S3
M49	321	12:29:46.841	+08:00:01.98	39.6	S3	0.0033	1.33	c
M87	5826	12:30:49.383	+12:23:28.67	126.8	I3	0.0044	2.50	d
	5827	156.2	I3
MACS J0011.7-1523	3261	00:11:42.965	-15:23:20.79	21.6	I3	0.3600	5.42	...
	6105	37.3	I3
MACS J0035.4-2015	3262	00:35:26.573	-20:15:46.06	21.4	I3	0.3644	7.39	...
MACS J0159.8-0849	3265	01:59:49.453	-08:50:00.90	17.9	I3	0.4050	9.59	...
	6106	35.3	I3
MACS J0242.5-2132	3266	02:42:35.906	-21:32:26.30	11.9	I3	0.3140	5.58	...
MACS J0257.1-2325	1654	02:57:09.130	-23:26:05.85	19.8	I3	0.5053	10.50	...
	3581	18.5	I3
MACS J0257.6-2209	3267	02:57:41.024	-22:09:11.12	20.5	I3	0.3224	8.02	...
MACS J0308.9+2645	3268	03:08:55.927	+26:45:38.34	24.4	I3	0.3240	10.54	...
MACS J0329.6-0211	3257	03:29:41.681	-02:11:47.67	9.9	I3	0.4500	5.20	...
	3582	19.9	I3
	6108	39.6	I3
MACS J0417.5-1154	3270	04:17:34.686	-11:54:32.71	12.0	I3	0.4400	11.07	...
MACS J0429.6-0253	3271	04:29:36.088	-02:53:09.02	23.2	I3	0.3990	5.66	...
MACS J0520.7-1328	3272	05:20:42.052	-13:28:49.38	19.2	I3	0.3398	6.27	...
MACS J0547.0-3904	3273	05:47:01.582	-39:04:28.24	21.7	I3	0.2100	3.58	e
MACS J0717.5+3745	1655	07:17:31.654	+37:45:18.52	19.9	I3	0.5480	10.50	...
	4200	59.2	I3
MACS J0744.8+3927	3197	07:44:52.802	+39:27:24.41	20.2	I3	0.6860	11.29	...

Table 1—Continued

Cluster	Obs. ID	R.A. hr:min:sec	Decl. ° : ' : "	Exposure Time ksec	ACIS	z	kT_X keV	Notes
(1)	(2)	(3)	(4)	(5)	(6)	(7)	(8)	(9)
MACS J1115.2+5320	3585	19.9	I3
	6111	49.5	I3
	3253	11:15:15.632	+53:20:03.31	8.8	I3	0.4390	8.03	...
	5008	18.0	I3
	5350	6.9	I3
MACS J1115.8+0129	3275	11:15:52.048	+01:29:56.56	15.9	I3	0.1200	6.78	...
MACS J1131.8-1955	3276	11:31:54.580	-19:55:44.54	13.9	I3	0.3070	8.64	...
MACS J1149.5+2223	1656	11:49:35.856	+22:23:55.02	18.5	I3	0.5440	8.40	...
	3589	20.0	I3
MACS J1206.2-0847	3277	12:06:12.276	-08:48:02.40	23.5	I3	0.4400	10.21	...
MACS J1311.0-0310	3258	13:11:01.665	-03:10:39.50	14.9	I3	0.4940	5.60	...
	6110	63.2	I3
MACS J1621.3+3810	3254	16:21:24.801	+38:10:08.65	9.8	I3	0.4610	7.53	...
	3594	19.7	I3
	6109	37.5	I3
	6172	29.8	I3
MACS J1931.8-2634	3282	19:31:49.656	-26:34:33.99	13.6	I3	0.3520	6.97	e
MACS J2049.9-3217	3283	20:49:56.245	-32:16:52.30	23.8	I3	0.3254	6.98	...
MACS J2211.7-0349	3284	22:11:45.856	-03:49:37.24	17.7	I3	0.2700	11.30	...
MACS J2214.9-1359	3259	22:14:57.467	-14:00:09.35	19.5	I3	0.5026	8.80	...
	5011	18.5	I3
MACS J2228+2036	3285	22:28:33.872	+20:37:18.31	19.9	I3	0.4120	7.86	...
MACS J2229.7-2755	3286	22:29:45.358	-27:55:38.41	16.4	I3	0.3240	5.01	...
MACS J2245.0+2637	3287	22:45:04.657	+26:38:03.46	16.9	I3	0.3040	6.06	...
MKW3S	900	15:21:51.930	+07:42:31.97	57.3	I3	0.0450	2.18	...
MKW 4	3234	12:04:27.218	+01:53:42.79	30.0	S3	0.0198	2.06	...
MKW 8	4942	14:40:39.633	+03:28:13.61	23.1	I3	0.0270	3.29	a,b
MS J0016.9+1609	520	00:18:33.503	+16:26:12.99	67.4	I3	0.5410	8.94	...
MS J0116.3-0115	4963	01:18:53.944	-01:00:07.54	39.3	S3	0.0452	1.84	...
MS J0440.5+0204	4196	04:43:09.952	+02:10:18.70	59.4	S3	0.1900	5.46	...
MS J0451.6-0305	902	04:54:11.004	-03:00:52.19	44.2	S3	0.5386	8.90	...
MS J0735.6+7421	4197	07:41:44.245	+74:14:38.23	45.5	S3	0.2160	5.55	...
MS J0839.8+2938	2224	08:42:55.969	+29:27:26.97	29.8	S3	0.1940	4.68	...
MS J0906.5+1110	924	09:09:12.753	+10:58:32.00	29.7	I3	0.1630	5.38	...
MS J1006.0+1202	925	10:08:47.462	+11:47:36.31	29.4	I3	0.2210	5.61	...
MS J1008.1-1224	926	10:10:32.312	-12:39:56.80	44.2	I3	0.3010	7.45	...
MS J1455.0+2232	4192	14:57:15.088	+22:20:32.49	91.9	I3	0.2590	4.77	...
MS J2137.3-2353	4974	21:40:15.178	-23:39:40.71	57.4	S3	0.3130	6.01	...
MS J1157.3+5531	4964	11:59:52.295	+55:32:05.61	75.1	S3	0.0810	3.28	b
NGC 507	2882	01:23:39.905	+33:15:21.73	43.6	I3	0.0164	1.40	c
NGC 4636	3926	12:42:49.856	+02:41:15.86	74.7	I3	0.0031	0.66	c
	4415	74.4	I3
NGC 5044	3225	13:15:23.947	-16:23:07.62	83.1	S3	0.0090	1.22	c
	3664	61.3	S3

Table 1—Continued

Cluster	Obs. ID	R.A. hr:min:sec	Decl. ° : ' : "	Exposure Time ksec	ACIS	z	kT_X keV	Notes
(1)	(2)	(3)	(4)	(5)	(6)	(7)	(8)	(9)
NGC 5813	5907	15:01:11.260	+01:42:07.23	48.4	S3	0.0066	0.76	c
NGC 5846	788	15:06:29.289	+01:36:20.13	29.9	S3	0.0057	0.64	c
Ophiuchus	3200	17:12:27.731	-23:22:06.74	50.5	S3	0.0280	11.12	...
PKS 0745-191	2427	07:47:31.436	-19:17:39.78	17.9	S3	0.1028	8.50	...
	508	28.0	S3
	6103	10.3	I3
RBS 461	4182	03:41:17.490	+15:23:54.66	23.4	I3	0.0290	2.60	a,e
RBS 533	3186	04:19:38.105	+02:24:35.54	10.0	I3	0.0123	1.29	...
	3187	9.6	I3
	5800	44.5	S3
	5801	44.4	S3
RBS 797	2202	09:47:12.693	+76:23:13.40	11.7	I3	0.3540	7.68	d
	7902	38.3	S3
RCS J2327-0204	7355	23:27:27.524	-02:04:39.01	24.7	S3	0.2000	7.06	...
RX J0220.9-3829	9411	02:20:56.582	-38:28:51.21	19.9	I3	0.2287	5.02	...
RX J0232.2-4420	4993	02:32:18.771	-44:20:46.68	23.4	I3	0.2836	7.83	...
RX J0439+0520	527	04:39:02.218	+05:20:43.11	9.6	I3	0.2080	4.60	...
RX J0439.0+0715	1449	04:39:00.710	+07:16:07.65	6.3	I3	0.2300	6.50	...
	3583	19.2	I3
RX J0528.9-3927	4994	05:28:53.039	-39:28:15.53	22.5	I3	0.2632	7.89	...
RX J0647.7+7015	3196	06:47:50.029	+70:14:49.66	19.3	I3	0.5840	9.07	...
	3584	20.0	I3
RX J0819.6+6336	2199	08:19:26.007	+63:37:26.53	14.9	S3	0.1190	3.87	...
RX J1000.4+4409	9421	10:00:32.024	+44:08:39.69	18.5	I3	0.1540	3.42	...
RX J1022.1+3830	6942	10:22:10.034	+38:31:23.54	41.5	S3	0.0491	3.04	f
RX J1130.0+3637	6945	11:30:02.789	+36:38:08.26	49.4	S3	0.0600	2.00	...
RX J1320.2+3308	6941	13:20:14.650	+33:08:33.06	38.6	S3	0.0366	1.01	e
RX J1347.5-1145	3592	13:47:30.593	-11:45:10.05	57.7	I3	0.4510	10.88	...
	507	10.0	S3
RX J1423.8+2404	1657	14:23:47.759	+24:04:40.45	18.5	I3	0.5450	5.92	...
	4195	115.6	S3
RX J1504.1-0248	5793	15:04:07.415	-02:48:15.70	39.2	I3	0.2150	8.00	...
RX J1532.9+3021	1649	15:32:53.781	+30:20:58.72	9.4	I3	0.3450	5.44	...
	1665	10.0	S3
RX J1539.5-8335	8266	15:39:32.485	-83:35:23.83	8.0	I3	0.0728	4.29	...
RX J1720.1+2638	4361	17:20:09.941	+26:37:29.11	25.7	I3	0.1640	6.37	...
RX J1720.2+3536	3280	17:20:16.953	+35:36:23.63	20.8	I3	0.3913	5.65	...
	6107	33.9	I3
	7225	2.0	I3
RX J1852.1+5711	5749	18:52:08.815	+57:11:42.63	29.8	I3	0.1094	3.66	...
RX J2129.6+0005	552	21:29:39.944	+00:05:18.83	10.0	I3	0.2350	5.91	...
RXCJ0331.1-2100	10790	03:31:06.020	-21:00:32.93	10.0	I3	0.1880	4.61	...
	9415	9.9	I3
SC 1327-312	4165	13:29:47.748	-31:36:23.54	18.4	I3	0.0531	3.53	f

Table 1—Continued

Cluster	Obs. ID	R.A. hr:min:sec	Decl. ° : ' : "	Exposure Time ksec	ACIS	z	kT_X keV	Notes
(1)	(2)	(3)	(4)	(5)	(6)	(7)	(8)	(9)
Sersic 159-03	1668	23:13:58.764	-42:43:34.70	9.9	S3	0.0580	2.65	...
SS2B153	3243	10:50:26.125	-12:50:41.76	29.5	S3	0.0186	0.80	...
UGC 3957	8265	07:40:58.335	+55:25:38.30	7.9	I3	0.0341	2.85	...
UGC 12491	7896	23:18:38.311	+42:57:29.06	32.7	S3	0.0174	0.87	...
ZWCL 1215	4184	12:17:41.708	+03:39:15.81	12.1	I3	0.0750	6.62	...
ZWCL 1358+6245	516	13:59:50.526	+62:31:04.57	54.1	S3	0.3280	10.66	...
ZWCL 1742	8267	17:44:14.515	+32:59:29.68	8.0	I3	0.0757	4.40	...
ZWCL 1953	1659	08:50:06.677	+36:04:16.16	24.9	I3	0.3800	7.37	...
ZWCL 3146	909	10:23:39.735	+04:11:08.05	46.0	I3	0.2900	7.48	...
ZWCL 7160	543	14:57:15.158	+22:20:33.85	9.9	I3	0.2578	4.53	...
Zwicky 2701	3195	09:52:49.183	+51:53:05.27	26.9	S3	0.2100	5.21	...
ZwCl 0857.9+2107	7897	09:00:36.835	+20:53:40.36	9.0	I3	0.2350	4.29	e

Note. — Col. (1) Cluster name; Col. (2) CXC CDA Observation Identification Number; Col. (3) R.A. of cluster center; Col. (4) Decl. of cluster center; Col. (5) exposure time; Col. (6) CCD location of cluster center; Col. (7) redshift; Col. (8) average cluster temperature; Col. (9) best-fit core entropy measured in this work; Col. (10) assigned notes: ‘a’ Clusters analyzed using the best-fit β -model for the surface brightness profiles (discussed in §3.2); ‘b’ Clusters with complex surface brightness of which only the central regions were used in fitting $K(r)$; ‘c’ Clusters only used during analysis of the *HIFLUGCS* sub-sample (discussed in §5.4); ‘d’ Clusters with central AGN removed during analysis (discussed in §3.5); ‘e’ Clusters with central compact source removed during analysis (discussed in §3.5); ‘f’ Clusters with central bin ignored during fitting (discussed in §3.5)..

Table 2. Summary of β -Model Fits

Cluster	S_{01} $10^{-6} \text{ cts s}^{-1} \text{ arcsec}^2$	r_{c1} "	β_1	S_{02} $10^{-6} \text{ cts s}^{-1} \text{ arcsec}^2$	r_{c2} "	β_2	D.O.F.	χ^2_{red}
(1)	(2)	(3)	(4)	(5)	(6)	(7)	(8)	(9)
Abell 119	4.93 ± 0.73	39.1 ± 15.3	0.34 ± 0.07	3.52 ± 0.96	735.2 ± 479.4	1.27 ± 1.27	52	1.76
Abell 160	2.32 ± 0.27	53.4 ± 11.1	0.57 ± 0.12	1.29 ± 0.22	284.0 ± 52.2	0.74 ± 0.10	90	1.18
Abell 193	24.72 ± 1.62	80.8 ± 2.2	0.43 ± 0.01	38	0.43
Abell 400	4.66 ± 0.09	151.3 ± 6.4	0.42 ± 0.01	96	0.57
Abell 1060	21.95 ± 0.44	93.5 ± 8.1	0.35 ± 0.01	42	1.44
Abell 1240	1.58 ± 0.07	247.9 ± 46.9	1.01 ± 0.22	58	1.58
Abell 1736	3.81 ± 0.56	55.6 ± 16.1	0.42 ± 0.12	2.49 ± 0.47	1470.0 ± 87.2	5.00 ± 0.73	35	1.58
Abell 2125	3.50 ± 0.20	26.0 ± 4.9	0.49 ± 0.05	1.02 ± 0.13	159.9 ± 9.2	1.32 ± 0.16	35	0.33
Abell 2255	8.38 ± 0.15	222.7 ± 9.8	0.62 ± 0.02	94	1.45
Abell 2256	21.69 ± 0.19	407.8 ± 17.9	0.99 ± 0.05	88	0.83
Abell 2319	47.39 ± 0.61	128.8 ± 3.1	0.49 ± 0.01	92	1.67
Abell 2462	8.19 ± 1.43	60.8 ± 9.6	0.64 ± 0.11	1.87 ± 0.25	762.7 ± 39.1	5.00 ± 0.87	67	1.54
Abell 2631	20.55 ± 1.01	66.0 ± 4.0	0.73 ± 0.03	58	1.15
Abell 3376	4.21 ± 0.09	125.5 ± 5.6	0.40 ± 0.01	98	1.42
Abell 3391	10.65 ± 0.31	132.3 ± 7.9	0.48 ± 0.01	84	1.86
Abell 3395	6.85 ± 0.67	90.9 ± 6.7	0.49 ± 0.03	38	0.96
MKW 8	7.71 ± 0.62	25.2 ± 2.5	0.32 ± 0.01	1.51 ± 0.08	1124.0 ± 64.1	5.00 ± 0.40	88	0.65
RBS 461	12.84 ± 0.34	102.2 ± 4.1	0.52 ± 0.01	84	1.56

Note. — Col. (1) Cluster name; col. (2) central surface brightness of first component; col. (3) core radius of first component; col. (4) β parameter of first component; col. (5) central surface brightness of second component; col. (6) core radius of second component; col. (7) β parameter of second component; col. (8) model degrees of freedom; and col. (9) reduced chi-squared statistic for best-fit model.

Table 3. M. Donahue’s H α Observations.

Cluster	Telescope	z	[NII]/H α	H α Flux 10 ⁻¹⁵ ergs s ⁻¹ cm ⁻²
Abell 85	PO	0.0558	2.67	0.581
Abell 119	LC	0.0442	...	<0.036
Abell 133	LC	0.0558	...	0.88
Abell 496	LC	0.0328	2.50	2.90
Abell 1644	LC	0.0471	...	1.00
Abell 1650	LC	0.0843	...	<0.029
Abell 1689	LC	0.1843	...	<0.029
Abell 1736	LC	0.0338	...	<0.026
Abell 2597	PO	0.0854	0.85	29.7
Abell 3112	LC	0.0720	2.22	2.66
Abell 3158	LC	0.0586	...	<0.036
Abell 3266	LC	0.0590	1.62	<0.027
Abell 4059	LC	0.0475	3.60	2.22
Cygnus A	PO	0.0561	1.85	28.4
EXO 0422-086	LC	0.0397	...	<0.031
Hydra A	LC	0.0522	0.85	13.4
PKS 0745-191	LC	0.1028	1.02	10.4

Note. — The abbreviation “PO” denotes observations taken on the 5 m Hale Telescope at the Palomar Observatory, USA, while “LC” are observations taken on the DuPont 2.5 m telescope at the Las Campanas Observatory, Chile. Upperlimits for H α fluxes are 3σ .

Table 4. Statistics of Best-Fit Parameters

Sample	N_{obj}	K_0 keV cm ²	K_{12} keV cm ²	K_{100} keV cm ²	α	1σ	$N_{K_0=0}$ 2σ	3σ
(1)	(2)	(3)	(4)	(5)	(6)	(7)	(8)	(9)
All K_0								
<i>ACCEPT</i>	233	72.9 ± 33.7	91.6 ± 35.7	126 ± 45	1.21 ± 0.39	4 (2%)	12 (5%)	24 (11%)
<i>HIFLUGCS</i>	59	62.3 ± 32.7	87.2 ± 34.5	166 ± 65	1.18 ± 0.38	1 (2%)	3 (5%)	4 (7%)
CSE	37	61.9 ± 27.4	81.6 ± 31.3	132 ± 45	1.19 ± 0.39	1 (3%)	2 (5%)	6 (16%)
β Models	17	220 ± 74	230 ± 76.9	67.4 ± 27.0	1.45 ± 0.47
$4 \text{ keV cm}^2 < K_0 \leq 50 \text{ keV cm}^2$								
<i>ACCEPT</i>	99	17.5 ± 5.8	31.2 ± 10.3	148 ± 49	1.21 ± 0.39	3 (3%)	5 (5%)	10 (10%)
<i>HIFLUGCS</i>	25	13.6 ± 4.6	29.4 ± 9.63	174 ± 57	1.15 ± 0.37	0 (0%)	0 (0%)	0 (0%)
CSE	17	16.4 ± 5.4	30.9 ± 10.2	146 ± 48	1.19 ± 0.38	0 (0%)	0 (0%)	2 (12%)
$K_0 \leq 50 \text{ keV cm}^2$								
<i>ACCEPT</i>	107	16.1 ± 5.7	30.5 ± 10.0	150 ± 50	1.20 ± 0.38	4 (4%)	6 (6%)	11 (10%)
<i>HIFLUGCS</i>	29	11.4 ± 4.2	31.2 ± 10.5	235 ± 89	1.17 ± 0.37	1 (4%)	1 (4%)	1 (4%)
CSE	19	15.6 ± 5.2	30.9 ± 10.2	146 ± 48	1.16 ± 0.38	1 (5%)	1 (5%)	3 (16%)
$K_0 > 50 \text{ keV cm}^2$								
<i>ACCEPT</i>	126	156 ± 54	175 ± 59	107 ± 39	1.23 ± 0.40	0 (0%)	6 (5%)	13 (11%)
<i>HIFLUGCS</i>	30	151 ± 53	172 ± 58	113 ± 43	1.19 ± 0.39	0 (0%)	2 (7%)	3 (10%)
CSE	18	148 ± 49	165 ± 54	118 ± 42	1.23 ± 0.40	0 (0%)	1 (6%)	3 (17%)

Note. — isted here are the mean best-fit parameters of the model $K(r) = K_0 + K_{100}(r/100 \text{ kpc})^\alpha$ for various sub-groups of the full *ACCEPT* sample. Each sub-group is labeled in the table. The 'CSE' sample are the clusters with a central source excluded (discussed in §3.5). The K_{12} values represent the entropy at 12 kpc and are calculated from the best-fit models. Col. (1) Sample being considered; col. (2) number of objects in the sub-group; col. (3) mean best-fit K_0 ; col. (4) mean entropy at 12 kpc; col. (5) mean best-fit K_{100} ; and col. (6) mean best-fit power-law index; cols. (7,8,9) number of clusters consistent with $K_0 = 0 \text{ keV cm}^2$ at 1σ , 2σ , and 3σ significance, respectively. Percentage of the sub-group represented by each is also listed.

Table 5. Summary of Entropy Profile Fits

Cluster	Method	N_{bins}	r_{max} Mpc	K_0 keV cm ²	$\sigma_{K_0} > 0$	K_{100} keV cm ²	α	DOF	χ^2	p-value
(1)	(2)	(3)	(4)	(5)	(6)	(7)	(8)	(9)	(10)	(11)
1E0657 56	extr	48	1.00	299.4 ± 19.6	15.3	20.5 ± 7.0	1.84 ± 0.16	45	42.09	5.96e-01
	-	-	-	0.0	-	277.9 ± 14.5	0.60 ± 0.04	46	146.18	2.31e-12
	flat	-	-	307.5 ± 19.3	15.9	18.6 ± 6.5	1.88 ± 0.17	45	42.87	5.63e-01
2A 335+096	-	-	-	0.0	-	283.6 ± 14.6	0.58 ± 0.04	46	157.03	4.77e-14
	extr	37	0.12	5.3 ± 0.2	34.8	137.7 ± 1.9	1.43 ± 0.02	34	173.51	1.26e-20
	-	-	-	0.0	-	117.7 ± 1.5	1.06 ± 0.01	35	1188.38	6.24e-227
2PIGG J0011.5-2850	flat	-	-	7.1 ± 0.1	49.3	138.6 ± 1.9	1.52 ± 0.02	34	209.16	4.39e-27
	-	-	-	0.0	-	107.4 ± 1.4	0.97 ± 0.01	35	2097.26	0.00e+00
	extr	27	0.20	75.3 ± 44.8	1.7	236.9 ± 53.2	0.82 ± 0.27	24	2.01	1.00e+00
2PIGG J2227.0-3041	-	-	-	0.0	-	318.5 ± 13.6	0.53 ± 0.06	25	3.19	1.00e+00
	flat	-	-	102.0 ± 42.9	2.4	214.7 ± 51.5	0.84 ± 0.29	24	2.79	1.00e+00
	-	-	-	0.0	-	323.8 ± 13.7	0.45 ± 0.05	25	4.40	1.00e+00
3C 28.0	extr	23	0.15	12.5 ± 1.0	12.3	119.5 ± 3.6	1.32 ± 0.06	20	13.14	8.71e-01
	-	-	-	0.0	-	118.4 ± 3.3	0.88 ± 0.02	21	132.53	3.43e-18
	flat	-	-	17.1 ± 1.0	17.4	113.9 ± 3.6	1.37 ± 0.06	20	11.50	9.32e-01
3C 295	-	-	-	0.0	-	108.6 ± 3.1	0.73 ± 0.02	21	202.76	1.04e-31
	extr	12	0.18	20.7 ± 1.3	15.5	111.7 ± 3.9	1.70 ± 0.09	9	23.42	5.32e-03
	-	-	-	0.0	-	115.3 ± 3.4	0.82 ± 0.03	10	151.06	2.25e-27
3C 388	flat	-	-	23.9 ± 1.3	18.6	107.8 ± 3.9	1.79 ± 0.09	9	22.93	6.35e-03
	-	-	-	0.0	-	110.8 ± 3.3	0.74 ± 0.03	10	179.58	2.86e-33
	extr	17	0.50	12.6 ± 2.6	4.9	84.5 ± 6.4	1.45 ± 0.07	14	7.52	9.13e-01
3C 388	-	-	-	0.0	-	108.2 ± 3.8	1.20 ± 0.04	15	27.39	2.57e-02
	flat	-	-	14.5 ± 2.5	5.8	81.9 ± 6.3	1.47 ± 0.07	14	8.36	8.70e-01
	-	-	-	0.0	-	109.3 ± 3.8	1.18 ± 0.04	15	34.84	2.59e-03
4C 55.16	extr	24	0.20	17.0 ± 5.7	3.0	214.2 ± 8.5	0.76 ± 0.07	21	10.82	9.66e-01
	-	-	-	0.0	-	226.3 ± 7.0	0.60 ± 0.02	22	16.13	8.09e-01
	flat	-	-	17.0 ± 5.8	3.0	214.3 ± 8.5	0.76 ± 0.07	21	10.90	9.65e-01
Abell 13	-	-	-	0.0	-	226.4 ± 7.0	0.60 ± 0.02	22	16.14	8.09e-01
	extr	21	0.40	22.4 ± 2.9	7.7	162.9 ± 7.7	1.28 ± 0.06	18	7.52	9.85e-01
	-	-	-	0.0	-	197.1 ± 5.6	0.94 ± 0.03	19	46.97	3.61e-04
Abell 68	flat	-	-	23.3 ± 2.9	8.1	161.6 ± 7.7	1.29 ± 0.06	18	7.92	9.80e-01
	-	-	-	0.0	-	197.0 ± 5.6	0.93 ± 0.03	19	50.60	1.07e-04
	extr	35	0.30	182.6 ± 26.2	7.0	182.0 ± 36.8	1.37 ± 0.22	32	11.58	1.00e+00
Abell 85	-	-	-	0.0	-	401.9 ± 14.1	0.59 ± 0.05	33	32.03	5.15e-01
	flat	-	-	182.6 ± 26.2	7.0	182.0 ± 36.8	1.37 ± 0.22	32	11.58	1.00e+00
	-	-	-	0.0	-	401.9 ± 14.1	0.59 ± 0.05	33	32.03	5.15e-01
Abell 13	extr	31	0.60	217.3 ± 89.0	2.4	142.3 ± 98.3	0.89 ± 0.39	28	1.72	1.00e+00
	-	-	-	0.0	-	393.4 ± 36.9	0.40 ± 0.08	29	3.45	1.00e+00
	flat	-	-	217.3 ± 89.0	2.4	142.3 ± 98.3	0.89 ± 0.39	28	1.72	1.00e+00
Abell 68	-	-	-	0.0	-	393.4 ± 36.9	0.40 ± 0.08	29	3.45	1.00e+00
	extr	39	0.20	7.3 ± 0.6	12.8	165.5 ± 1.9	1.05 ± 0.02	36	52.57	3.67e-02
	-	-	-	0.0	-	170.2 ± 1.8	0.90 ± 0.01	37	201.42	1.67e-24
Abell 85	flat	-	-	12.5 ± 0.5	23.7	158.8 ± 1.9	1.12 ± 0.02	36	59.03	9.10e-03

Table 5—Continued

Cluster	Method	N_{bins}	r_{max} Mpc	K_0 keV cm ²	$\sigma_{K_0} > 0$	K_{100} keV cm ²	α	DOF	χ^2	p-value
(1)	(2)	(3)	(4)	(5)	(6)	(7)	(8)	(9)	(10)	(11)
Abell 119	-	-	-	0.0	-	165.5 ± 1.8	0.83 ± 0.01	37	492.25	6.48e-81
	extr	23	0.20	210.1 ± 84.5	2.5	207.1 ± 100.1	0.77 ± 0.56	20	0.12	1.00e+00
	-	-	-	0.0	-	418.7 ± 31.2	0.26 ± 0.07	21	1.34	1.00e+00
	flat	-	-	233.9 ± 87.7	2.7	191.3 ± 102.8	0.75 ± 0.61	20	0.10	1.00e+00
Abell 133	-	-	-	0.0	-	425.5 ± 31.1	0.22 ± 0.06	21	1.19	1.00e+00
	extr	20	0.10	13.3 ± 0.5	25.1	170.7 ± 3.9	1.47 ± 0.04	17	44.38	3.01e-04
	-	-	-	0.0	-	142.2 ± 2.7	0.90 ± 0.01	18	504.69	1.08e-95
	flat	-	-	17.3 ± 0.5	35.0	170.1 ± 4.1	1.59 ± 0.04	17	54.26	9.02e-06
Abell 141	-	-	-	0.0	-	127.5 ± 2.5	0.79 ± 0.01	18	812.02	8.79e-161
	extr	33	0.60	144.1 ± 31.3	4.6	68.5 ± 27.5	1.53 ± 0.27	30	136.92	1.32e-15
	-	-	-	0.0	-	221.9 ± 18.4	0.77 ± 0.09	31	447.75	2.25e-75
	flat	-	-	205.0 ± 27.4	7.5	42.6 ± 20.8	1.78 ± 0.33	30	175.31	1.84e-22
Abell 160	-	-	-	0.0	-	269.7 ± 17.7	0.57 ± 0.07	31	704.66	2.56e-128
	extr	28	0.12	155.8 ± 27.7	5.6	116.3 ± 29.2	0.98 ± 0.57	25	0.33	1.00e+00
	-	-	-	0.0	-	254.7 ± 13.5	0.20 ± 0.04	26	3.66	1.00e+00
	flat	-	-	155.8 ± 27.7	5.6	116.3 ± 29.2	0.98 ± 0.57	25	0.33	1.00e+00
Abell 193	-	-	-	0.0	-	254.7 ± 13.5	0.20 ± 0.04	26	3.66	1.00e+00
	extr	26	0.12	185.5 ± 13.3	13.9	36.0 ± 16.8	2.23 ± 1.89	23	0.02	1.00e+00
	-	-	-	0.0	-	213.8 ± 7.3	0.09 ± 0.04	24	2.92	1.00e+00
	flat	-	-	185.5 ± 13.3	13.9	36.0 ± 16.8	2.23 ± 1.89	23	0.02	1.00e+00
Abell 209	-	-	-	0.0	-	213.8 ± 7.3	0.09 ± 0.04	24	2.92	1.00e+00
	extr	19	0.30	100.7 ± 26.3	3.8	150.5 ± 34.5	0.81 ± 0.21	16	2.48	1.00e+00
	-	-	-	0.0	-	266.2 ± 9.6	0.40 ± 0.04	17	7.88	9.69e-01
	flat	-	-	105.5 ± 26.9	3.9	149.3 ± 35.2	0.80 ± 0.21	16	2.73	1.00e+00
Abell 222	-	-	-	0.0	-	269.5 ± 9.6	0.38 ± 0.04	17	8.03	9.66e-01
	extr	37	0.60	122.2 ± 15.2	8.0	84.8 ± 19.2	0.99 ± 0.15	34	4.82	1.00e+00
	-	-	-	0.0	-	231.9 ± 7.3	0.40 ± 0.03	35	26.22	8.58e-01
	flat	-	-	126.0 ± 15.0	8.4	82.2 ± 19.0	1.00 ± 0.15	34	4.94	1.00e+00
Abell 223	-	-	-	0.0	-	233.9 ± 7.3	0.39 ± 0.03	35	27.16	8.26e-01
	extr	30	0.50	183.9 ± 46.1	4.0	160.7 ± 59.2	1.24 ± 0.31	27	1.35	1.00e+00
	-	-	-	0.0	-	386.1 ± 23.5	0.57 ± 0.08	28	6.55	1.00e+00
	flat	-	-	183.9 ± 46.1	4.0	160.7 ± 59.2	1.24 ± 0.31	27	1.35	1.00e+00
Abell 262	-	-	-	0.0	-	386.1 ± 23.5	0.57 ± 0.08	28	6.55	1.00e+00
	extr	30	0.05	9.4 ± 0.8	11.8	200.9 ± 7.3	0.95 ± 0.04	27	52.37	2.40e-03
	-	-	-	0.0	-	166.6 ± 3.3	0.66 ± 0.01	28	159.48	2.36e-20
	flat	-	-	10.6 ± 0.8	13.8	205.1 ± 7.9	0.98 ± 0.04	27	60.17	2.50e-04
Abell 267	-	-	-	0.0	-	164.3 ± 3.3	0.65 ± 0.01	28	199.73	7.70e-28
	extr	22	0.40	168.3 ± 17.7	9.5	52.0 ± 21.1	1.82 ± 0.38	19	0.62	1.00e+00
	-	-	-	0.0	-	263.4 ± 11.7	0.41 ± 0.06	20	22.64	3.07e-01
	flat	-	-	168.6 ± 17.6	9.6	51.8 ± 21.0	1.82 ± 0.38	19	0.62	1.00e+00
Abell 368	-	-	-	0.0	-	263.5 ± 11.7	0.40 ± 0.06	20	22.71	3.03e-01
	extr	28	0.50	47.5 ± 8.3	5.7	146.7 ± 15.4	1.20 ± 0.11	25	6.13	1.00e+00
	-	-	-	0.0	-	216.8 ± 8.0	0.77 ± 0.04	26	24.09	5.71e-01
	flat	-	-	50.9 ± 8.2	6.2	144.1 ± 15.4	1.21 ± 0.11	25	6.18	1.00e+00

Table 5—Continued

Cluster	Method	N_{bins}	r_{max} Mpc	K_0 keV cm ²	$\sigma_{K_0} > 0$	K_{100} keV cm ²	α	DOF	χ^2	p-value
(1)	(2)	(3)	(4)	(5)	(6)	(7)	(8)	(9)	(10)	(11)
Abell 370	-	-	-	0.0	-	218.7 ± 8.0	0.74 ± 0.04	26	26.03	4.61e-01
	extr	20	0.50	321.9 ± 90.8	3.5	78.7 ± 89.3	1.24 ± 0.68	17	2.41	1.00e+00
	-	-	-	0.0	-	422.4 ± 34.9	0.40 ± 0.08	18	6.02	9.96e-01
	flat	-	-	321.9 ± 90.8	3.5	78.7 ± 89.3	1.24 ± 0.68	17	2.41	1.00e+00
Abell 383	-	-	-	0.0	-	422.4 ± 34.9	0.40 ± 0.08	18	6.02	9.96e-01
	extr	13	0.20	10.9 ± 1.6	6.6	114.0 ± 5.2	1.34 ± 0.09	10	4.76	9.07e-01
	-	-	-	0.0	-	121.4 ± 4.9	0.96 ± 0.04	11	40.90	2.50e-05
	flat	-	-	13.0 ± 1.6	8.3	110.9 ± 5.2	1.40 ± 0.09	10	6.30	7.89e-01
Abell 399	-	-	-	0.0	-	119.2 ± 4.9	0.92 ± 0.03	11	58.48	1.78e-08
	extr	31	0.20	140.3 ± 19.1	7.3	215.3 ± 22.7	0.73 ± 0.12	28	4.14	1.00e+00
	-	-	-	0.0	-	360.8 ± 7.0	0.32 ± 0.02	29	21.40	8.44e-01
	flat	-	-	153.2 ± 18.8	8.2	204.3 ± 22.4	0.74 ± 0.12	28	4.19	1.00e+00
Abell 400	-	-	-	0.0	-	362.5 ± 7.0	0.30 ± 0.02	29	22.24	8.10e-01
	extr	73	0.18	162.8 ± 3.9	41.6	35.3 ± 5.7	1.76 ± 0.28	70	0.71	1.00e+00
	-	-	-	0.0	-	205.9 ± 2.1	0.17 ± 0.01	71	57.23	8.82e-01
	flat	-	-	162.8 ± 3.9	41.6	35.3 ± 5.7	1.76 ± 0.28	70	0.71	1.00e+00
Abell 401	-	-	-	0.0	-	205.9 ± 2.1	0.17 ± 0.01	71	57.23	8.82e-01
	extr	60	0.40	162.5 ± 7.9	20.7	86.0 ± 10.7	1.37 ± 0.11	57	8.70	1.00e+00
	-	-	-	0.0	-	290.7 ± 4.7	0.43 ± 0.02	58	134.73	4.81e-08
	flat	-	-	166.9 ± 7.7	21.7	81.8 ± 10.4	1.40 ± 0.11	57	8.36	1.00e+00
Abell 426	-	-	-	0.0	-	292.0 ± 4.7	0.42 ± 0.02	58	142.56	4.50e-09
	extr	56	0.10	19.4 ± 0.2	124.3	119.9 ± 0.5	1.74 ± 0.01	53	1040.29	3.10e-183
	-	-	-	0.0	-	112.3 ± 0.3	0.92 ± 0.00	54	6430.00	0.00e+00
	flat	-	-	19.4 ± 0.2	124.4	119.9 ± 0.5	1.74 ± 0.01	53	1045.73	2.32e-184
Abell 478	-	-	-	0.0	-	112.3 ± 0.3	0.92 ± 0.00	54	6447.72	0.00e+00
	extr	49	0.40	6.9 ± 0.9	7.5	123.4 ± 2.6	0.96 ± 0.02	46	20.38	1.00e+00
	-	-	-	0.0	-	136.7 ± 1.7	0.84 ± 0.01	47	66.62	3.13e-02
	flat	-	-	7.8 ± 0.9	8.5	122.0 ± 2.6	0.97 ± 0.02	46	22.58	9.99e-01
Abell 496	-	-	-	0.0	-	137.0 ± 1.7	0.84 ± 0.01	47	81.79	1.25e-03
	extr	26	0.08	4.3 ± 0.8	5.7	206.1 ± 9.2	1.13 ± 0.04	23	7.05	9.99e-01
	-	-	-	0.0	-	182.9 ± 6.6	0.94 ± 0.02	24	36.09	5.38e-02
	flat	-	-	8.9 ± 0.7	13.4	216.3 ± 10.5	1.27 ± 0.05	23	6.95	1.00e+00
Abell 520	-	-	-	0.0	-	161.2 ± 5.8	0.83 ± 0.02	24	132.18	6.24e-17
	extr	33	0.55	325.5 ± 29.2	11.1	10.2 ± 11.8	2.09 ± 0.71	30	2.86	1.00e+00
	-	-	-	0.0	-	328.7 ± 18.7	0.29 ± 0.05	31	14.09	9.96e-01
	flat	-	-	325.5 ± 29.2	11.1	10.2 ± 11.8	2.09 ± 0.71	30	2.86	1.00e+00
Abell 521	-	-	-	0.0	-	328.7 ± 18.7	0.29 ± 0.05	31	14.09	9.96e-01
	extr	8	0.15	201.6 ± 36.1	5.6	235.7 ± 61.8	1.92 ± 0.72	5	0.23	9.99e-01
	-	-	-	0.0	-	420.3 ± 37.9	0.44 ± 0.10	6	9.70	1.38e-01
	flat	-	-	259.9 ± 36.2	7.2	245.4 ± 61.8	1.91 ± 0.69	5	0.32	9.97e-01
Abell 539	-	-	-	0.0	-	481.0 ± 37.3	0.35 ± 0.08	6	11.51	7.39e-02
	extr	11	0.03	19.6 ± 4.0	4.9	552.4 ± 198.3	1.14 ± 0.21	8	1.80	9.86e-01
	-	-	-	0.0	-	241.9 ± 31.9	0.58 ± 0.05	9	10.03	3.48e-01
	flat	-	-	22.6 ± 4.5	5.0	493.3 ± 165.6	1.05 ± 0.20	8	2.12	9.77e-01

Table 5—Continued

Cluster	Method	N_{bins}	r_{max} Mpc	K_0 keV cm ²	$\sigma_{K_0} > 0$	K_{100} keV cm ²	α	DOF	χ^2	p-value
(1)	(2)	(3)	(4)	(5)	(6)	(7)	(8)	(9)	(10)	(11)
Abell 562	-	-	-	0.0	-	234.5 \pm 27.5	0.53 \pm 0.04	9	10.08	3.44e-01
	extr	27	0.27	202.1 \pm 39.3	5.1	34.6 \pm 45.3	1.09 \pm 1.19	24	1.66	1.00e+00
	-	-	-	0.0	-	244.4 \pm 9.7	0.13 \pm 0.06	25	2.41	1.00e+00
	flat	-	-	202.1 \pm 39.3	5.1	34.6 \pm 45.3	1.09 \pm 1.19	24	1.66	1.00e+00
Abell 576	-	-	-	0.0	-	244.4 \pm 9.7	0.13 \pm 0.06	25	2.41	1.00e+00
	extr	21	0.08	78.4 \pm 18.7	4.2	230.6 \pm 26.6	1.19 \pm 0.34	18	3.81	1.00e+00
	-	-	-	0.0	-	259.8 \pm 16.1	0.51 \pm 0.06	19	10.60	9.37e-01
	flat	-	-	95.3 \pm 15.4	6.2	221.2 \pm 31.5	1.41 \pm 0.41	18	4.71	9.99e-01
Abell 586	-	-	-	0.0	-	247.8 \pm 15.2	0.45 \pm 0.06	19	15.49	6.91e-01
	extr	17	0.25	94.7 \pm 19.2	4.9	92.1 \pm 25.5	1.25 \pm 0.32	14	3.47	9.98e-01
	-	-	-	0.0	-	201.4 \pm 7.2	0.53 \pm 0.06	15	10.34	7.98e-01
	flat	-	-	94.7 \pm 19.2	4.9	92.1 \pm 25.5	1.25 \pm 0.32	14	3.47	9.98e-01
Abell 611	-	-	-	0.0	-	201.4 \pm 7.2	0.53 \pm 0.06	15	10.34	7.98e-01
	extr	19	0.40	124.9 \pm 18.6	6.7	164.4 \pm 31.5	1.25 \pm 0.20	16	1.98	1.00e+00
	-	-	-	0.0	-	326.7 \pm 15.2	0.53 \pm 0.05	17	14.90	6.02e-01
	flat	-	-	124.9 \pm 18.6	6.7	164.4 \pm 31.5	1.25 \pm 0.20	16	1.98	1.00e+00
Abell 644	-	-	-	0.0	-	326.7 \pm 15.2	0.53 \pm 0.05	17	14.90	6.02e-01
	extr	53	0.35	132.4 \pm 9.1	14.5	85.9 \pm 11.7	1.55 \pm 0.13	50	15.09	1.00e+00
	-	-	-	0.0	-	244.8 \pm 4.3	0.68 \pm 0.03	51	90.43	5.59e-04
	flat	-	-	132.4 \pm 9.1	14.5	85.9 \pm 11.7	1.55 \pm 0.13	50	15.09	1.00e+00
Abell 665	-	-	-	0.0	-	244.8 \pm 4.3	0.68 \pm 0.03	51	90.43	5.59e-04
	extr	46	0.70	134.6 \pm 23.5	5.7	106.3 \pm 25.1	1.06 \pm 0.13	43	3.79	1.00e+00
	-	-	-	0.0	-	254.8 \pm 10.1	0.61 \pm 0.04	44	19.71	9.99e-01
	flat	-	-	134.6 \pm 23.5	5.7	106.3 \pm 25.1	1.06 \pm 0.13	43	3.79	1.00e+00
Abell 697	-	-	-	0.0	-	254.8 \pm 10.1	0.61 \pm 0.04	44	19.71	9.99e-01
	extr	30	0.60	161.0 \pm 24.7	6.5	111.1 \pm 29.5	1.09 \pm 0.18	27	4.01	1.00e+00
	-	-	-	0.0	-	310.0 \pm 13.4	0.46 \pm 0.04	28	19.49	8.82e-01
	flat	-	-	166.7 \pm 24.4	6.8	108.2 \pm 29.1	1.10 \pm 0.18	27	4.28	1.00e+00
Abell 744	-	-	-	0.0	-	313.9 \pm 13.3	0.45 \pm 0.04	28	20.28	8.54e-01
	extr	18	0.12	60.3 \pm 9.4	6.4	227.9 \pm 15.4	0.83 \pm 0.13	15	1.20	1.00e+00
	-	-	-	0.0	-	251.0 \pm 11.7	0.41 \pm 0.03	16	13.36	6.46e-01
	flat	-	-	63.4 \pm 10.2	6.2	229.3 \pm 15.2	0.79 \pm 0.13	15	1.27	1.00e+00
Abell 754	-	-	-	0.0	-	256.9 \pm 11.5	0.39 \pm 0.02	16	12.56	7.05e-01
	extr	58	0.30	270.4 \pm 23.8	11.4	69.7 \pm 26.5	1.48 \pm 0.34	55	13.35	1.00e+00
	-	-	-	0.0	-	366.4 \pm 8.1	0.34 \pm 0.03	56	35.36	9.86e-01
	flat	-	-	270.4 \pm 23.8	11.4	69.7 \pm 26.5	1.48 \pm 0.34	55	13.35	1.00e+00
Abell 773	-	-	-	0.0	-	366.4 \pm 8.1	0.34 \pm 0.03	56	35.36	9.86e-01
	extr	35	0.60	244.3 \pm 31.7	7.7	41.1 \pm 22.5	1.60 \pm 0.33	32	3.28	1.00e+00
	-	-	-	0.0	-	283.2 \pm 16.6	0.54 \pm 0.06	33	19.39	9.71e-01
	flat	-	-	244.3 \pm 31.7	7.7	41.1 \pm 22.5	1.60 \pm 0.33	32	3.28	1.00e+00
Abell 907	-	-	-	0.0	-	283.2 \pm 16.6	0.54 \pm 0.06	33	19.39	9.71e-01
	extr	31	0.40	20.4 \pm 3.3	6.1	191.5 \pm 8.1	1.02 \pm 0.05	28	7.33	1.00e+00
	-	-	-	0.0	-	223.9 \pm 5.4	0.81 \pm 0.02	29	32.96	2.79e-01
	flat	-	-	23.4 \pm 3.2	7.3	187.0 \pm 8.1	1.05 \pm 0.05	28	7.62	1.00e+00

Table 5—Continued

Cluster	Method	N_{bins}	r_{max} Mpc	K_0 keV cm ²	$\sigma_{K_0} > 0$	K_{100} keV cm ²	α	DOF	χ^2	p-value
(1)	(2)	(3)	(4)	(5)	(6)	(7)	(8)	(9)	(10)	(11)
Abell 963	-	-	-	0.0	-	224.1 ± 5.4	0.79 ± 0.02	29	41.74	5.92e-02
	extr	24	0.40	22.0 ± 15.7	1.4	205.5 ± 22.9	0.79 ± 0.09	21	2.75	1.00e+00
	-	-	-	0.0	-	234.8 ± 7.8	0.68 ± 0.04	22	4.30	1.00e+00
	flat	-	-	55.8 ± 12.9	4.3	169.1 ± 20.3	0.90 ± 0.10	21	3.37	1.00e+00
Abell 1060	-	-	-	0.0	-	244.6 ± 7.6	0.61 ± 0.03	22	13.86	9.06e-01
	extr	25	0.03	58.1 ± 8.8	6.6	138.8 ± 40.0	0.80 ± 0.30	22	1.55	1.00e+00
	-	-	-	0.0	-	134.9 ± 7.7	0.21 ± 0.03	23	7.68	9.99e-01
	flat	-	-	72.0 ± 5.2	13.8	178.3 ± 100.9	1.25 ± 0.49	22	2.61	1.00e+00
Abell 1063S	-	-	-	0.0	-	121.7 ± 6.6	0.15 ± 0.02	23	13.85	9.31e-01
	extr	24	0.60	169.6 ± 19.7	8.6	42.2 ± 17.7	1.72 ± 0.27	21	2.98	1.00e+00
	-	-	-	0.0	-	235.3 ± 13.3	0.63 ± 0.06	22	34.40	4.47e-02
	flat	-	-	169.6 ± 19.7	8.6	42.2 ± 17.7	1.72 ± 0.27	21	2.98	1.00e+00
Abell 1068	-	-	-	0.0	-	235.3 ± 13.3	0.63 ± 0.06	22	34.40	4.47e-02
	extr	17	0.20	9.0 ± 1.0	8.7	108.9 ± 3.2	1.31 ± 0.06	14	3.45	9.98e-01
	-	-	-	0.0	-	116.5 ± 3.0	0.96 ± 0.03	15	53.28	3.46e-06
	flat	-	-	9.1 ± 1.0	8.8	108.8 ± 3.2	1.31 ± 0.06	14	3.44	9.98e-01
Abell 1201	-	-	-	0.0	-	116.5 ± 3.0	0.96 ± 0.03	15	54.19	2.44e-06
	extr	14	0.20	39.2 ± 14.0	2.8	200.4 ± 23.8	1.20 ± 0.21	11	1.60	1.00e+00
	-	-	-	0.0	-	245.2 ± 15.1	0.81 ± 0.08	12	6.57	8.85e-01
	flat	-	-	64.8 ± 16.9	3.8	198.9 ± 25.2	1.03 ± 0.21	11	2.19	9.98e-01
Abell 1204	-	-	-	0.0	-	262.1 ± 15.3	0.56 ± 0.05	12	8.39	7.54e-01
	extr	11	0.15	14.1 ± 1.5	9.5	83.1 ± 3.6	1.35 ± 0.11	8	1.62	9.91e-01
	-	-	-	0.0	-	87.9 ± 3.2	0.75 ± 0.03	9	54.35	1.62e-08
	flat	-	-	15.3 ± 1.4	10.8	81.8 ± 3.6	1.40 ± 0.11	8	1.91	9.84e-01
Abell 1240	-	-	-	0.0	-	86.7 ± 3.2	0.73 ± 0.03	9	65.62	1.09e-10
	extr	37	0.50	429.4 ± 46.9	9.1	16.9 ± 28.8	1.96 ± 1.14	34	0.06	1.00e+00
	-	-	-	0.0	-	482.7 ± 27.4	0.17 ± 0.06	35	4.78	1.00e+00
	flat	-	-	462.4 ± 41.7	11.1	8.3 ± 18.2	2.37 ± 1.48	34	0.03	1.00e+00
Abell 1361	-	-	-	0.0	-	504.2 ± 26.9	0.13 ± 0.05	35	4.76	1.00e+00
	extr	14	0.15	14.8 ± 4.3	3.4	119.2 ± 10.7	1.15 ± 0.19	11	3.47	9.83e-01
	-	-	-	0.0	-	121.7 ± 9.4	0.74 ± 0.06	12	12.04	4.43e-01
	flat	-	-	18.6 ± 4.9	3.8	117.9 ± 10.5	1.06 ± 0.18	11	4.08	9.68e-01
Abell 1413	-	-	-	0.0	-	122.2 ± 8.9	0.63 ± 0.05	12	13.17	3.57e-01
	extr	10	0.12	29.8 ± 13.9	2.1	158.2 ± 14.7	0.82 ± 0.20	7	5.97	5.43e-01
	-	-	-	0.0	-	179.6 ± 10.0	0.54 ± 0.05	8	11.45	1.77e-01
	flat	-	-	64.0 ± 8.3	7.7	123.2 ± 13.0	1.19 ± 0.28	7	6.18	5.19e-01
Abell 1423	-	-	-	0.0	-	164.1 ± 9.2	0.38 ± 0.04	8	25.44	1.31e-03
	extr	23	0.40	58.8 ± 12.6	4.7	124.8 ± 20.9	1.22 ± 0.17	20	1.75	1.00e+00
	-	-	-	0.0	-	205.5 ± 9.7	0.73 ± 0.06	21	15.66	7.88e-01
	flat	-	-	68.3 ± 12.9	5.3	124.2 ± 21.1	1.20 ± 0.17	20	1.67	1.00e+00
Abell 1446	-	-	-	0.0	-	215.6 ± 9.7	0.65 ± 0.05	21	17.39	6.87e-01
	extr	34	0.32	152.4 ± 43.8	3.5	119.5 ± 49.5	0.67 ± 0.27	31	6.87	1.00e+00
	-	-	-	0.0	-	282.4 ± 8.4	0.26 ± 0.04	32	9.71	1.00e+00
	flat	-	-	152.4 ± 43.8	3.5	119.5 ± 49.5	0.67 ± 0.27	31	6.87	1.00e+00

Table 5—Continued

Cluster	Method	N_{bins}	r_{max} Mpc	K_0 keV cm ²	$\sigma_{K_0} > 0$	K_{100} keV cm ²	α	DOF	χ^2	p-value
(1)	(2)	(3)	(4)	(5)	(6)	(7)	(8)	(9)	(10)	(11)
Abell 1569	-	-	-	0.0	-	282.4 ± 8.4	0.26 ± 0.04	32	9.71	1.00e+00
	extr	29	0.20	110.1 ± 27.8	4.0	149.1 ± 28.9	0.51 ± 0.19	26	7.39	1.00e+00
	-	-	-	0.0	-	253.7 ± 9.5	0.20 ± 0.02	27	9.59	9.99e-01
	flat	-	-	110.1 ± 27.8	4.0	149.1 ± 28.9	0.51 ± 0.19	26	7.39	1.00e+00
Abell 1576	-	-	-	0.0	-	253.7 ± 9.5	0.20 ± 0.02	27	9.59	9.99e-01
	extr	33	0.70	174.1 ± 49.7	3.5	102.3 ± 48.5	1.36 ± 0.29	30	41.88	7.32e-02
	-	-	-	0.0	-	286.9 ± 27.0	0.77 ± 0.09	31	250.93	2.94e-36
	flat	-	-	186.2 ± 49.1	3.8	98.3 ± 47.6	1.38 ± 0.29	30	41.62	7.71e-02
Abell 1644	-	-	-	0.0	-	297.3 ± 26.9	0.74 ± 0.09	31	272.38	2.10e-40
	extr	11	0.05	10.7 ± 1.3	8.2	511.4 ± 61.2	1.54 ± 0.10	8	0.50	1.00e+00
	-	-	-	0.0	-	293.9 ± 22.4	1.02 ± 0.04	9	43.93	1.45e-06
	flat	-	-	19.0 ± 1.2	16.4	585.7 ± 81.8	1.76 ± 0.11	8	1.25	9.96e-01
Abell 1650	-	-	-	0.0	-	177.6 ± 12.5	0.71 ± 0.03	9	108.10	3.58e-19
	extr	15	0.12	32.7 ± 10.8	3.0	164.9 ± 12.3	0.80 ± 0.16	12	1.85	1.00e+00
	-	-	-	0.0	-	185.9 ± 9.1	0.49 ± 0.04	13	6.09	9.43e-01
	flat	-	-	38.0 ± 10.0	3.8	159.9 ± 12.1	0.84 ± 0.17	12	2.00	9.99e-01
Abell 1651	-	-	-	0.0	-	183.7 ± 9.0	0.47 ± 0.04	13	7.85	8.53e-01
	extr	27	0.20	87.7 ± 11.2	7.8	117.3 ± 15.3	0.96 ± 0.18	24	13.05	9.65e-01
	-	-	-	0.0	-	207.6 ± 6.7	0.34 ± 0.03	25	28.85	2.70e-01
	flat	-	-	89.5 ± 11.1	8.1	115.5 ± 15.2	0.97 ± 0.19	24	13.26	9.62e-01
Abell 1664	-	-	-	0.0	-	207.6 ± 6.7	0.34 ± 0.03	25	29.42	2.47e-01
	extr	13	0.15	10.0 ± 1.1	9.1	142.7 ± 5.9	1.50 ± 0.08	10	27.58	2.11e-03
	-	-	-	0.0	-	127.9 ± 4.9	0.97 ± 0.03	11	82.78	4.27e-13
	flat	-	-	14.4 ± 1.0	14.8	141.8 ± 6.1	1.70 ± 0.09	10	16.24	9.31e-02
Abell 1689	-	-	-	0.0	-	117.2 ± 4.6	0.85 ± 0.03	11	127.13	6.63e-22
	extr	20	0.30	78.4 ± 7.6	10.4	111.8 ± 13.8	1.35 ± 0.14	17	7.34	9.79e-01
	-	-	-	0.0	-	218.8 ± 6.3	0.62 ± 0.03	18	52.72	2.90e-05
	flat	-	-	78.4 ± 7.6	10.4	111.8 ± 13.8	1.35 ± 0.14	17	7.34	9.79e-01
Abell 1736	-	-	-	0.0	-	218.8 ± 6.3	0.62 ± 0.03	18	52.72	2.90e-05
	extr	15	0.10	150.4 ± 38.3	3.9	127.3 ± 37.9	0.99 ± 0.83	12	0.10	1.00e+00
	-	-	-	0.0	-	251.9 ± 19.2	0.20 ± 0.06	13	1.58	1.00e+00
	flat	-	-	150.4 ± 38.3	3.9	127.3 ± 37.9	0.99 ± 0.83	12	0.10	1.00e+00
Abell 1758	-	-	-	0.0	-	251.9 ± 19.2	0.20 ± 0.06	13	1.58	1.00e+00
	extr	20	0.40	116.8 ± 44.3	2.6	218.0 ± 58.6	1.03 ± 0.24	17	0.61	1.00e+00
	-	-	-	0.0	-	361.7 ± 20.8	0.62 ± 0.08	18	4.61	9.99e-01
	flat	-	-	230.8 ± 37.2	6.2	144.0 ± 50.2	1.21 ± 0.32	17	1.98	1.00e+00
Abell 1763	-	-	-	0.0	-	417.8 ± 20.2	0.36 ± 0.06	18	9.94	9.34e-01
	extr	39	0.60	214.7 ± 32.8	6.5	70.8 ± 29.1	1.37 ± 0.25	36	2.87	1.00e+00
	-	-	-	0.0	-	288.8 ± 13.8	0.60 ± 0.05	37	18.21	9.96e-01
	flat	-	-	214.7 ± 32.8	6.5	70.8 ± 29.1	1.37 ± 0.25	36	2.87	1.00e+00
Abell 1795	-	-	-	0.0	-	288.8 ± 13.8	0.60 ± 0.05	37	18.21	9.96e-01
	extr	53	0.30	18.4 ± 1.1	17.4	131.4 ± 2.8	1.17 ± 0.03	50	33.33	9.66e-01
	-	-	-	0.0	-	158.9 ± 2.0	0.86 ± 0.01	51	271.73	7.10e-32
	flat	-	-	19.0 ± 1.1	18.1	130.4 ± 2.8	1.18 ± 0.03	50	35.74	9.36e-01

Table 5—Continued

Cluster	Method	N_{bins}	r_{max} Mpc	K_0 keV cm ²	$\sigma_{K_0} > 0$	K_{100} keV cm ²	α	DOF	χ^2	p-value
(1)	(2)	(3)	(4)	(5)	(6)	(7)	(8)	(9)	(10)	(11)
Abell 1835	-	-	-	0.0	-	158.8 ± 2.0	0.86 ± 0.01	51	292.75	1.18e-35
	extr	16	0.30	10.9 ± 2.5	4.4	112.6 ± 7.9	1.25 ± 0.09	13	8.46	8.12e-01
	-	-	-	0.0	-	134.2 ± 5.2	0.99 ± 0.03	14	26.28	2.38e-02
	flat	-	-	11.4 ± 2.5	4.6	111.7 ± 7.9	1.26 ± 0.09	13	8.76	7.91e-01
Abell 1914	-	-	-	0.0	-	134.3 ± 5.3	0.98 ± 0.03	14	28.26	1.32e-02
	extr	29	0.40	63.3 ± 22.3	2.8	175.5 ± 32.3	0.88 ± 0.14	26	3.91	1.00e+00
	-	-	-	0.0	-	256.7 ± 10.4	0.61 ± 0.04	27	9.94	9.99e-01
	flat	-	-	107.2 ± 18.0	5.9	131.1 ± 28.3	1.05 ± 0.18	26	4.42	1.00e+00
Abell 1942	-	-	-	0.0	-	269.8 ± 10.3	0.52 ± 0.04	27	21.84	7.45e-01
	extr	12	0.22	107.7 ± 77.7	1.4	194.1 ± 88.7	0.66 ± 0.41	9	1.21	9.99e-01
	-	-	-	0.0	-	307.8 ± 17.3	0.35 ± 0.07	10	1.81	9.98e-01
	flat	-	-	107.7 ± 77.7	1.4	194.1 ± 88.7	0.66 ± 0.41	9	1.21	9.99e-01
Abell 1991	-	-	-	0.0	-	307.8 ± 17.3	0.35 ± 0.07	10	1.81	9.98e-01
	extr	19	0.10	1.0 ± 0.3	3.0	151.4 ± 4.1	1.04 ± 0.03	16	31.46	1.18e-02
	-	-	-	0.0	-	151.3 ± 3.6	1.04 ± 0.01	17	31.47	1.75e-02
	flat	-	-	1.5 ± 0.3	4.8	152.2 ± 4.2	1.09 ± 0.03	16	43.79	2.12e-04
Abell 1995	-	-	-	0.0	-	143.7 ± 3.4	0.99 ± 0.01	17	64.00	2.26e-07
	extr	26	0.60	374.3 ± 60.1	6.2	26.8 ± 32.9	2.08 ± 0.81	23	0.99	1.00e+00
	-	-	-	0.0	-	421.2 ± 36.4	0.35 ± 0.11	24	9.74	9.96e-01
	flat	-	-	374.3 ± 60.1	6.2	26.8 ± 32.9	2.08 ± 0.81	23	0.99	1.00e+00
Abell 2029	-	-	-	0.0	-	421.2 ± 36.4	0.35 ± 0.11	24	9.74	9.96e-01
	extr	58	0.40	6.1 ± 0.7	8.7	169.9 ± 2.1	0.92 ± 0.01	55	82.78	9.09e-03
	-	-	-	0.0	-	181.2 ± 1.6	0.82 ± 0.01	56	146.10	5.63e-10
	flat	-	-	10.5 ± 0.7	15.8	163.6 ± 2.1	0.95 ± 0.02	55	58.95	3.33e-01
Abell 2034	-	-	-	0.0	-	182.6 ± 1.6	0.78 ± 0.01	56	235.51	7.10e-24
	extr	67	0.50	215.8 ± 25.1	8.6	99.1 ± 25.3	1.05 ± 0.16	64	11.63	1.00e+00
	-	-	-	0.0	-	333.4 ± 9.0	0.42 ± 0.03	65	31.58	1.00e+00
	flat	-	-	232.6 ± 23.0	10.1	85.1 ± 22.6	1.14 ± 0.17	64	10.87	1.00e+00
Abell 2052	-	-	-	0.0	-	338.1 ± 8.9	0.41 ± 0.03	65	35.48	9.99e-01
	extr	29	0.10	8.9 ± 0.7	13.2	164.8 ± 2.6	1.23 ± 0.03	26	374.86	1.67e-63
	-	-	-	0.0	-	162.4 ± 2.3	0.99 ± 0.01	27	541.69	3.71e-97
	flat	-	-	9.5 ± 0.7	14.3	164.7 ± 2.6	1.25 ± 0.03	26	387.05	5.51e-66
Abell 2063	-	-	-	0.0	-	162.1 ± 2.3	0.99 ± 0.01	27	580.67	3.03e-105
	extr	52	0.18	53.5 ± 2.6	20.6	129.0 ± 3.9	1.07 ± 0.05	49	37.82	8.77e-01
	-	-	-	0.0	-	180.6 ± 2.4	0.51 ± 0.01	50	224.14	6.72e-24
	flat	-	-	53.5 ± 2.6	20.6	129.0 ± 3.9	1.07 ± 0.05	49	37.82	8.77e-01
Abell 2065	-	-	-	0.0	-	180.6 ± 2.4	0.51 ± 0.01	50	224.14	6.72e-24
	extr	29	0.20	33.1 ± 6.9	4.8	206.9 ± 10.8	0.97 ± 0.09	26	7.99	1.00e+00
	-	-	-	0.0	-	239.0 ± 7.5	0.67 ± 0.03	27	21.36	7.69e-01
	flat	-	-	43.9 ± 6.5	6.8	195.3 ± 10.6	1.02 ± 0.10	26	7.97	1.00e+00
Abell 2069	-	-	-	0.0	-	236.5 ± 7.5	0.60 ± 0.03	27	29.46	3.39e-01
	extr	39	0.40	416.2 ± 41.8	10.0	82.4 ± 46.0	1.22 ± 0.41	36	5.75	1.00e+00
	-	-	-	0.0	-	544.7 ± 16.4	0.20 ± 0.03	37	15.09	1.00e+00
	flat	-	-	453.2 ± 35.6	12.7	54.6 ± 36.3	1.47 ± 0.51	36	5.71	1.00e+00

Table 5—Continued

Cluster	Method	N_{bins}	r_{max} Mpc	K_0 keV cm ²	$\sigma_{K_0} > 0$	K_{100} keV cm ²	α	DOF	χ^2	p-value
(1)	(2)	(3)	(4)	(5)	(6)	(7)	(8)	(9)	(10)	(11)
Abell 2104	-	-	-	0.0	-	557.2 ± 16.2	0.17 ± 0.03	37	16.52	9.99e-01
	extr	9	0.12	98.0 ± 57.6	1.7	276.2 ± 59.7	0.94 ± 0.55	6	0.64	9.96e-01
	-	-	-	0.0	-	350.0 ± 36.1	0.46 ± 0.10	7	2.22	9.47e-01
Abell 2107	flat	-	-	160.6 ± 42.2	3.8	210.1 ± 53.9	1.20 ± 0.77	6	0.74	9.94e-01
	-	-	-	0.0	-	331.9 ± 33.4	0.30 ± 0.08	7	3.39	8.47e-01
	extr	6	0.03	18.0 ± 4.7	3.8	473.9 ± 117.3	1.03 ± 0.16	3	13.10	4.42e-03
Abell 2111	-	-	-	0.0	-	290.4 ± 26.6	0.64 ± 0.04	4	40.08	4.17e-08
	flat	-	-	21.2 ± 5.8	3.6	396.1 ± 92.5	0.91 ± 0.16	3	15.79	1.25e-03
	-	-	-	0.0	-	263.6 ± 21.3	0.55 ± 0.03	4	43.05	1.01e-08
Abell 2124	extr	22	0.40	107.4 ± 97.3	1.1	194.0 ± 118.7	0.65 ± 0.38	19	1.06	1.00e+00
	-	-	-	0.0	-	317.5 ± 23.7	0.39 ± 0.08	20	1.54	1.00e+00
	flat	-	-	107.4 ± 97.3	1.1	194.0 ± 118.7	0.65 ± 0.38	19	1.06	1.00e+00
Abell 2125	-	-	-	0.0	-	317.5 ± 23.7	0.39 ± 0.08	20	1.54	1.00e+00
	extr	19	0.12	88.7 ± 24.2	3.7	272.5 ± 30.8	0.89 ± 0.27	16	2.86	1.00e+00
	-	-	-	0.0	-	325.0 ± 21.8	0.41 ± 0.05	17	7.20	9.81e-01
Abell 2142	flat	-	-	98.3 ± 23.9	4.1	260.8 ± 30.8	0.90 ± 0.28	16	3.24	1.00e+00
	-	-	-	0.0	-	320.8 ± 21.3	0.37 ± 0.05	17	7.78	9.71e-01
	extr	10	0.20	225.2 ± 32.0	7.0	32.9 ± 41.2	1.35 ± 1.73	7	0.06	1.00e+00
Abell 2147	-	-	-	0.0	-	264.5 ± 11.5	0.10 ± 0.05	8	1.06	9.98e-01
	flat	-	-	225.2 ± 32.0	7.0	32.9 ± 41.2	1.35 ± 1.73	7	0.06	1.00e+00
	-	-	-	0.0	-	264.5 ± 11.5	0.10 ± 0.05	8	1.06	9.98e-01
Abell 2151	extr	75	0.30	58.5 ± 2.7	21.7	132.5 ± 4.5	1.13 ± 0.04	72	17.26	1.00e+00
	-	-	-	0.0	-	205.9 ± 2.1	0.62 ± 0.01	73	240.81	8.51e-20
	flat	-	-	68.1 ± 2.5	27.5	120.6 ± 4.4	1.22 ± 0.04	72	17.98	1.00e+00
Abell 2155	-	-	-	0.0	-	206.1 ± 2.2	0.58 ± 0.01	73	335.00	3.31e-35
	extr	57	0.20	151.9 ± 27.2	5.6	136.2 ± 30.5	0.55 ± 0.19	54	31.13	9.95e-01
	-	-	-	0.0	-	291.4 ± 6.4	0.18 ± 0.02	55	35.26	9.82e-01
Abell 2163	flat	-	-	151.9 ± 27.2	5.6	136.2 ± 30.5	0.55 ± 0.19	54	31.13	9.95e-01
	-	-	-	0.0	-	291.4 ± 6.4	0.18 ± 0.02	55	35.26	9.82e-01
	extr	20	0.07	1.7 ± 3.0	0.6	137.9 ± 6.0	0.61 ± 0.06	17	36.84	3.54e-03
Abell 2199	-	-	-	0.0	-	136.6 ± 5.2	0.58 ± 0.02	18	37.11	5.07e-03
	flat	-	-	0.4 ± 3.6	0.1	135.2 ± 5.4	0.56 ± 0.06	17	36.91	3.46e-03
	-	-	-	0.0	-	135.0 ± 5.0	0.55 ± 0.02	18	36.92	5.37e-03
Abell 2204	extr	42	0.60	437.3 ± 82.7	5.3	72.5 ± 50.8	1.86 ± 0.43	39	7.08	1.00e+00
	-	-	-	0.0	-	449.2 ± 42.9	0.82 ± 0.09	40	20.09	9.96e-01
	flat	-	-	438.0 ± 82.6	5.3	72.2 ± 50.6	1.87 ± 0.43	39	7.08	1.00e+00
Abell 2204	-	-	-	0.0	-	449.3 ± 42.9	0.82 ± 0.09	40	20.17	9.96e-01
	extr	7	0.02	7.6 ± 0.8	9.1	423.7 ± 95.3	1.38 ± 0.12	4	3.72	4.45e-01
	-	-	-	0.0	-	143.3 ± 11.8	0.72 ± 0.03	5	35.07	1.46e-06
Abell 2204	flat	-	-	13.3 ± 0.8	15.6	331.5 ± 90.0	1.35 ± 0.15	4	11.09	2.56e-02
	-	-	-	0.0	-	81.8 ± 5.2	0.44 ± 0.02	5	45.17	1.34e-08
	extr	15	0.20	9.7 ± 0.9	11.1	166.2 ± 6.0	1.41 ± 0.05	12	22.73	3.01e-02
Abell 2204	-	-	-	0.0	-	164.6 ± 5.9	1.02 ± 0.02	13	102.32	5.88e-16
	flat	-	-	9.7 ± 0.9	11.1	166.2 ± 6.0	1.41 ± 0.05	12	22.73	3.01e-02

Table 5—Continued

Cluster	Method	N_{bins}	r_{max} Mpc	K_0 keV cm ²	$\sigma_{K_0} > 0$	K_{100} keV cm ²	α	DOF	χ^2	p-value
(1)	(2)	(3)	(4)	(5)	(6)	(7)	(8)	(9)	(10)	(11)
Abell 2218	-	-	-	0.0	-	164.6 ± 5.9	1.02 ± 0.02	13	102.32	5.88e-16
	extr	42	0.60	288.6 ± 20.0	14.4	10.7 ± 7.1	2.35 ± 0.41	39	4.83	1.00e+00
	-	-	-	0.0	-	294.5 ± 14.7	0.41 ± 0.05	40	39.78	4.80e-01
	flat	-	-	288.6 ± 20.0	14.4	10.7 ± 7.1	2.35 ± 0.41	39	4.83	1.00e+00
Abell 2219	-	-	-	0.0	-	294.5 ± 14.7	0.41 ± 0.05	40	39.78	4.80e-01
	extr	34	0.60	411.6 ± 43.2	9.5	17.0 ± 19.2	1.97 ± 0.66	31	3.70	1.00e+00
	-	-	-	0.0	-	407.6 ± 26.4	0.36 ± 0.06	32	19.62	9.58e-01
	flat	-	-	411.6 ± 43.2	9.5	17.0 ± 19.2	1.97 ± 0.66	31	3.70	1.00e+00
Abell 2244	-	-	-	0.0	-	407.6 ± 26.4	0.36 ± 0.06	32	19.62	9.58e-01
	extr	34	0.30	57.6 ± 4.2	13.6	109.1 ± 6.0	1.00 ± 0.05	31	14.02	9.96e-01
	-	-	-	0.0	-	180.0 ± 2.1	0.56 ± 0.02	32	102.67	2.46e-09
	flat	-	-	57.6 ± 4.2	13.6	109.1 ± 6.0	1.00 ± 0.05	31	14.02	9.96e-01
Abell 2255	-	-	-	0.0	-	180.0 ± 2.1	0.56 ± 0.02	32	102.67	2.46e-09
	extr	40	0.30	529.1 ± 28.2	18.8	5.8 ± 16.6	2.63 ± 2.69	37	0.24	1.00e+00
	-	-	-	0.0	-	553.0 ± 14.0	0.05 ± 0.03	38	2.79	1.00e+00
	flat	-	-	529.1 ± 28.2	18.8	5.8 ± 16.6	2.63 ± 2.69	37	0.24	1.00e+00
Abell 2256	-	-	-	0.0	-	553.0 ± 14.0	0.05 ± 0.03	38	2.79	1.00e+00
	extr	63	0.35	349.6 ± 11.6	30.2	7.0 ± 7.6	2.54 ± 0.93	60	2.24	1.00e+00
	-	-	-	0.0	-	378.4 ± 6.9	0.08 ± 0.02	61	21.60	1.00e+00
	flat	-	-	349.6 ± 11.6	30.2	7.0 ± 7.6	2.54 ± 0.93	60	2.24	1.00e+00
Abell 2259	-	-	-	0.0	-	378.4 ± 6.9	0.08 ± 0.02	61	21.60	1.00e+00
	extr	36	0.50	114.0 ± 18.9	6.0	61.0 ± 20.4	1.36 ± 0.24	33	1.37	1.00e+00
	-	-	-	0.0	-	189.0 ± 8.7	0.63 ± 0.05	34	15.77	9.97e-01
	flat	-	-	114.0 ± 18.9	6.0	61.0 ± 20.4	1.36 ± 0.24	33	1.37	1.00e+00
Abell 2261	-	-	-	0.0	-	189.0 ± 8.7	0.63 ± 0.05	34	15.77	9.97e-01
	extr	18	0.30	60.5 ± 8.2	7.4	106.5 ± 14.1	1.27 ± 0.16	15	3.63	9.99e-01
	-	-	-	0.0	-	189.6 ± 6.6	0.61 ± 0.04	16	28.62	2.67e-02
	flat	-	-	61.1 ± 8.1	7.5	106.0 ± 14.1	1.27 ± 0.16	15	3.62	9.99e-01
Abell 2294	-	-	-	0.0	-	189.7 ± 6.6	0.61 ± 0.04	16	29.00	2.40e-02
	extr	22	0.32	128.5 ± 52.0	2.5	246.7 ± 75.6	1.04 ± 0.32	19	0.60	1.00e+00
	-	-	-	0.0	-	409.8 ± 28.7	0.57 ± 0.09	20	3.67	1.00e+00
	flat	-	-	156.3 ± 52.7	3.0	235.7 ± 76.3	1.03 ± 0.33	19	0.83	1.00e+00
Abell 2319	-	-	-	0.0	-	428.8 ± 28.6	0.49 ± 0.08	20	4.23	1.00e+00
	extr	74	0.40	270.2 ± 4.8	56.0	39.4 ± 7.1	1.76 ± 0.15	71	9.83	1.00e+00
	-	-	-	0.0	-	363.1 ± 4.3	0.19 ± 0.01	72	212.75	7.89e-16
	flat	-	-	270.2 ± 4.8	56.0	39.4 ± 7.1	1.76 ± 0.15	71	9.83	1.00e+00
Abell 2384	-	-	-	0.0	-	363.1 ± 4.3	0.19 ± 0.01	72	212.75	7.89e-16
	extr	23	0.20	17.9 ± 3.3	5.4	162.9 ± 7.3	1.31 ± 0.09	20	7.54	9.95e-01
	-	-	-	0.0	-	179.6 ± 6.3	0.99 ± 0.04	21	29.61	1.00e-01
	flat	-	-	38.5 ± 3.0	13.0	139.2 ± 7.3	1.49 ± 0.11	20	7.85	9.93e-01
Abell 2390	-	-	-	0.0	-	163.6 ± 6.1	0.70 ± 0.03	21	87.32	4.67e-10
	extr	11	0.20	14.7 ± 7.0	2.1	202.9 ± 15.6	1.07 ± 0.15	8	0.96	9.99e-01
	-	-	-	0.0	-	214.4 ± 13.9	0.84 ± 0.05	9	4.71	8.59e-01
	flat	-	-	14.7 ± 7.0	2.1	202.9 ± 15.6	1.07 ± 0.15	8	0.96	9.99e-01

Table 5—Continued

Cluster	Method	N_{bins}	r_{max} Mpc	K_0 keV cm ²	$\sigma_{K_0} > 0$	K_{100} keV cm ²	α	DOF	χ^2	p-value
(1)	(2)	(3)	(4)	(5)	(6)	(7)	(8)	(9)	(10)	(11)
Abell 2409	-	-	-	0.0	-	214.4 ± 13.9	0.84 ± 0.05	9	4.71	8.59e-01
	extr	16	0.20	69.6 ± 20.9	3.3	124.1 ± 27.4	0.96 ± 0.32	13	8.79	7.88e-01
	-	-	-	0.0	-	198.6 ± 10.2	0.45 ± 0.06	14	15.23	3.62e-01
	flat	-	-	73.8 ± 20.7	3.6	120.8 ± 27.3	0.97 ± 0.33	13	9.06	7.68e-01
Abell 2420	-	-	-	0.0	-	199.4 ± 10.3	0.43 ± 0.06	14	15.83	3.24e-01
	extr	64	0.50	332.6 ± 67.5	4.9	64.3 ± 62.6	1.12 ± 0.58	61	5.54	1.00e+00
	-	-	-	0.0	-	411.0 ± 22.4	0.28 ± 0.06	62	9.20	1.00e+00
	flat	-	-	332.6 ± 67.5	4.9	64.3 ± 62.6	1.12 ± 0.58	61	5.54	1.00e+00
Abell 2462	-	-	-	0.0	-	411.0 ± 22.4	0.28 ± 0.06	62	9.20	1.00e+00
	extr	58	0.40	129.7 ± 27.0	4.8	83.2 ± 31.1	0.77 ± 0.24	55	1.23	1.00e+00
	-	-	-	0.0	-	224.1 ± 6.2	0.30 ± 0.03	56	7.73	1.00e+00
	flat	-	-	129.7 ± 27.0	4.8	83.2 ± 31.1	0.77 ± 0.24	55	1.23	1.00e+00
Abell 2537	-	-	-	0.0	-	224.1 ± 6.2	0.30 ± 0.03	56	7.73	1.00e+00
	extr	14	0.30	106.7 ± 19.6	5.4	127.9 ± 29.2	1.24 ± 0.26	11	1.05	1.00e+00
	-	-	-	0.0	-	259.9 ± 11.9	0.51 ± 0.06	12	12.70	3.91e-01
	flat	-	-	110.4 ± 19.4	5.7	124.7 ± 29.0	1.26 ± 0.27	11	1.05	1.00e+00
Abell 2554	-	-	-	0.0	-	261.0 ± 11.9	0.50 ± 0.06	12	13.23	3.52e-01
	extr	30	0.30	105.1 ± 71.8	1.5	318.4 ± 86.2	0.66 ± 0.21	27	0.87	1.00e+00
	-	-	-	0.0	-	436.9 ± 18.7	0.45 ± 0.05	28	1.98	1.00e+00
	flat	-	-	105.1 ± 71.8	1.5	318.4 ± 86.2	0.66 ± 0.21	27	0.87	1.00e+00
Abell 2556	-	-	-	0.0	-	436.9 ± 18.7	0.45 ± 0.05	28	1.98	1.00e+00
	extr	17	0.13	10.6 ± 1.4	7.7	117.5 ± 3.9	1.10 ± 0.06	14	4.27	9.94e-01
	-	-	-	0.0	-	116.2 ± 3.5	0.76 ± 0.02	15	44.30	9.85e-05
	flat	-	-	12.4 ± 1.3	9.2	115.8 ± 4.0	1.13 ± 0.07	14	4.50	9.92e-01
Abell 2589	-	-	-	0.0	-	113.8 ± 3.4	0.72 ± 0.02	15	57.13	7.81e-07
	extr	25	0.10	52.0 ± 39.2	1.3	109.6 ± 34.8	0.61 ± 0.51	22	1.06	1.00e+00
	-	-	-	0.0	-	154.1 ± 13.4	0.29 ± 0.07	23	1.60	1.00e+00
	flat	-	-	52.0 ± 39.2	1.3	109.6 ± 34.8	0.61 ± 0.51	22	1.06	1.00e+00
Abell 2597	-	-	-	0.0	-	154.1 ± 13.4	0.29 ± 0.07	23	1.60	1.00e+00
	extr	8	0.06	9.6 ± 1.6	5.9	96.1 ± 14.0	1.19 ± 0.18	5	4.09	5.37e-01
	-	-	-	0.0	-	70.7 ± 5.0	0.62 ± 0.04	6	23.75	5.81e-04
	flat	-	-	10.6 ± 1.5	7.0	98.9 ± 15.2	1.26 ± 0.19	5	4.10	5.35e-01
Abell 2626	-	-	-	0.0	-	68.5 ± 4.8	0.59 ± 0.04	6	28.70	6.94e-05
	extr	22	0.12	23.2 ± 2.9	8.1	144.1 ± 6.3	1.05 ± 0.09	19	11.88	8.91e-01
	-	-	-	0.0	-	147.7 ± 5.2	0.62 ± 0.03	20	46.28	7.38e-04
	flat	-	-	23.2 ± 2.9	8.1	144.1 ± 6.3	1.05 ± 0.09	19	11.88	8.91e-01
Abell 2631	-	-	-	0.0	-	147.7 ± 5.2	0.62 ± 0.03	20	46.28	7.38e-04
	extr	38	0.80	308.8 ± 37.4	8.3	29.2 ± 23.4	1.44 ± 0.41	35	0.21	1.00e+00
	-	-	-	0.0	-	347.2 ± 21.7	0.33 ± 0.05	36	13.73	1.00e+00
	flat	-	-	308.8 ± 37.4	8.3	29.2 ± 23.4	1.44 ± 0.41	35	0.21	1.00e+00
Abell 2657	-	-	-	0.0	-	347.2 ± 21.7	0.33 ± 0.05	36	13.73	1.00e+00
	extr	51	0.20	65.4 ± 12.0	5.5	153.5 ± 15.1	0.91 ± 0.13	48	7.69	1.00e+00
	-	-	-	0.0	-	222.0 ± 5.9	0.50 ± 0.03	49	21.73	1.00e+00
	flat	-	-	65.4 ± 12.0	5.5	153.5 ± 15.1	0.91 ± 0.13	48	7.69	1.00e+00

Table 5—Continued

Cluster	Method	N_{bins}	r_{max} Mpc	K_0 keV cm ²	$\sigma_{K_0} > 0$	K_{100} keV cm ²	α	DOF	χ^2	p-value
(1)	(2)	(3)	(4)	(5)	(6)	(7)	(8)	(9)	(10)	(11)
Abell 2667	-	-	-	0.0	-	222.0 ± 5.9	0.50 ± 0.03	49	21.73	1.00e+00
	extr	11	0.20	12.3 ± 4.0	3.1	102.2 ± 7.7	1.17 ± 0.15	8	1.61	9.91e-01
	-	-	-	0.0	-	113.7 ± 6.2	0.85 ± 0.05	9	9.48	3.94e-01
	flat	-	-	19.3 ± 3.4	5.7	93.4 ± 7.6	1.31 ± 0.17	8	1.66	9.90e-01
Abell 2717	-	-	-	0.0	-	110.5 ± 6.2	0.75 ± 0.05	9	20.81	1.35e-02
	extr	26	0.12	26.3 ± 8.2	3.2	152.2 ± 10.1	0.76 ± 0.13	23	2.19	1.00e+00
	-	-	-	0.0	-	167.6 ± 7.9	0.50 ± 0.03	24	7.90	9.99e-01
	flat	-	-	27.0 ± 8.4	3.2	151.2 ± 10.2	0.75 ± 0.13	23	2.15	1.00e+00
Abell 2744	-	-	-	0.0	-	167.2 ± 7.8	0.49 ± 0.03	24	7.77	9.99e-01
	extr	27	0.60	295.1 ± 113.4	2.6	152.8 ± 112.7	0.83 ± 0.37	24	8.72	9.98e-01
	-	-	-	0.0	-	460.3 ± 29.9	0.37 ± 0.05	25	10.50	9.95e-01
	flat	-	-	438.4 ± 58.7	7.5	46.4 ± 44.0	1.41 ± 0.55	24	7.87	9.99e-01
Abell 2813	-	-	-	0.0	-	503.6 ± 29.3	0.30 ± 0.05	25	14.15	9.59e-01
	extr	14	0.30	216.3 ± 48.9	4.4	126.0 ± 74.9	1.52 ± 0.64	11	2.29	9.97e-01
	-	-	-	0.0	-	397.4 ± 33.0	0.42 ± 0.10	12	7.83	7.98e-01
	flat	-	-	267.6 ± 43.8	6.1	90.4 ± 67.3	1.76 ± 0.80	11	2.64	9.95e-01
Abell 3084	-	-	-	0.0	-	417.0 ± 33.5	0.31 ± 0.09	12	8.95	7.07e-01
	extr	34	0.30	96.7 ± 13.4	7.2	193.7 ± 22.8	1.08 ± 0.17	31	4.48	1.00e+00
	-	-	-	0.0	-	288.3 ± 14.4	0.43 ± 0.04	32	17.29	9.84e-01
	flat	-	-	96.7 ± 13.4	7.2	193.7 ± 22.8	1.08 ± 0.17	31	4.48	1.00e+00
Abell 3088	-	-	-	0.0	-	288.3 ± 14.4	0.43 ± 0.04	32	17.29	9.84e-01
	extr	10	0.20	32.7 ± 9.5	3.4	269.7 ± 25.8	1.51 ± 0.20	7	0.21	1.00e+00
	-	-	-	0.0	-	283.9 ± 23.8	1.02 ± 0.09	8	7.68	4.65e-01
	flat	-	-	82.8 ± 8.4	9.8	216.8 ± 25.8	1.71 ± 0.25	7	0.59	9.99e-01
Abell 3112	-	-	-	0.0	-	230.3 ± 18.8	0.49 ± 0.06	8	18.94	1.52e-02
	extr	18	0.12	8.2 ± 1.6	5.3	170.1 ± 6.8	1.09 ± 0.06	15	3.55	9.99e-01
	-	-	-	0.0	-	162.7 ± 6.0	0.86 ± 0.03	16	23.03	1.13e-01
	flat	-	-	11.4 ± 1.4	8.0	169.1 ± 7.0	1.17 ± 0.07	15	5.32	9.89e-01
Abell 3120	-	-	-	0.0	-	157.3 ± 5.8	0.82 ± 0.03	16	45.16	1.31e-04
	extr	29	0.20	15.0 ± 3.3	4.5	209.1 ± 10.9	1.02 ± 0.08	26	6.41	1.00e+00
	-	-	-	0.0	-	206.6 ± 10.1	0.76 ± 0.03	27	20.49	8.10e-01
	flat	-	-	17.3 ± 3.5	4.9	206.2 ± 10.9	0.99 ± 0.08	26	7.14	1.00e+00
Abell 3158	-	-	-	0.0	-	202.9 ± 9.8	0.70 ± 0.03	27	22.57	7.08e-01
	extr	72	0.40	166.0 ± 11.7	14.1	80.9 ± 12.9	0.90 ± 0.10	69	22.54	1.00e+00
	-	-	-	0.0	-	260.6 ± 2.9	0.32 ± 0.01	70	71.32	4.34e-01
	flat	-	-	166.0 ± 11.7	14.1	80.9 ± 12.9	0.90 ± 0.10	69	22.54	1.00e+00
Abell 3266	-	-	-	0.0	-	260.6 ± 2.9	0.32 ± 0.01	70	71.32	4.34e-01
	extr	15	0.08	63.7 ± 41.9	1.5	405.3 ± 51.6	0.71 ± 0.27	12	0.79	1.00e+00
	-	-	-	0.0	-	418.9 ± 37.8	0.44 ± 0.06	13	2.02	1.00e+00
	flat	-	-	72.5 ± 49.7	1.5	376.7 ± 48.0	0.64 ± 0.28	12	1.26	1.00e+00
Abell 3364	-	-	-	0.0	-	404.6 ± 35.2	0.39 ± 0.05	13	2.34	1.00e+00
	extr	55	0.70	268.6 ± 33.2	8.1	34.5 ± 18.0	1.97 ± 0.32	52	3.99	1.00e+00
	-	-	-	0.0	-	298.6 ± 22.7	0.63 ± 0.08	53	30.04	9.95e-01
	flat	-	-	268.6 ± 33.2	8.1	34.5 ± 18.0	1.97 ± 0.32	52	3.99	1.00e+00

Table 5—Continued

Cluster	Method	N_{bins}	r_{max} Mpc	K_0 keV cm ²	$\sigma_{K_0} > 0$	K_{100} keV cm ²	α	DOF	χ^2	p-value
(1)	(2)	(3)	(4)	(5)	(6)	(7)	(8)	(9)	(10)	(11)
Abell 3376	-	-	-	0.0	-	298.6 \pm 22.7	0.63 \pm 0.08	53	30.04	9.95e-01
	extr	67	0.30	282.9 \pm 9.3	30.3	59.0 \pm 10.6	1.71 \pm 0.18	64	5.46	1.00e+00
	-	-	-	0.0	-	378.5 \pm 4.3	0.30 \pm 0.02	65	112.42	2.39e-04
	flat	-	-	282.9 \pm 9.3	30.3	59.0 \pm 10.6	1.71 \pm 0.18	64	5.46	1.00e+00
Abell 3391	-	-	-	0.0	-	378.5 \pm 4.3	0.30 \pm 0.02	65	112.42	2.39e-04
	extr	75	0.40	367.5 \pm 16.0	22.9	23.6 \pm 14.8	1.64 \pm 0.47	72	3.59	1.00e+00
	-	-	-	0.0	-	420.4 \pm 7.5	0.14 \pm 0.02	73	24.89	1.00e+00
	flat	-	-	367.5 \pm 16.0	22.9	23.6 \pm 14.8	1.64 \pm 0.47	72	3.59	1.00e+00
Abell 3395	-	-	-	0.0	-	420.4 \pm 7.5	0.14 \pm 0.02	73	24.89	1.00e+00
	extr	24	0.12	213.3 \pm 26.2	8.2	133.5 \pm 30.4	1.58 \pm 0.79	21	0.00	1.00e+00
	-	-	-	0.0	-	325.5 \pm 14.4	0.23 \pm 0.05	22	5.73	1.00e+00
	flat	-	-	247.2 \pm 25.2	9.8	105.9 \pm 29.8	1.65 \pm 1.01	21	0.01	1.00e+00
Abell 3528S	-	-	-	0.0	-	332.8 \pm 14.0	0.16 \pm 0.05	22	4.49	1.00e+00
	extr	24	0.12	19.4 \pm 2.3	8.6	288.1 \pm 10.2	1.16 \pm 0.05	21	32.09	5.73e-02
	-	-	-	0.0	-	271.7 \pm 8.8	0.84 \pm 0.02	22	84.38	3.04e-09
	flat	-	-	31.6 \pm 2.3	14.0	270.0 \pm 10.3	1.17 \pm 0.06	21	32.23	5.55e-02
Abell 3558	-	-	-	0.0	-	239.2 \pm 7.6	0.65 \pm 0.02	22	128.53	4.82e-17
	extr	25	0.12	126.2 \pm 11.8	10.7	132.5 \pm 17.2	2.11 \pm 0.58	22	6.87	9.99e-01
	-	-	-	0.0	-	234.0 \pm 10.7	0.42 \pm 0.06	23	19.89	6.49e-01
	flat	-	-	126.2 \pm 11.8	10.7	132.5 \pm 17.2	2.11 \pm 0.58	22	6.87	9.99e-01
Abell 3562	-	-	-	0.0	-	234.0 \pm 10.7	0.42 \pm 0.06	23	19.89	6.49e-01
	extr	26	0.12	71.4 \pm 9.0	8.0	166.8 \pm 10.4	0.80 \pm 0.13	23	33.16	7.84e-02
	-	-	-	0.0	-	217.3 \pm 6.5	0.33 \pm 0.02	24	54.22	3.99e-04
	flat	-	-	77.4 \pm 8.9	8.7	159.8 \pm 10.4	0.81 \pm 0.13	23	35.16	5.01e-02
Abell 3571	-	-	-	0.0	-	215.4 \pm 6.4	0.31 \pm 0.02	24	56.31	2.08e-04
	extr	31	0.12	79.3 \pm 14.8	5.4	191.3 \pm 14.8	0.82 \pm 0.16	28	375.69	1.65e-62
	-	-	-	0.0	-	256.1 \pm 7.9	0.39 \pm 0.03	29	657.82	6.19e-120
	flat	-	-	79.3 \pm 14.8	5.4	191.3 \pm 14.8	0.82 \pm 0.16	28	375.69	1.65e-62
Abell 3581	-	-	-	0.0	-	256.1 \pm 7.9	0.39 \pm 0.03	29	657.82	6.19e-120
	extr	46	0.10	7.1 \pm 0.8	8.4	138.1 \pm 5.5	1.15 \pm 0.05	43	20.49	9.99e-01
	-	-	-	0.0	-	121.6 \pm 4.0	0.85 \pm 0.02	44	65.85	1.80e-02
	flat	-	-	9.5 \pm 0.8	12.2	138.1 \pm 5.7	1.22 \pm 0.05	43	21.56	9.97e-01
Abell 3667	-	-	-	0.0	-	114.3 \pm 3.8	0.79 \pm 0.02	44	103.30	1.13e-06
	extr	56	0.30	149.3 \pm 17.2	8.7	121.9 \pm 18.6	0.72 \pm 0.09	53	21.14	1.00e+00
	-	-	-	0.0	-	278.7 \pm 2.3	0.34 \pm 0.01	54	44.43	8.20e-01
	flat	-	-	160.4 \pm 15.5	10.4	110.6 \pm 16.8	0.78 \pm 0.10	53	22.84	1.00e+00
Abell 3822	-	-	-	0.0	-	279.5 \pm 2.3	0.33 \pm 0.01	54	52.83	5.19e-01
	extr	42	0.30	108.7 \pm 76.4	1.4	200.3 \pm 90.8	0.66 \pm 0.33	39	3.24	1.00e+00
	-	-	-	0.0	-	322.5 \pm 16.6	0.38 \pm 0.07	40	3.95	1.00e+00
	flat	-	-	108.7 \pm 76.4	1.4	200.3 \pm 90.8	0.66 \pm 0.33	39	3.24	1.00e+00
Abell 3827	-	-	-	0.0	-	322.5 \pm 16.6	0.38 \pm 0.07	40	3.95	1.00e+00
	extr	67	0.60	144.6 \pm 13.4	10.8	113.1 \pm 15.2	1.23 \pm 0.10	64	1651.91	6.60e-303
	-	-	-	0.0	-	287.2 \pm 7.4	0.60 \pm 0.03	65	4867.53	0.00e+00
	flat	-	-	164.6 \pm 12.5	13.2	94.8 \pm 13.7	1.34 \pm 0.10	64	1368.56	6.59e-244

Table 5—Continued

Cluster	Method	N_{bins}	r_{max} Mpc	K_0 keV cm ²	$\sigma_{K_0} > 0$	K_{100} keV cm ²	α	DOF	χ^2	p-value
(1)	(2)	(3)	(4)	(5)	(6)	(7)	(8)	(9)	(10)	(11)
Abell 3921	-	-	-	0.0	-	293.5 ± 7.3	0.57 ± 0.03	65	5896.48	0.00e+00
	extr	47	0.40	101.2 ± 17.9	5.7	151.5 ± 23.0	0.86 ± 0.11	44	7.55	1.00e+00
	-	-	-	0.0	-	272.4 ± 6.8	0.48 ± 0.03	45	22.08	9.98e-01
	flat	-	-	101.2 ± 17.9	5.7	151.5 ± 23.0	0.86 ± 0.11	44	7.55	1.00e+00
Abell 4038	-	-	-	0.0	-	272.4 ± 6.8	0.48 ± 0.03	45	22.08	9.98e-01
	extr	42	0.12	37.1 ± 1.2	30.2	118.5 ± 2.7	1.10 ± 0.05	39	58.69	2.22e-02
	-	-	-	0.0	-	127.3 ± 2.0	0.42 ± 0.01	40	393.69	1.15e-59
	flat	-	-	37.9 ± 1.2	31.2	117.9 ± 2.7	1.11 ± 0.05	39	60.31	1.58e-02
Abell 4059	-	-	-	0.0	-	126.5 ± 1.9	0.41 ± 0.01	40	410.34	6.07e-63
	extr	33	0.15	0.0 ± 1.0	0.0	210.7 ± 2.2	0.82 ± 0.01	30	44.86	3.98e-02
	-	-	-	0.0	-	210.7 ± 2.2	0.82 ± 0.01	31	44.86	5.13e-02
	flat	-	-	7.1 ± 1.0	6.7	203.2 ± 2.4	0.88 ± 0.02	30	54.25	4.31e-03
Abell S0405	-	-	-	0.0	-	208.3 ± 2.2	0.77 ± 0.01	31	93.59	3.35e-08
	extr	34	0.20	23.5 ± 21.0	1.1	261.1 ± 22.1	0.52 ± 0.10	31	8.24	1.00e+00
	-	-	-	0.0	-	281.9 ± 11.3	0.43 ± 0.03	32	9.16	1.00e+00
	flat	-	-	16.9 ± 27.9	0.6	274.2 ± 27.3	0.45 ± 0.10	31	9.79	1.00e+00
Abell S0592	-	-	-	0.0	-	289.3 ± 11.2	0.40 ± 0.02	32	10.10	1.00e+00
	extr	23	0.40	52.2 ± 14.4	3.6	199.0 ± 23.6	0.99 ± 0.12	20	9.34	9.79e-01
	-	-	-	0.0	-	271.1 ± 10.0	0.68 ± 0.04	21	16.08	7.65e-01
	flat	-	-	58.7 ± 14.4	4.1	195.5 ± 23.6	0.99 ± 0.13	20	9.70	9.73e-01
AC 114	-	-	-	0.0	-	275.6 ± 10.0	0.65 ± 0.04	21	17.46	6.83e-01
	flat	20	0.45	199.8 ± 28.0	7.1	70.0 ± 32.6	1.50 ± 0.36	17	3.69	1.00e+00
	-	-	-	0.0	-	306.6 ± 14.8	0.46 ± 0.06	18	16.94	5.28e-01
	extr	-	-	199.8 ± 28.0	7.1	70.0 ± 32.6	1.50 ± 0.36	17	3.69	1.00e+00
AWM7	-	-	-	0.0	-	306.6 ± 14.8	0.46 ± 0.06	18	16.94	5.28e-01
	extr	13	0.02	4.8 ± 1.1	4.5	290.2 ± 28.4	0.89 ± 0.06	10	7.30	6.96e-01
	-	-	-	0.0	-	217.6 ± 10.6	0.70 ± 0.02	11	20.91	3.43e-02
	flat	-	-	8.4 ± 1.3	6.5	227.6 ± 23.1	0.80 ± 0.06	10	13.19	2.13e-01
Centaurus	-	-	-	0.0	-	157.1 ± 6.6	0.54 ± 0.01	11	32.84	5.58e-04
	extr	27	0.03	1.4 ± 0.04	32.1	421.2 ± 5.4	1.25 ± 0.01	24	253.13	3.95e-40
	-	-	-	0.0	-	328.8 ± 3.1	1.11 ± 0.00	25	1159.86	6.17e-229
	flat	-	-	2.2 ± 0.04	56.6	474.9 ± 6.3	1.33 ± 0.01	24	483.38	4.67e-87
CID 72	-	-	-	0.0	-	307.3 ± 2.9	1.08 ± 0.00	25	3151.59	0.00e+00
	extr	37	0.12	4.9 ± 0.3	14.6	139.2 ± 2.1	0.95 ± 0.02	34	135.51	4.60e-14
	-	-	-	0.0	-	128.6 ± 1.7	0.77 ± 0.01	35	313.61	1.74e-46
	flat	-	-	9.4 ± 0.3	29.9	133.2 ± 2.2	0.99 ± 0.02	34	129.24	5.04e-13
CL J1226.9+3332	-	-	-	0.0	-	111.3 ± 1.5	0.63 ± 0.01	35	634.02	4.82e-111
	extr	10	0.40	166.0 ± 45.2	3.7	99.0 ± 58.7	1.41 ± 0.50	7	0.75	9.98e-01
	-	-	-	0.0	-	308.7 ± 25.3	0.55 ± 0.10	8	4.81	7.78e-01
	flat	-	-	166.0 ± 45.2	3.7	99.0 ± 58.7	1.41 ± 0.50	7	0.75	9.98e-01
Cygnus A	-	-	-	0.0	-	308.7 ± 25.3	0.55 ± 0.10	8	4.81	7.78e-01
	extr	19	0.10	21.7 ± 0.9	24.2	208.4 ± 6.7	1.51 ± 0.05	16	28.49	2.76e-02
	-	-	-	0.0	-	154.4 ± 3.7	0.73 ± 0.02	17	294.72	1.38e-52
	flat	-	-	23.6 ± 0.9	27.1	210.1 ± 6.9	1.57 ± 0.05	16	22.48	1.28e-01

Table 5—Continued

Cluster	Method	N_{bins}	r_{max} Mpc	K_0 keV cm ²	$\sigma_{K_0} > 0$	K_{100} keV cm ²	α	DOF	χ^2	p-value
(1)	(2)	(3)	(4)	(5)	(6)	(7)	(8)	(9)	(10)	(11)
ESO 3060170	-	-	-	0.0	-	148.5 ± 3.6	0.70 ± 0.02	17	340.49	4.67e-62
	extr	5	0.02	7.8 ± 1.0	7.8	1370.5 ± 562.2	1.79 ± 0.20	2	0.77	6.80e-01
	-	-	-	0.0	-	255.8 ± 37.1	0.90 ± 0.05	3	25.78	1.06e-05
	flat	-	-	8.0 ± 1.0	8.0	1400.9 ± 578.9	1.80 ± 0.21	2	0.81	6.67e-01
ESO 5520200	-	-	-	0.0	-	251.2 ± 36.3	0.89 ± 0.05	3	26.70	6.81e-06
	extr	17	0.10	6.3 ± 3.5	1.8	113.8 ± 7.0	0.74 ± 0.10	31	0.15	1.00e+00
	-	-	-	0.0	-	112.0 ± 6.0	0.60 ± 0.03	32	5.57	1.00e+00
	flat	-	-	5.9 ± 4.2	1.4	121.8 ± 6.5	0.67 ± 0.09	31	0.52	1.00e+00
EXO 422-086	-	-	-	0.0	-	121.1 ± 5.8	0.57 ± 0.03	32	4.15	1.00e+00
	extr	19	0.07	10.1 ± 0.8	12.5	199.3 ± 11.4	1.21 ± 0.06	16	11.00	8.10e-01
	-	-	-	0.0	-	142.0 ± 5.6	0.75 ± 0.02	17	112.48	4.11e-16
	flat	-	-	13.8 ± 0.8	17.5	193.8 ± 11.8	1.25 ± 0.06	16	11.24	7.95e-01
HCG 62	-	-	-	0.0	-	120.4 ± 4.6	0.62 ± 0.02	17	157.52	8.19e-25
	extr	27	0.04	3.1 ± 0.08	40.8	203.9 ± 10.4	1.23 ± 0.02	24	153.17	8.52e-21
	-	-	-	0.0	-	63.4 ± 1.7	0.63 ± 0.01	25	660.63	2.48e-123
	flat	-	-	3.4 ± 0.07	47.4	219.0 ± 11.4	1.28 ± 0.03	24	138.50	4.39e-18
HCG 42	-	-	-	0.0	-	57.7 ± 1.5	0.60 ± 0.01	25	751.59	1.92e-142
	extr	22	0.03	1.8 ± 0.3	5.5	128.5 ± 12.8	0.88 ± 0.05	19	44.38	8.38e-04
	-	-	-	0.0	-	89.4 ± 4.1	0.67 ± 0.01	20	60.87	5.23e-06
	flat	-	-	1.9 ± 0.3	5.7	126.5 ± 12.6	0.87 ± 0.05	19	45.28	6.25e-04
Hercules A	-	-	-	0.0	-	87.4 ± 4.0	0.66 ± 0.01	20	62.24	3.19e-06
	extr	16	0.20	2.8 ± 1.5	1.8	151.8 ± 3.3	0.99 ± 0.04	13	2.34	1.00e+00
	-	-	-	0.0	-	154.1 ± 3.1	0.94 ± 0.02	14	6.23	9.60e-01
	flat	-	-	9.2 ± 1.3	6.8	143.9 ± 3.3	1.07 ± 0.04	13	6.24	9.37e-01
Hydra A	-	-	-	0.0	-	151.0 ± 3.1	0.87 ± 0.02	14	46.89	2.01e-05
	extr	57	0.30	13.0 ± 0.7	19.5	115.3 ± 1.4	1.02 ± 0.02	54	71.44	5.62e-02
	-	-	-	0.0	-	134.0 ± 1.0	0.81 ± 0.01	55	364.39	3.36e-47
	flat	-	-	13.3 ± 0.7	20.0	114.9 ± 1.4	1.03 ± 0.02	54	72.66	4.60e-02
M49	-	-	-	0.0	-	134.0 ± 1.0	0.80 ± 0.01	55	379.86	4.40e-50
	extr	54	1.00	0.9 ± 0.05	18.1	486.7 ± 32.2	1.14 ± 0.02	51	74.03	1.92e-02
	-	-	-	0.0	-	231.3 ± 10.1	0.89 ± 0.01	52	327.07	1.58e-41
	flat	-	-	0.9 ± 0.05	18.9	495.3 ± 32.9	1.14 ± 0.02	51	75.65	1.41e-02
M87	-	-	-	0.0	-	227.4 ± 10.0	0.88 ± 0.01	52	349.43	1.14e-45
	extr	88	0.04	3.5 ± 0.08	43.1	146.4 ± 1.0	0.80 ± 0.00	85	749.92	4.94e-107
	-	-	-	0.0	-	123.8 ± 0.5	0.64 ± 0.00	86	2083.55	0.00e+00
	flat	-	-	3.5 ± 0.08	43.7	146.6 ± 1.0	0.80 ± 0.00	85	763.71	1.06e-109
MACS J0011.7-1523	-	-	-	0.0	-	123.7 ± 0.5	0.64 ± 0.00	86	2130.02	0.00e+00
	extr	16	0.40	14.9 ± 6.4	2.3	111.3 ± 11.6	1.03 ± 0.10	13	1.95	1.00e+00
	-	-	-	0.0	-	134.7 ± 5.1	0.86 ± 0.04	14	5.88	9.70e-01
	flat	-	-	18.8 ± 6.3	3.0	109.1 ± 11.5	1.04 ± 0.10	13	2.28	1.00e+00
MACS J0035.4-2015	-	-	-	0.0	-	138.4 ± 5.0	0.81 ± 0.04	14	7.99	8.90e-01
	extr	29	0.70	69.5 ± 17.1	4.1	93.9 ± 23.0	1.15 ± 0.16	26	0.70	1.00e+00
	-	-	-	0.0	-	183.2 ± 11.5	0.74 ± 0.06	27	11.72	9.95e-01
	flat	-	-	93.4 ± 15.7	6.0	76.4 ± 20.8	1.26 ± 0.17	26	1.00	1.00e+00

Table 5—Continued

Cluster	Method	N_{bins}	r_{max} Mpc	K_0 keV cm ²	$\sigma_{K_0} > 0$	K_{100} keV cm ²	α	DOF	χ^2	p-value
(1)	(2)	(3)	(4)	(5)	(6)	(7)	(8)	(9)	(10)	(11)
MACS J0159.8-0849	-	-	-	0.0	-	198.2 ± 11.1	0.66 ± 0.05	27	20.41	8.13e-01
	extr	15	0.40	11.9 ± 4.0	3.0	133.7 ± 10.0	1.25 ± 0.08	12	2.47	9.98e-01
	-	-	-	0.0	-	155.7 ± 5.8	1.06 ± 0.04	13	9.44	7.39e-01
	flat	-	-	18.8 ± 3.7	5.0	123.9 ± 9.9	1.31 ± 0.09	12	3.68	9.89e-01
MACS J0242.5-2132	-	-	-	0.0	-	158.3 ± 5.9	1.01 ± 0.04	13	21.08	7.13e-02
	extr	22	0.50	9.7 ± 1.9	5.0	76.3 ± 5.1	1.27 ± 0.07	19	11.73	8.97e-01
	-	-	-	0.0	-	94.0 ± 3.2	1.01 ± 0.04	20	29.52	7.81e-02
	flat	-	-	10.9 ± 1.9	5.7	74.6 ± 5.0	1.29 ± 0.07	19	11.84	8.93e-01
MACS J0257.1-2325	-	-	-	0.0	-	94.4 ± 3.2	0.99 ± 0.03	20	34.37	2.37e-02
	extr	13	0.40	234.5 ± 68.2	3.4	195.8 ± 107.3	1.39 ± 0.57	10	0.24	1.00e+00
	-	-	-	0.0	-	489.1 ± 50.9	0.47 ± 0.12	11	3.07	9.90e-01
	flat	-	-	234.5 ± 68.2	3.4	195.8 ± 107.3	1.39 ± 0.57	10	0.24	1.00e+00
MACS J0257.6-2209	-	-	-	0.0	-	489.1 ± 50.9	0.47 ± 0.12	11	3.07	9.90e-01
	extr	17	0.40	155.1 ± 25.1	6.2	82.7 ± 32.5	1.55 ± 0.34	14	1.00	1.00e+00
	-	-	-	0.0	-	277.1 ± 15.3	0.56 ± 0.07	15	18.10	2.57e-01
	flat	-	-	155.9 ± 25.0	6.2	82.1 ± 32.4	1.55 ± 0.34	14	1.01	1.00e+00
MACS J0308.9+2645	-	-	-	0.0	-	277.6 ± 15.2	0.56 ± 0.07	15	18.25	2.49e-01
	extr	30	0.70	212.8 ± 53.9	3.9	70.1 ± 42.2	1.43 ± 0.35	27	0.86	1.00e+00
	-	-	-	0.0	-	290.5 ± 34.0	0.66 ± 0.10	28	7.88	1.00e+00
	flat	-	-	212.8 ± 53.9	3.9	70.1 ± 42.2	1.43 ± 0.35	27	0.86	1.00e+00
MACS J0329.6-0211	-	-	-	0.0	-	290.5 ± 34.0	0.66 ± 0.10	28	7.88	1.00e+00
	extr	14	0.40	6.6 ± 2.7	2.4	102.9 ± 6.5	1.21 ± 0.07	11	9.63	5.64e-01
	-	-	-	0.0	-	115.4 ± 3.6	1.08 ± 0.03	12	14.83	2.51e-01
	flat	-	-	11.1 ± 2.5	4.4	96.7 ± 6.4	1.26 ± 0.07	11	11.91	3.71e-01
MACS J0417.5-1154	-	-	-	0.0	-	117.5 ± 3.6	1.03 ± 0.03	12	26.77	8.33e-03
	extr	11	0.30	9.5 ± 6.7	1.4	101.6 ± 14.8	1.52 ± 0.22	8	0.88	9.99e-01
	-	-	-	0.0	-	117.2 ± 9.2	1.29 ± 0.13	9	2.51	9.81e-01
	flat	-	-	27.1 ± 7.3	3.7	99.7 ± 15.1	1.42 ± 0.23	8	1.16	9.97e-01
MACS J0429.6-0253	-	-	-	0.0	-	136.1 ± 9.4	0.85 ± 0.08	9	7.22	6.14e-01
	extr	15	0.40	14.8 ± 4.4	3.4	91.4 ± 9.0	1.21 ± 0.11	12	2.46	9.98e-01
	-	-	-	0.0	-	115.3 ± 4.7	0.95 ± 0.05	13	10.52	6.51e-01
	flat	-	-	17.2 ± 4.3	4.0	88.9 ± 9.0	1.23 ± 0.11	12	2.52	9.98e-01
MACS J0520.7-1328	-	-	-	0.0	-	116.5 ± 4.7	0.92 ± 0.05	13	13.22	4.31e-01
	extr	21	0.50	88.6 ± 22.0	4.0	84.9 ± 28.2	1.20 ± 0.24	18	0.75	1.00e+00
	-	-	-	0.0	-	194.8 ± 12.0	0.64 ± 0.07	19	8.63	9.79e-01
	flat	-	-	88.6 ± 22.0	4.0	84.9 ± 28.2	1.20 ± 0.24	18	0.75	1.00e+00
MACS J0547.0-3904	-	-	-	0.0	-	194.8 ± 12.0	0.64 ± 0.07	19	8.63	9.79e-01
	extr	24	0.40	22.0 ± 4.4	5.0	122.6 ± 10.2	1.19 ± 0.10	21	7.76	9.96e-01
	-	-	-	0.0	-	153.5 ± 6.9	0.84 ± 0.04	22	23.85	3.55e-01
	flat	-	-	23.1 ± 4.4	5.2	121.6 ± 10.2	1.20 ± 0.10	21	7.65	9.96e-01
MACS J0717.5+3745	-	-	-	0.0	-	153.7 ± 7.0	0.83 ± 0.04	22	25.01	2.97e-01
	extr	16	0.50	158.7 ± 111.6	1.4	202.0 ± 128.8	0.69 ± 0.35	13	1.31	1.00e+00
	-	-	-	0.0	-	378.6 ± 26.0	0.40 ± 0.07	14	2.63	1.00e+00
	flat	-	-	220.1 ± 96.4	2.3	160.1 ± 112.2	0.76 ± 0.40	13	1.03	1.00e+00

Table 5—Continued

Cluster	Method	N_{bins}	r_{max} Mpc	K_0 keV cm ²	$\sigma_{K_0} > 0$	K_{100} keV cm ²	α	DOF	χ^2	p-value
(1)	(2)	(3)	(4)	(5)	(6)	(7)	(8)	(9)	(10)	(11)
MACS J0744.8+3927	-	-	-	0.0	-	404.8 ± 25.2	0.33 ± 0.06	14	3.02	9.99e-01
	extr	17	0.60	39.5 ± 11.0	3.6	113.9 ± 17.4	1.10 ± 0.11	14	3.84	9.96e-01
	-	-	-	0.0	-	170.4 ± 7.6	0.81 ± 0.05	15	11.91	6.86e-01
	flat	-	-	42.4 ± 10.9	3.9	112.0 ± 17.2	1.11 ± 0.12	14	3.88	9.96e-01
MACS J1115.2+5320	-	-	-	0.0	-	172.6 ± 7.5	0.79 ± 0.04	15	12.98	6.04e-01
	extr	18	0.50	292.3 ± 60.5	4.8	27.6 ± 42.3	1.73 ± 1.01	15	3.47	9.99e-01
	-	-	-	0.0	-	334.8 ± 32.1	0.33 ± 0.10	16	6.98	9.74e-01
	flat	-	-	292.3 ± 60.5	4.8	27.6 ± 42.3	1.73 ± 1.01	15	3.47	9.99e-01
MACS J1115.8+0129	-	-	-	0.0	-	334.8 ± 32.1	0.33 ± 0.10	16	6.98	9.74e-01
	extr	20	0.20	14.1 ± 5.1	2.8	265.5 ± 18.4	1.26 ± 0.11	17	5.12	9.97e-01
	-	-	-	0.0	-	278.8 ± 17.7	1.05 ± 0.06	18	13.05	7.89e-01
	flat	-	-	22.7 ± 4.9	4.7	253.8 ± 18.4	1.32 ± 0.12	17	5.50	9.96e-01
MACS J1131.8-1955	-	-	-	0.0	-	270.5 ± 17.7	0.96 ± 0.05	18	24.02	1.54e-01
	extr	23	0.50	62.1 ± 22.3	2.8	160.9 ± 33.8	1.18 ± 0.18	20	0.40	1.00e+00
	-	-	-	0.0	-	246.2 ± 16.5	0.84 ± 0.08	21	6.22	9.99e-01
	flat	-	-	97.3 ± 23.0	4.2	156.3 ± 34.7	1.15 ± 0.19	20	0.69	1.00e+00
MACS J1149.5+2223	-	-	-	0.0	-	287.7 ± 15.5	0.64 ± 0.06	21	9.81	9.81e-01
	extr	32	1.00	280.7 ± 39.2	7.2	33.1 ± 20.6	1.47 ± 0.30	29	1.62	1.00e+00
	-	-	-	0.0	-	282.3 ± 22.1	0.52 ± 0.06	30	15.32	9.88e-01
	flat	-	-	280.7 ± 39.2	7.2	33.1 ± 20.6	1.47 ± 0.30	29	1.62	1.00e+00
MACS J1206.2-0847	-	-	-	0.0	-	282.3 ± 22.1	0.52 ± 0.06	30	15.32	9.88e-01
	extr	30	0.80	61.0 ± 10.1	6.0	97.1 ± 14.6	1.27 ± 0.11	27	1.38	1.00e+00
	-	-	-	0.0	-	181.0 ± 8.5	0.84 ± 0.05	28	25.36	6.08e-01
	flat	-	-	69.0 ± 10.1	6.8	94.7 ± 14.5	1.28 ± 0.11	27	1.87	1.00e+00
MACS J1311.0-0310	-	-	-	0.0	-	190.5 ± 8.3	0.78 ± 0.05	28	30.00	3.63e-01
	extr	14	0.40	42.5 ± 4.2	10.1	67.1 ± 7.4	1.58 ± 0.12	11	2.47	9.96e-01
	-	-	-	0.0	-	127.7 ± 3.9	0.84 ± 0.04	12	67.11	1.11e-09
	flat	-	-	47.4 ± 4.1	11.5	63.5 ± 7.3	1.62 ± 0.12	11	2.39	9.97e-01
MACS J1621.3+3810	-	-	-	0.0	-	130.2 ± 3.9	0.77 ± 0.04	12	77.77	1.10e-11
	extr	17	0.50	13.9 ± 5.6	2.5	135.0 ± 11.6	1.16 ± 0.08	14	6.71	9.45e-01
	-	-	-	0.0	-	158.9 ± 5.8	1.01 ± 0.04	15	11.72	7.00e-01
	flat	-	-	20.1 ± 5.4	3.7	129.8 ± 11.4	1.18 ± 0.08	14	7.04	9.33e-01
MACS J1931.8-2634	-	-	-	0.0	-	164.4 ± 5.8	0.96 ± 0.04	15	16.97	3.21e-01
	extr	16	0.40	10.3 ± 3.8	2.7	93.7 ± 9.3	1.22 ± 0.10	13	4.58	9.83e-01
	-	-	-	0.0	-	112.9 ± 5.1	1.01 ± 0.05	14	10.52	7.23e-01
	flat	-	-	14.6 ± 3.6	4.1	87.5 ± 9.2	1.27 ± 0.11	13	5.80	9.53e-01
MACS J2049.9-3217	-	-	-	0.0	-	114.6 ± 5.1	0.97 ± 0.04	14	17.89	2.12e-01
	extr	21	0.50	195.8 ± 67.6	2.9	92.7 ± 71.5	1.06 ± 0.48	18	0.87	1.00e+00
	-	-	-	0.0	-	309.0 ± 25.4	0.43 ± 0.08	19	3.69	1.00e+00
	flat	-	-	195.8 ± 67.6	2.9	92.7 ± 71.5	1.06 ± 0.48	18	0.87	1.00e+00
MACS J2211.7-0349	-	-	-	0.0	-	309.0 ± 25.4	0.43 ± 0.08	19	3.69	1.00e+00
	extr	29	0.60	165.5 ± 25.5	6.5	78.3 ± 26.3	1.59 ± 0.24	26	0.89	1.00e+00
	-	-	-	0.0	-	270.5 ± 16.5	0.74 ± 0.07	27	20.58	8.06e-01
	flat	-	-	165.5 ± 25.5	6.5	78.3 ± 26.3	1.59 ± 0.24	26	0.89	1.00e+00

Table 5—Continued

Cluster	Method	N_{bins}	r_{max} Mpc	K_0 keV cm ²	$\sigma_{K_0} > 0$	K_{100} keV cm ²	α	DOF	χ^2	p-value
(1)	(2)	(3)	(4)	(5)	(6)	(7)	(8)	(9)	(10)	(11)
MACS J2214.9-1359	-	-	-	0.0	-	270.5 ± 16.5	0.74 ± 0.07	27	20.58	8.06e-01
	extr	13	0.40	238.6 ± 88.3	2.7	203.6 ± 152.6	1.38 ± 0.66	10	0.08	1.00e+00
	-	-	-	0.0	-	507.6 ± 70.9	0.52 ± 0.16	11	2.25	9.97e-01
	flat	-	-	297.7 ± 83.2	3.6	172.0 ± 147.7	1.46 ± 0.76	10	0.10	1.00e+00
MACS J2228+2036	-	-	-	0.0	-	534.0 ± 73.0	0.40 ± 0.14	11	2.62	9.95e-01
	extr	22	0.60	118.8 ± 39.2	3.0	107.2 ± 45.9	1.00 ± 0.26	19	0.60	1.00e+00
	-	-	-	0.0	-	246.7 ± 17.6	0.55 ± 0.07	20	4.67	1.00e+00
	flat	-	-	118.8 ± 39.2	3.0	107.2 ± 45.9	1.00 ± 0.26	19	0.60	1.00e+00
MACS J2229.7-2755	-	-	-	0.0	-	246.7 ± 17.6	0.55 ± 0.07	20	4.67	1.00e+00
	extr	17	0.40	10.2 ± 2.1	4.8	78.1 ± 5.2	1.32 ± 0.08	14	12.45	5.70e-01
	-	-	-	0.0	-	95.0 ± 3.4	1.04 ± 0.04	15	30.08	1.16e-02
	flat	-	-	12.4 ± 2.0	6.1	75.0 ± 5.2	1.36 ± 0.08	14	13.61	4.79e-01
MACS J2245.0+2637	-	-	-	0.0	-	95.4 ± 3.4	1.01 ± 0.04	15	39.96	4.60e-04
	extr	23	0.50	39.0 ± 6.6	5.9	108.5 ± 13.1	1.31 ± 0.12	20	0.54	1.00e+00
	-	-	-	0.0	-	166.7 ± 7.2	0.82 ± 0.05	21	23.13	3.37e-01
	flat	-	-	42.0 ± 6.5	6.5	105.9 ± 13.1	1.33 ± 0.13	20	0.53	1.00e+00
MKW3S	-	-	-	0.0	-	168.1 ± 7.2	0.79 ± 0.05	21	25.90	2.10e-01
	extr	46	0.20	20.7 ± 1.7	12.1	134.8 ± 2.6	0.93 ± 0.03	43	26.23	9.80e-01
	-	-	-	0.0	-	154.3 ± 1.8	0.66 ± 0.01	44	121.79	3.16e-09
	flat	-	-	23.9 ± 1.6	14.7	131.1 ± 2.5	0.96 ± 0.03	43	27.65	9.67e-01
MKW 4	-	-	-	0.0	-	153.5 ± 1.8	0.65 ± 0.01	44	159.12	6.08e-15
	extr	16	0.03	5.9 ± 0.3	18.9	368.4 ± 26.7	1.21 ± 0.04	13	17.01	1.99e-01
	-	-	-	0.0	-	164.0 ± 6.7	0.74 ± 0.01	14	233.26	8.23e-42
	flat	-	-	6.9 ± 0.3	23.0	392.7 ± 29.4	1.26 ± 0.04	13	19.05	1.21e-01
MKW 8	-	-	-	0.0	-	146.6 ± 5.9	0.70 ± 0.01	14	305.78	7.37e-57
	extr	19	0.05	130.7 ± 22.4	5.8	228.5 ± 54.2	0.87 ± 0.40	16	0.44	1.00e+00
	-	-	-	0.0	-	275.3 ± 16.3	0.22 ± 0.03	17	4.86	9.98e-01
	flat	-	-	130.7 ± 22.4	5.8	228.5 ± 54.2	0.87 ± 0.40	16	0.44	1.00e+00
MS J0016.9+1609	-	-	-	0.0	-	275.3 ± 16.3	0.22 ± 0.03	17	4.86	9.98e-01
	extr	16	0.50	160.7 ± 22.6	7.1	65.0 ± 26.7	1.28 ± 0.30	13	3.17	9.97e-01
	-	-	-	0.0	-	258.5 ± 11.8	0.40 ± 0.05	14	15.63	3.37e-01
	flat	-	-	162.1 ± 22.5	7.2	64.2 ± 26.5	1.29 ± 0.30	13	3.17	9.97e-01
MS J0116.3-0115	-	-	-	0.0	-	259.3 ± 11.7	0.40 ± 0.05	14	15.74	3.30e-01
	extr	22	0.10	17.2 ± 32.0	0.5	214.2 ± 24.7	0.62 ± 0.23	19	2.51	1.00e+00
	-	-	-	0.0	-	225.3 ± 14.8	0.52 ± 0.05	20	3.02	1.00e+00
	flat	-	-	12.8 ± 31.0	0.4	220.8 ± 24.1	0.63 ± 0.22	19	2.53	1.00e+00
MS J0440.5+0204	-	-	-	0.0	-	228.7 ± 15.1	0.55 ± 0.05	20	2.96	1.00e+00
	extr	19	0.30	22.8 ± 7.6	3.0	165.5 ± 15.1	1.11 ± 0.13	16	5.73	9.91e-01
	-	-	-	0.0	-	196.6 ± 9.6	0.82 ± 0.06	17	11.13	8.50e-01
	flat	-	-	25.5 ± 7.6	3.4	164.0 ± 15.2	1.11 ± 0.13	16	6.15	9.86e-01
MS J0451.6-0305	-	-	-	0.0	-	198.0 ± 9.6	0.79 ± 0.05	17	12.34	7.79e-01
	extr	16	0.50	568.1 ± 115.6	4.9	15.6 ± 49.9	2.81 ± 2.27	13	0.56	1.00e+00
	-	-	-	0.0	-	643.5 ± 79.7	0.21 ± 0.16	14	3.73	9.97e-01
	flat	-	-	568.1 ± 115.6	4.9	15.6 ± 49.9	2.81 ± 2.27	13	0.56	1.00e+00

Table 5—Continued

Cluster	Method	N_{bins}	r_{max} Mpc	K_0 keV cm ²	$\sigma_{K_0} > 0$	K_{100} keV cm ²	α	DOF	χ^2	p-value
(1)	(2)	(3)	(4)	(5)	(6)	(7)	(8)	(9)	(10)	(11)
MS J0735.6+7421	-	-	-	0.0	-	643.5 \pm 79.7	0.21 \pm 0.16	14	3.73	9.97e-01
	extr	18	0.30	13.8 \pm 2.2	6.3	109.9 \pm 4.6	1.12 \pm 0.05	15	22.06	1.06e-01
	-	-	-	0.0	-	131.3 \pm 2.7	0.89 \pm 0.02	16	60.72	3.95e-07
	flat	-	-	16.0 \pm 2.1	7.5	106.8 \pm 4.6	1.14 \pm 0.05	15	25.59	4.26e-02
MS J0839.8+2938	-	-	-	0.0	-	131.5 \pm 2.7	0.87 \pm 0.02	16	77.93	3.92e-10
	extr	16	0.25	15.5 \pm 3.1	5.1	110.7 \pm 6.3	1.26 \pm 0.11	13	3.12	9.98e-01
	-	-	-	0.0	-	127.3 \pm 4.9	0.88 \pm 0.04	14	21.16	9.75e-02
	flat	-	-	19.2 \pm 2.9	6.7	105.8 \pm 6.3	1.33 \pm 0.11	13	2.50	9.99e-01
MS J0906.5+1110	-	-	-	0.0	-	126.1 \pm 4.9	0.84 \pm 0.04	14	30.67	6.17e-03
	extr	29	0.40	104.2 \pm 14.9	7.0	97.3 \pm 19.6	1.15 \pm 0.17	26	1.25	1.00e+00
	-	-	-	0.0	-	222.7 \pm 6.4	0.54 \pm 0.04	27	19.62	8.46e-01
	flat	-	-	104.2 \pm 14.9	7.0	97.3 \pm 19.6	1.15 \pm 0.17	26	1.25	1.00e+00
MS J1006.0+1202	-	-	-	0.0	-	222.7 \pm 6.4	0.54 \pm 0.04	27	19.62	8.46e-01
	extr	29	0.50	175.8 \pm 20.1	8.7	71.7 \pm 25.0	1.40 \pm 0.26	26	7.00	1.00e+00
	-	-	-	0.0	-	285.4 \pm 12.1	0.41 \pm 0.05	27	29.77	3.25e-01
	flat	-	-	160.3 \pm 21.3	7.5	82.8 \pm 26.9	1.32 \pm 0.24	26	6.68	1.00e+00
MS J1008.1-1224	-	-	-	0.0	-	278.4 \pm 12.2	0.46 \pm 0.05	27	26.32	5.01e-01
	extr	23	0.50	96.0 \pm 40.7	2.4	260.2 \pm 56.0	0.77 \pm 0.18	20	1.45	1.00e+00
	-	-	-	0.0	-	373.9 \pm 18.0	0.49 \pm 0.05	21	4.07	1.00e+00
	flat	-	-	97.6 \pm 41.5	2.4	262.0 \pm 56.8	0.76 \pm 0.18	20	1.50	1.00e+00
MS J1455.0+2232	-	-	-	0.0	-	377.0 \pm 18.1	0.48 \pm 0.05	21	4.07	1.00e+00
	extr	16	0.30	16.9 \pm 1.5	11.1	81.5 \pm 4.0	1.39 \pm 0.07	13	10.09	6.86e-01
	-	-	-	0.0	-	107.3 \pm 2.7	0.86 \pm 0.03	14	80.05	2.76e-11
	flat	-	-	16.9 \pm 1.5	11.1	81.5 \pm 4.0	1.39 \pm 0.07	13	10.09	6.86e-01
MS J2137.3-2353	-	-	-	0.0	-	107.3 \pm 2.7	0.86 \pm 0.03	14	80.05	2.76e-11
	extr	22	0.50	12.3 \pm 1.9	6.5	93.5 \pm 5.3	1.36 \pm 0.06	19	5.01	9.99e-01
	-	-	-	0.0	-	116.9 \pm 3.4	1.08 \pm 0.03	20	36.15	1.47e-02
	flat	-	-	14.7 \pm 1.8	7.9	89.9 \pm 5.3	1.39 \pm 0.06	19	5.76	9.98e-01
MS J1157.3+5531	-	-	-	0.0	-	117.6 \pm 3.4	1.05 \pm 0.03	20	50.37	1.96e-04
	extr	13	0.10	4.1 \pm 0.4	9.7	283.8 \pm 17.7	1.44 \pm 0.05	10	7.54	6.74e-01
	-	-	-	0.0	-	196.2 \pm 9.6	1.09 \pm 0.02	11	64.85	1.15e-09
	flat	-	-	5.9 \pm 0.4	13.9	277.0 \pm 17.7	1.45 \pm 0.05	10	7.22	7.04e-01
NGC 507	-	-	-	0.0	-	160.6 \pm 7.7	0.95 \pm 0.02	11	96.24	9.86e-16
	extr	61	0.05	0.0 \pm 2.1	0.0	101.7 \pm 2.8	0.67 \pm 0.01	58	42.84	9.32e-01
	-	-	-	0.0	-	101.7 \pm 2.8	0.67 \pm 0.01	59	42.84	9.44e-01
	flat	-	-	0.0 \pm 2.1	0.0	99.9 \pm 2.7	0.65 \pm 0.01	58	46.55	8.60e-01
NGC 4636	-	-	-	0.0	-	99.9 \pm 2.7	0.65 \pm 0.01	59	46.55	8.80e-01
	extr	12	0.00	1.4 \pm 0.1	13.4	10674.9 \pm 7937.9	1.93 \pm 0.18	9	8.12	5.22e-01
	-	-	-	0.0	-	108.2 \pm 19.2	0.77 \pm 0.04	10	56.25	1.84e-08
	flat	-	-	1.4 \pm 0.1	13.9	11962.1 \pm 8977.0	1.96 \pm 0.18	9	8.95	4.42e-01
NGC 5044	-	-	-	0.0	-	104.9 \pm 18.6	0.77 \pm 0.04	10	60.03	3.58e-09
	extr	66	0.03	1.9 \pm 0.3	7.2	79.6 \pm 6.7	0.93 \pm 0.05	63	49.49	8.93e-01
	-	-	-	0.0	-	55.1 \pm 2.4	0.67 \pm 0.02	64	77.04	1.27e-01
	flat	-	-	2.3 \pm 0.3	8.9	82.2 \pm 7.2	0.96 \pm 0.05	63	48.05	9.18e-01

Table 5—Continued

Cluster	Method	N_{bins}	r_{max} Mpc	K_0 keV cm ²	$\sigma_{K_0} > 0$	K_{100} keV cm ²	α	DOF	χ^2	p-value
(1)	(2)	(3)	(4)	(5)	(6)	(7)	(8)	(9)	(10)	(11)
NGC 5813	-	-	-	0.0	-	52.3 ± 2.2	0.64 ± 0.02	64	86.52	3.19e-02
	extr	60	0.02	1.4 ± 0.2	8.9	102.5 ± 7.1	0.91 ± 0.03	57	107.52	6.00e-05
	-	-	-	0.0	-	69.3 ± 2.1	0.70 ± 0.01	58	161.30	1.14e-11
	flat	-	-	1.4 ± 0.2	8.9	102.5 ± 7.1	0.91 ± 0.03	57	107.52	6.00e-05
NGC 5846	-	-	-	0.0	-	69.3 ± 2.1	0.70 ± 0.01	58	161.30	1.14e-11
	extr	16	0.00	1.8 ± 0.2	10.7	685.8 ± 344.9	1.44 ± 0.15	13	1.16	1.00e+00
	-	-	-	0.0	-	52.7 ± 7.3	0.63 ± 0.03	14	40.72	1.97e-04
	flat	-	-	1.8 ± 0.2	10.7	685.8 ± 344.9	1.44 ± 0.15	13	1.16	1.00e+00
Ophiuchus	-	-	-	0.0	-	52.7 ± 7.3	0.63 ± 0.03	14	40.72	1.97e-04
	extr	18	0.05	4.0 ± 0.6	6.3	375.1 ± 12.8	1.06 ± 0.03	15	9.75	8.35e-01
	-	-	-	0.0	-	328.4 ± 7.8	0.92 ± 0.01	16	42.24	3.63e-04
	flat	-	-	8.9 ± 1.2	7.5	247.5 ± 7.6	0.73 ± 0.03	15	95.06	1.12e-13
PKS 0745-191	-	-	-	0.0	-	217.0 ± 3.9	0.58 ± 0.01	16	127.43	2.02e-19
	extr	34	0.30	11.9 ± 0.7	17.4	111.7 ± 2.7	1.38 ± 0.04	31	17.17	9.79e-01
	-	-	-	0.0	-	129.2 ± 2.4	0.98 ± 0.02	32	245.68	8.53e-35
	flat	-	-	12.4 ± 0.7	18.3	110.7 ± 2.7	1.39 ± 0.04	31	19.54	9.45e-01
RBS 461	-	-	-	0.0	-	128.9 ± 2.4	0.97 ± 0.02	32	270.30	1.59e-39
	extr	70	0.20	95.7 ± 3.0	31.4	68.8 ± 4.5	1.39 ± 0.10	67	22.14	1.00e+00
	-	-	-	0.0	-	173.2 ± 1.8	0.35 ± 0.01	68	217.68	1.45e-17
	flat	-	-	95.7 ± 3.0	31.4	68.8 ± 4.5	1.39 ± 0.10	67	22.14	1.00e+00
RBS 533	-	-	-	0.0	-	173.2 ± 1.8	0.35 ± 0.01	68	217.68	1.45e-17
	extr	44	0.06	2.0 ± 0.05	39.5	162.8 ± 2.5	0.99 ± 0.01	41	202.89	2.65e-23
	-	-	-	0.0	-	113.5 ± 1.3	0.76 ± 0.00	42	1282.66	1.75e-241
	flat	-	-	2.2 ± 0.05	43.7	164.3 ± 2.5	1.00 ± 0.01	41	215.65	1.46e-25
RBS 797	-	-	-	0.0	-	110.0 ± 1.3	0.75 ± 0.00	42	1490.02	3.27e-285
	extr	24	0.30	20.0 ± 2.4	8.3	95.2 ± 9.0	1.72 ± 0.14	21	89.64	1.86e-10
	-	-	-	0.0	-	116.2 ± 8.0	0.98 ± 0.06	22	1061.58	1.51e-210
	flat	-	-	20.9 ± 2.4	8.9	93.2 ± 9.1	1.75 ± 0.15	21	104.70	4.22e-13
RCS J2327-0204	-	-	-	0.0	-	114.6 ± 8.0	0.96 ± 0.06	22	1188.56	1.25e-237
	extr	18	0.30	65.5 ± 20.2	3.2	220.6 ± 37.0	1.27 ± 0.25	15	31.21	8.24e-03
	-	-	-	0.0	-	300.3 ± 22.5	0.74 ± 0.09	16	119.10	8.17e-18
	flat	-	-	68.5 ± 19.9	3.4	217.2 ± 36.9	1.28 ± 0.26	15	31.00	8.80e-03
RXCJ0331.1-2100	-	-	-	0.0	-	300.1 ± 22.6	0.73 ± 0.09	16	126.00	3.83e-19
	extr	25	0.20	6.4 ± 1.6	4.1	141.0 ± 5.8	1.23 ± 0.06	22	325.76	7.05e-56
	-	-	-	0.0	-	145.9 ± 5.7	1.05 ± 0.03	23	677.70	2.20e-128
	flat	-	-	11.4 ± 1.5	7.7	134.1 ± 5.8	1.30 ± 0.07	22	356.18	4.25e-62
RX J0220.9-3829	-	-	-	0.0	-	140.5 ± 5.7	0.95 ± 0.03	23	1408.70	8.65e-284
	extr	22	0.40	33.1 ± 6.2	5.3	163.7 ± 14.0	1.25 ± 0.11	19	3.90	1.00e+00
	-	-	-	0.0	-	211.1 ± 9.0	0.84 ± 0.05	20	20.59	4.22e-01
	flat	-	-	43.0 ± 6.3	6.8	159.9 ± 14.0	1.23 ± 0.12	19	4.20	1.00e+00
RX J0232.2-4420	-	-	-	0.0	-	216.2 ± 9.2	0.73 ± 0.04	20	25.95	1.68e-01
	extr	14	0.30	34.2 ± 13.0	2.6	176.3 ± 25.0	1.12 ± 0.18	11	0.85	1.00e+00
	-	-	-	0.0	-	225.4 ± 13.1	0.80 ± 0.06	12	5.16	9.53e-01
	flat	-	-	44.6 ± 12.4	3.6	166.5 ± 24.7	1.16 ± 0.18	11	0.71	1.00e+00

Table 5—Continued

Cluster	Method	N_{bins}	r_{max} Mpc	K_0 keV cm ²	$\sigma_{K_0} > 0$	K_{100} keV cm ²	α	DOF	χ^2	p-value
(1)	(2)	(3)	(4)	(5)	(6)	(7)	(8)	(9)	(10)	(11)
RX J0439+0520	-	-	-	0.0	-	228.9 ± 13.2	0.74 ± 0.06	12	7.42	8.28e-01
	extr	18	0.30	12.8 ± 2.9	4.5	97.1 ± 6.2	1.18 ± 0.10	15	6.80	9.63e-01
	-	-	-	0.0	-	112.8 ± 4.6	0.86 ± 0.04	16	19.20	2.59e-01
	flat	-	-	14.9 ± 2.9	5.2	95.5 ± 6.2	1.19 ± 0.10	15	6.64	9.67e-01
RX J0439.0+0715	-	-	-	0.0	-	113.0 ± 4.6	0.82 ± 0.04	16	21.93	1.45e-01
	extr	22	0.40	61.2 ± 21.3	2.9	152.0 ± 31.1	0.95 ± 0.18	19	5.54	9.99e-01
	-	-	-	0.0	-	212.0 ± 10.6	0.68 ± 0.06	20	8.75	9.86e-01
	flat	-	-	66.8 ± 18.5	3.6	129.6 ± 28.4	1.06 ± 0.20	19	6.20	9.97e-01
RX J0528.9-3927	-	-	-	0.0	-	217.0 ± 10.5	0.63 ± 0.06	20	13.41	8.59e-01
	extr	21	0.40	69.9 ± 13.9	5.0	102.2 ± 22.6	1.45 ± 0.23	18	1.71	1.00e+00
	-	-	-	0.0	-	201.5 ± 11.3	0.74 ± 0.08	19	15.10	7.16e-01
	flat	-	-	72.9 ± 13.8	5.3	99.8 ± 22.4	1.47 ± 0.23	18	1.67	1.00e+00
RX J0647.7+7015	-	-	-	0.0	-	203.1 ± 11.3	0.72 ± 0.07	19	15.94	6.61e-01
	extr	24	0.80	225.1 ± 47.1	4.8	48.8 ± 31.9	1.70 ± 0.39	21	0.42	1.00e+00
	-	-	-	0.0	-	275.6 ± 32.0	0.71 ± 0.10	22	9.72	9.89e-01
	flat	-	-	225.1 ± 47.1	4.8	48.8 ± 31.9	1.70 ± 0.39	21	0.42	1.00e+00
RX J0819.6+6336	-	-	-	0.0	-	275.6 ± 32.0	0.71 ± 0.10	22	9.72	9.89e-01
	extr	28	0.30	20.7 ± 14.3	1.5	170.6 ± 19.4	0.68 ± 0.12	25	10.13	9.96e-01
	-	-	-	0.0	-	194.0 ± 8.8	0.55 ± 0.04	26	11.55	9.93e-01
	flat	-	-	20.7 ± 14.3	1.5	170.6 ± 19.4	0.68 ± 0.12	25	10.13	9.96e-01
RX J1000.4+4409	-	-	-	0.0	-	194.0 ± 8.8	0.55 ± 0.04	26	11.55	9.93e-01
	extr	23	0.30	23.1 ± 4.3	5.4	151.7 ± 9.9	1.12 ± 0.09	20	1.85	1.00e+00
	-	-	-	0.0	-	182.2 ± 7.1	0.77 ± 0.04	21	18.65	6.07e-01
	flat	-	-	27.7 ± 4.4	6.3	151.1 ± 9.9	1.09 ± 0.09	20	1.94	1.00e+00
RX J1022.1+3830	-	-	-	0.0	-	184.9 ± 7.2	0.71 ± 0.03	21	21.59	4.24e-01
	extr	18	0.09	44.0 ± 10.0	4.4	206.8 ± 18.5	1.03 ± 0.21	15	7.73	9.34e-01
	-	-	-	0.0	-	208.7 ± 11.4	0.54 ± 0.04	16	13.56	6.32e-01
	flat	-	-	51.6 ± 9.8	5.3	194.8 ± 18.7	1.04 ± 0.22	15	8.26	9.13e-01
RX J1130.0+3637	-	-	-	0.0	-	201.1 ± 10.7	0.48 ± 0.04	16	14.68	5.48e-01
	extr	26	0.15	23.4 ± 2.2	10.7	158.7 ± 9.3	1.19 ± 0.09	23	2.01	1.00e+00
	-	-	-	0.0	-	140.8 ± 6.7	0.60 ± 0.03	24	54.32	3.86e-04
	flat	-	-	29.9 ± 2.3	12.9	149.6 ± 9.2	1.14 ± 0.10	23	2.81	1.00e+00
RX J1320.2+3308	-	-	-	0.0	-	133.0 ± 6.0	0.48 ± 0.02	24	58.11	1.18e-04
	extr	11	0.04	7.6 ± 0.6	12.1	162.6 ± 26.6	1.36 ± 0.12	8	5.25	7.31e-01
	-	-	-	0.0	-	67.6 ± 4.2	0.61 ± 0.03	9	50.82	7.56e-08
	flat	-	-	8.8 ± 0.7	13.1	140.3 ± 23.4	1.28 ± 0.12	8	7.01	5.36e-01
RX J1347.5-1145	-	-	-	0.0	-	59.9 ± 3.4	0.53 ± 0.02	9	49.88	1.13e-07
	extr	8	0.22	12.5 ± 20.7	0.6	179.9 ± 35.3	1.06 ± 0.34	5	4.00	5.49e-01
	-	-	-	0.0	-	196.4 ± 18.3	0.90 ± 0.08	6	4.23	6.46e-01
	flat	-	-	12.5 ± 20.7	0.6	179.9 ± 35.3	1.06 ± 0.34	5	4.00	5.49e-01
RX J1423.8+2404	-	-	-	0.0	-	196.4 ± 18.3	0.90 ± 0.08	6	4.23	6.46e-01
	extr	7	0.22	10.2 ± 5.0	2.0	119.9 ± 10.8	1.27 ± 0.17	4	1.75	7.82e-01
	-	-	-	0.0	-	133.8 ± 7.3	1.02 ± 0.05	5	15.01	1.03e-02
	flat	-	-	10.2 ± 5.0	2.0	119.9 ± 10.8	1.27 ± 0.17	4	1.75	7.82e-01

Table 5—Continued

Cluster	Method	N_{bins}	r_{max} Mpc	K_0 keV cm ²	$\sigma_{K_0} > 0$	K_{100} keV cm ²	α	DOF	χ^2	p-value
(1)	(2)	(3)	(4)	(5)	(6)	(7)	(8)	(9)	(10)	(11)
RX J1504.1-0248	-	-	-	0.0	-	133.8 ± 7.3	1.02 ± 0.05	5	15.01	1.03e-02
	extr	27	0.45	13.1 ± 0.9	13.9	95.6 ± 3.5	1.50 ± 0.04	24	2.89	1.00e+00
	-	-	-	0.0	-	121.2 ± 2.7	1.09 ± 0.02	25	154.86	1.07e-20
	flat	-	-	13.1 ± 0.9	13.9	95.6 ± 3.5	1.50 ± 0.04	24	2.89	1.00e+00
RX J1532.9+3021	-	-	-	0.0	-	121.2 ± 2.7	1.09 ± 0.02	25	154.86	1.07e-20
	extr	21	0.50	14.3 ± 1.9	7.6	80.3 ± 5.0	1.46 ± 0.07	18	2.24	1.00e+00
	-	-	-	0.0	-	105.6 ± 3.3	1.08 ± 0.04	19	48.03	2.54e-04
	flat	-	-	16.9 ± 1.8	9.3	76.3 ± 5.0	1.51 ± 0.07	18	2.38	1.00e+00
RX J1539.5-8335	-	-	-	0.0	-	106.1 ± 3.3	1.04 ± 0.04	19	67.16	2.71e-07
	extr	29	0.20	21.8 ± 3.1	7.1	115.1 ± 5.8	1.32 ± 0.11	26	13.29	9.81e-01
	-	-	-	0.0	-	135.3 ± 4.5	0.83 ± 0.04	27	40.39	4.71e-02
	flat	-	-	25.9 ± 2.9	9.1	110.0 ± 5.8	1.41 ± 0.12	26	13.52	9.79e-01
RX J1720.1+2638	-	-	-	0.0	-	133.7 ± 4.5	0.79 ± 0.04	27	54.08	1.49e-03
	extr	30	0.40	20.7 ± 1.9	10.7	109.7 ± 5.4	1.38 ± 0.06	27	5.34	1.00e+00
	-	-	-	0.0	-	145.3 ± 3.6	0.98 ± 0.03	28	94.37	4.06e-09
	flat	-	-	21.0 ± 1.9	10.9	109.1 ± 5.4	1.39 ± 0.06	27	5.56	1.00e+00
RX J1720.2+3536	-	-	-	0.0	-	145.3 ± 3.6	0.98 ± 0.03	28	97.94	1.09e-09
	extr	13	0.32	17.5 ± 3.5	4.9	101.8 ± 7.9	1.35 ± 0.10	10	2.47	9.91e-01
	-	-	-	0.0	-	129.4 ± 4.7	1.00 ± 0.04	11	23.76	1.38e-02
	flat	-	-	24.0 ± 3.3	7.2	94.4 ± 7.8	1.42 ± 0.11	10	2.67	9.88e-01
RX J1852.1+5711	-	-	-	0.0	-	131.3 ± 4.7	0.92 ± 0.04	11	40.43	3.02e-05
	extr	12	0.12	13.7 ± 6.3	2.2	184.3 ± 12.8	0.96 ± 0.15	9	2.63	9.77e-01
	-	-	-	0.0	-	182.4 ± 10.9	0.73 ± 0.05	10	5.31	8.70e-01
	flat	-	-	18.7 ± 8.3	2.3	170.4 ± 11.8	0.83 ± 0.16	9	5.06	8.29e-01
RX J2129.6+0005	-	-	-	0.0	-	173.3 ± 9.8	0.58 ± 0.04	10	7.26	7.01e-01
	extr	22	0.40	18.0 ± 3.8	4.7	100.8 ± 8.1	1.24 ± 0.10	19	7.01	9.94e-01
	-	-	-	0.0	-	129.2 ± 4.8	0.91 ± 0.05	20	21.36	3.76e-01
	flat	-	-	21.1 ± 3.7	5.7	97.9 ± 8.0	1.26 ± 0.10	19	7.16	9.93e-01
SC 1327-312	-	-	-	0.0	-	130.8 ± 4.8	0.87 ± 0.04	20	26.01	1.66e-01
	extr	31	0.15	65.5 ± 10.1	6.5	160.4 ± 12.5	0.80 ± 0.14	28	1.08	1.00e+00
	-	-	-	0.0	-	212.5 ± 8.1	0.36 ± 0.03	29	15.85	9.77e-01
	flat	-	-	64.6 ± 9.9	6.5	160.8 ± 12.5	0.81 ± 0.14	28	1.03	1.00e+00
Sersic 159-03	-	-	-	0.0	-	212.0 ± 8.1	0.37 ± 0.03	29	16.01	9.75e-01
	extr	23	0.12	7.5 ± 0.8	9.7	79.7 ± 2.3	1.06 ± 0.05	20	15.95	7.20e-01
	-	-	-	0.0	-	77.9 ± 2.0	0.72 ± 0.02	21	77.11	2.44e-08
	flat	-	-	10.5 ± 0.7	15.0	77.8 ± 2.4	1.17 ± 0.06	20	16.81	6.65e-01
SS2B153	-	-	-	0.0	-	74.0 ± 1.9	0.65 ± 0.02	21	136.22	7.00e-19
	extr	38	0.07	1.1 ± 0.2	6.9	71.4 ± 2.1	0.80 ± 0.02	35	24.19	9.15e-01
	-	-	-	0.0	-	63.4 ± 1.4	0.69 ± 0.01	36	59.46	8.24e-03
	flat	-	-	1.1 ± 0.2	6.9	71.4 ± 2.1	0.80 ± 0.02	35	24.19	9.15e-01
UGC 3957	-	-	-	0.0	-	63.4 ± 1.4	0.69 ± 0.01	36	59.46	8.24e-03
	extr	36	0.12	11.0 ± 1.0	11.2	180.8 ± 7.3	1.01 ± 0.04	33	6.63	1.00e+00
	-	-	-	0.0	-	151.9 ± 5.1	0.68 ± 0.02	34	84.60	3.37e-06
	flat	-	-	12.9 ± 1.0	12.5	175.1 ± 7.1	0.98 ± 0.04	33	6.95	1.00e+00

Table 5—Continued

Cluster	Method	N_{bins}	r_{max} Mpc	K_0 keV cm ²	$\sigma_{K_0} > 0$	K_{100} keV cm ²	α	DOF	χ^2	p-value
(1)	(2)	(3)	(4)	(5)	(6)	(7)	(8)	(9)	(10)	(11)
UGC 12491	-	-	-	0.0	-	144.2 ± 4.7	0.62 ± 0.02	34	91.61	3.48e-07
	extr	23	0.04	3.0 ± 0.2	13.8	148.5 ± 11.7	1.12 ± 0.04	20	445.44	7.29e-82
	-	-	-	0.0	-	77.4 ± 3.4	0.70 ± 0.02	21	2353.02	0.00e+00
	flat	-	-	3.0 ± 0.2	13.8	148.5 ± 11.7	1.12 ± 0.04	20	445.44	7.29e-82
ZWCL 1215	-	-	-	0.0	-	77.4 ± 3.4	0.70 ± 0.02	21	2353.02	0.00e+00
	extr	36	0.25	163.2 ± 35.6	4.6	131.3 ± 43.6	1.00 ± 0.32	33	2.94	1.00e+00
	-	-	-	0.0	-	314.8 ± 10.9	0.37 ± 0.05	34	7.69	1.00e+00
	flat	-	-	163.2 ± 35.6	4.6	131.3 ± 43.6	1.00 ± 0.32	33	2.94	1.00e+00
ZWCL 1358+6245	-	-	-	0.0	-	314.8 ± 10.9	0.37 ± 0.05	34	7.69	1.00e+00
	extr	26	0.60	13.8 ± 3.3	4.2	102.3 ± 9.5	1.40 ± 0.08	23	5.58	1.00e+00
	-	-	-	0.0	-	130.6 ± 6.1	1.15 ± 0.05	24	19.02	7.51e-01
	flat	-	-	20.7 ± 3.2	6.4	98.0 ± 9.4	1.43 ± 0.09	23	5.65	1.00e+00
ZWCL 1742	-	-	-	0.0	-	138.5 ± 6.1	1.04 ± 0.05	24	32.17	1.23e-01
	extr	17	0.12	13.8 ± 1.5	9.0	147.7 ± 9.4	1.39 ± 0.11	14	14.80	3.92e-01
	-	-	-	0.0	-	122.0 ± 6.1	0.78 ± 0.04	15	55.08	1.73e-06
	flat	-	-	23.8 ± 1.7	14.4	126.5 ± 9.0	1.30 ± 0.12	14	24.08	4.49e-02
ZWCL 1953	-	-	-	0.0	-	100.7 ± 4.5	0.48 ± 0.03	15	69.54	5.39e-09
	extr	17	0.45	194.5 ± 56.6	3.4	62.1 ± 57.0	1.39 ± 0.65	14	0.99	1.00e+00
	-	-	-	0.0	-	283.3 ± 27.3	0.45 ± 0.11	15	4.39	9.96e-01
	flat	-	-	194.5 ± 56.6	3.4	62.1 ± 57.0	1.39 ± 0.65	14	0.99	1.00e+00
ZWCL 3146	-	-	-	0.0	-	283.3 ± 27.3	0.45 ± 0.11	15	4.39	9.96e-01
	extr	15	0.30	11.4 ± 2.0	5.7	105.5 ± 6.4	1.29 ± 0.08	12	5.24	9.49e-01
	-	-	-	0.0	-	126.3 ± 4.5	0.98 ± 0.03	13	31.82	2.55e-03
	flat	-	-	11.4 ± 2.0	5.7	105.5 ± 6.4	1.29 ± 0.08	12	5.24	9.49e-01
ZWCL 7160	-	-	-	0.0	-	126.3 ± 4.5	0.98 ± 0.03	13	31.82	2.55e-03
	extr	21	0.40	18.8 ± 3.2	5.9	89.3 ± 7.3	1.34 ± 0.10	18	2.43	1.00e+00
	-	-	-	0.0	-	117.0 ± 4.8	0.93 ± 0.05	19	29.31	6.13e-02
	flat	-	-	21.1 ± 3.1	6.8	86.3 ± 7.2	1.37 ± 0.10	18	2.82	1.00e+00
Zwicky 2701	-	-	-	0.0	-	116.9 ± 4.8	0.90 ± 0.05	19	36.37	9.49e-03
	extr	24	0.40	34.0 ± 4.2	8.2	135.1 ± 10.3	1.37 ± 0.10	21	4.79	1.00e+00
	-	-	-	0.0	-	187.1 ± 6.6	0.87 ± 0.04	22	43.01	4.71e-03
	flat	-	-	39.7 ± 3.9	10.1	126.0 ± 10.2	1.45 ± 0.10	21	5.67	1.00e+00
ZwCl 0857.9+2107	-	-	-	0.0	-	186.4 ± 6.7	0.82 ± 0.04	22	60.27	2.04e-05
	extr	16	0.30	23.6 ± 5.0	4.8	89.6 ± 10.4	1.40 ± 0.17	13	0.92	1.00e+00
	-	-	-	0.0	-	116.8 ± 7.3	0.86 ± 0.07	14	14.36	4.24e-01
	flat	-	-	24.2 ± 5.0	4.9	89.3 ± 10.4	1.40 ± 0.18	13	0.88	1.00e+00
	-	-	-	0.0	-	116.9 ± 7.4	0.85 ± 0.07	14	14.76	3.95e-01

Note. — Col. (1) Cluster name; col. (2) CDA observation identification number; col. (3) method of T_X interpolation (discussed in §3.4); col. (4) maximum radius for fit; col. (5) number of radial bins included in fit; col. (6) best-fit core entropy; col. (7) number of sigma K_0 is away from zero; col. (9) best-fit entropy at 100 kpc; col. (10) best-fit power-law index; col. (11) degrees of freedom in fit; col. (12) χ^2 statistic of best-fit model; and col. (13) probability of worse fit given χ^2 and degrees of freedom.

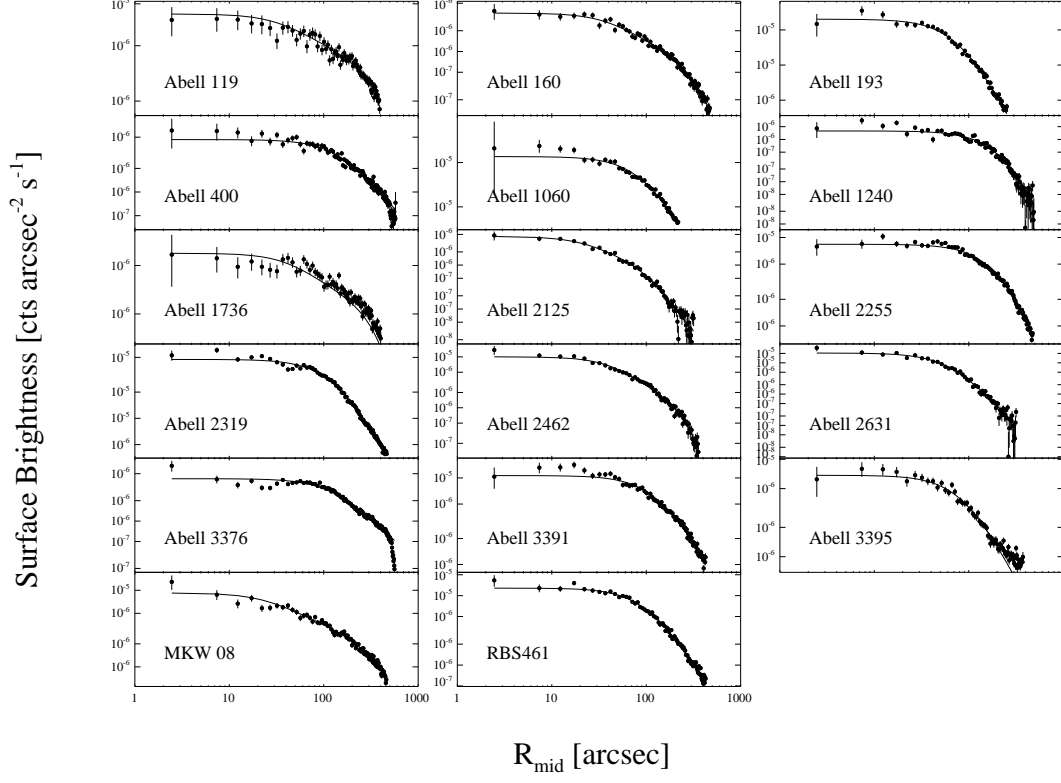


Fig. 1.— Surface brightness profiles for clusters requiring a β -model fit for deprojection (discussed in §3.3). The best-fit β -model for each cluster is overplotted as a dashed line. The discrepancy between the data and best-fit model for some clusters results from the presence of a compact X-ray source at the center of the cluster. These cases are discussed in Appendix A.

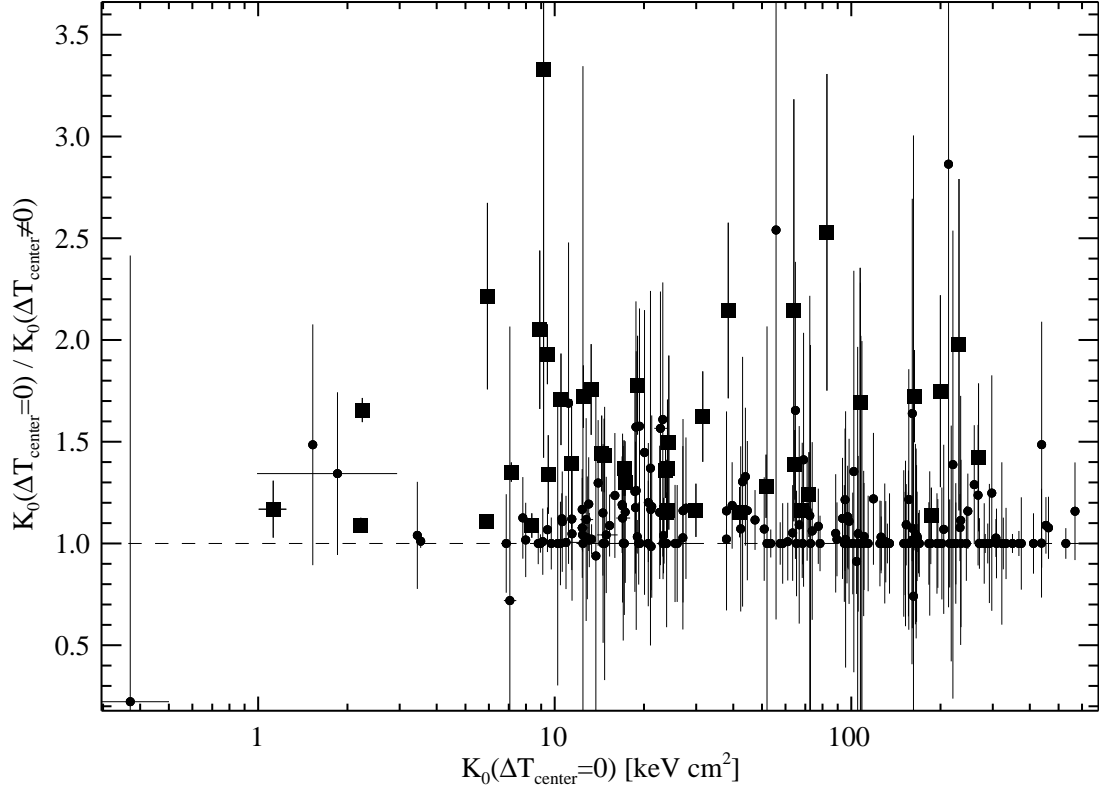


Fig. 2.— Ratio of best-fit K_0 for the two treatments of central temperature interpolation (see §3.1): (1) temperature is free to decline across the central density bins ($\Delta T_{\text{center}} \neq 0$), and (2) the temperature across the central density bins is isothermal ($\Delta T_{\text{center}} = 0$). Filled black squares are clusters for which the K_0 ratio is inconsistent with unity.

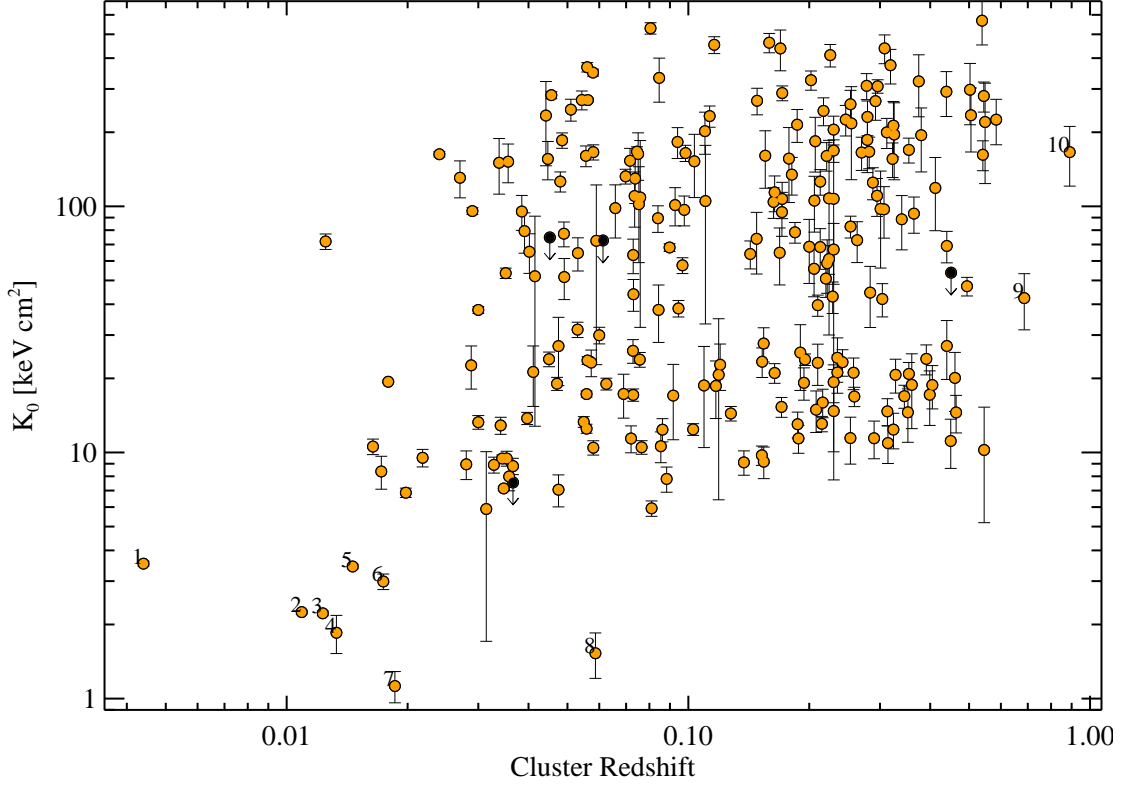


Fig. 3.— Best-fit K_0 vs. redshift. Some clusters have K_0 error bars smaller than the point. The clusters with upper-limits (*black points with downward arrows*) are: A2151, AS0405, MS 0116.3-0115, and RX J1347.5-1145. The numerically labeled clusters are: (1) M87, (2) Centaurus Cluster, (3) RBS 533, (4) HCG 42, (5) HCG 62, (6) SS2B153, (7) A1991, (8) MACS0744.8+3927, and (9) CL J1226.9+3332. For CLJ1226, Maughan et al. (2007) found best-fit $K_0 = 132 \pm 24$ keV cm² which is not significantly different from our value of $K_0 = 166 \pm 45$ keV cm². The lack of $K_0 < 10$ keV cm² clusters at $z > 0.1$ is most likely the result of insufficient angular resolution (see §4.2).

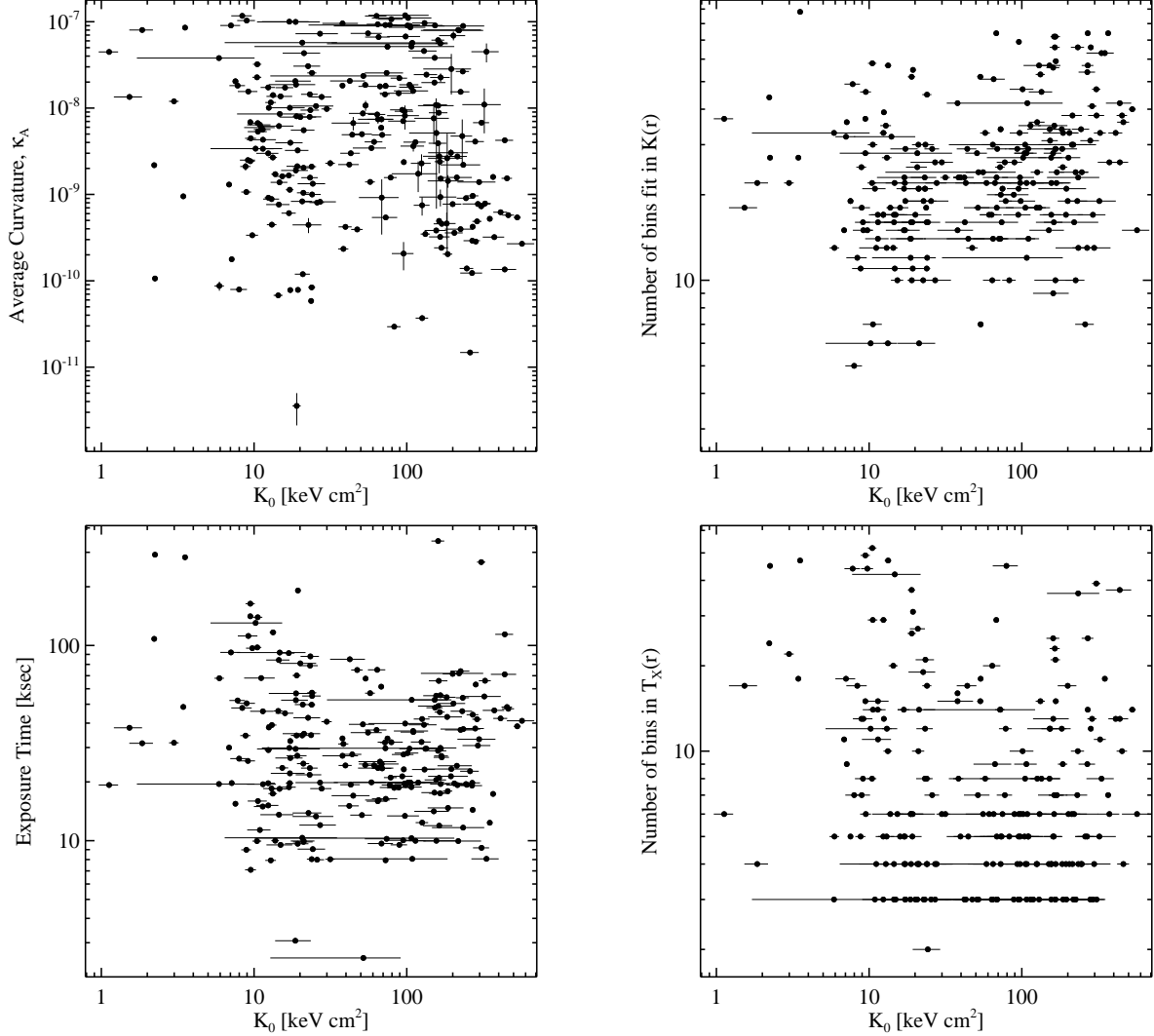


Fig. 4.— Plots of possible systematics versus best-fit K_0 . *Top left:* Best-fit K_0 plotted versus average curvature of the corresponding entropy profile (see eq. 6) There is no trend between these two quantities suggesting that K_0 is not heavily influenced by the total shape of the entropy profile. *Top right:* Best-fit K_0 plotted versus number of bins in the entropy profile which were used during fitting. Again, no trend is found. *Bottom left:* Best-fit K_0 plotted versus the total used exposure time for each cluster. No trend is found. *Bottom right:* Best-fit K_0 plotted versus the number of bins in the temperature profile for each cluster. As expected, fewer $T_X(r)$ does not correlate with K_0 .

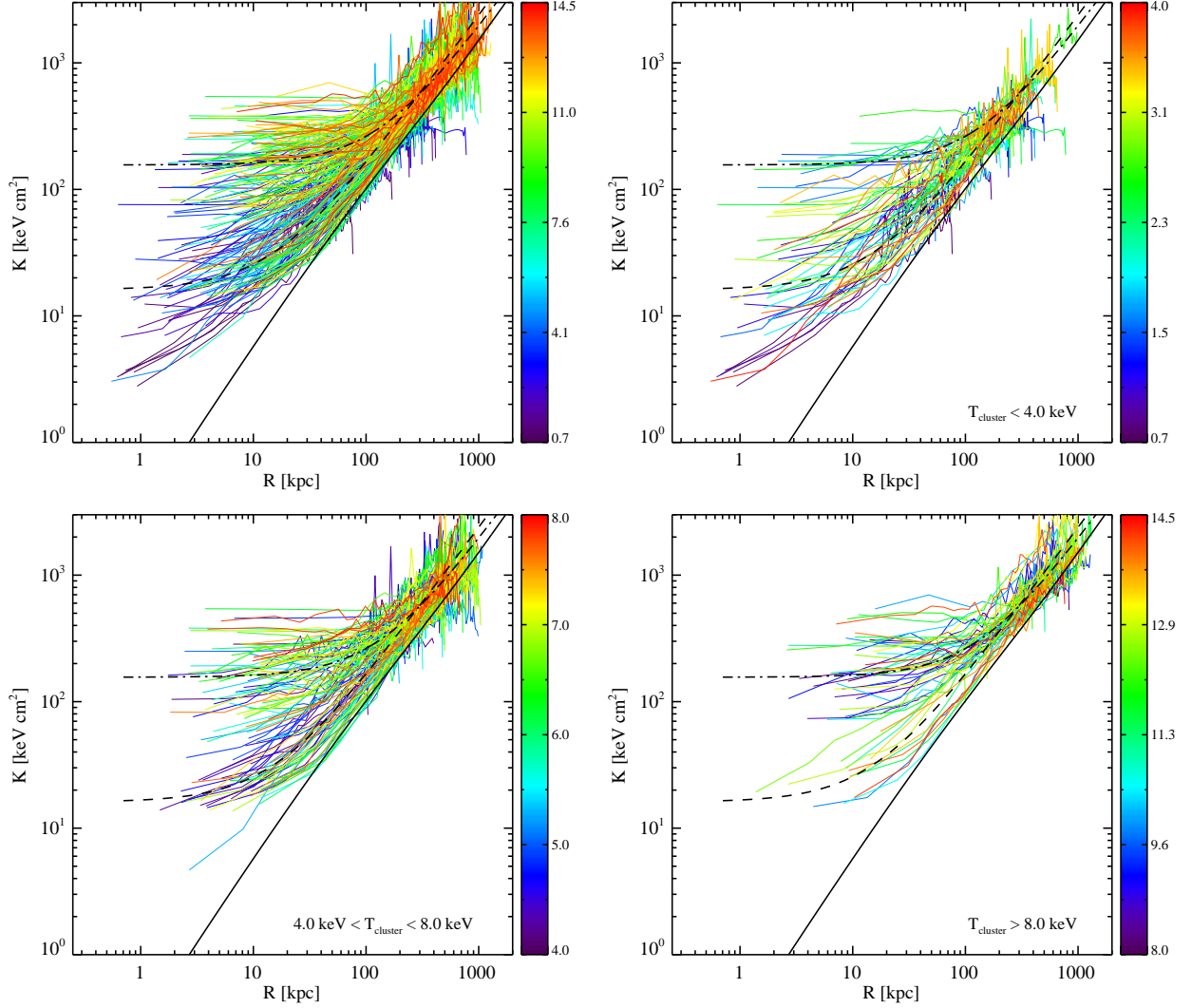


Fig. 5.— Composite plots of entropy profiles for varying cluster temperature ranges. Profiles are color-coded based on average cluster temperature. Units of the color bars are keV. The solid line is the pure-cooling model of Voit et al. (2002), the dashed line is the mean profile for clusters with $K_0 \leq 50 \text{ keV cm}^2$, and the dashed-dotted line is the mean profile for clusters with $K_0 > 50 \text{ keV cm}^2$. *Top left*: This panel contains all the entropy profiles in our study. *Top right*: Clusters with $kT_X < 4 \text{ keV}$. *Bottom left*: Clusters with $4 \text{ keV} < kT_X < 8 \text{ keV}$. *Bottom right*: Clusters with $kT_X > 8 \text{ keV}$. Note that while the dispersion of core entropy for each temperature range is large, as the kT_X range increases so to does the mean core entropy.

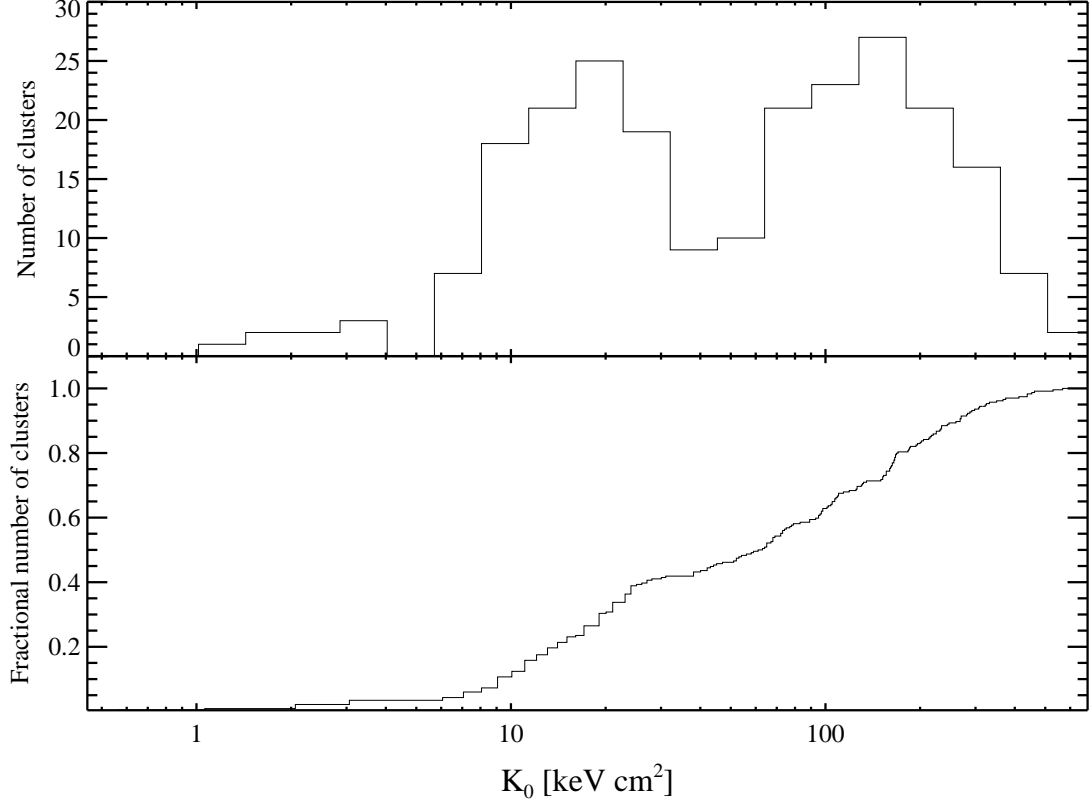


Fig. 6.— *Top panel:* Histogram of best-fit K_0 for all the clusters in *ACCEPT*. Bin widths are 0.15 in log space. *Bottom panel:* Cumulative distribution of K_0 values for the full sample. The distinct bimodality in K_0 is present in both distributions, which would not be seen if it were an artifact of the histogram binning. A KMM test finds the K_0 distribution cannot arise from a simple unimodal Gaussian.

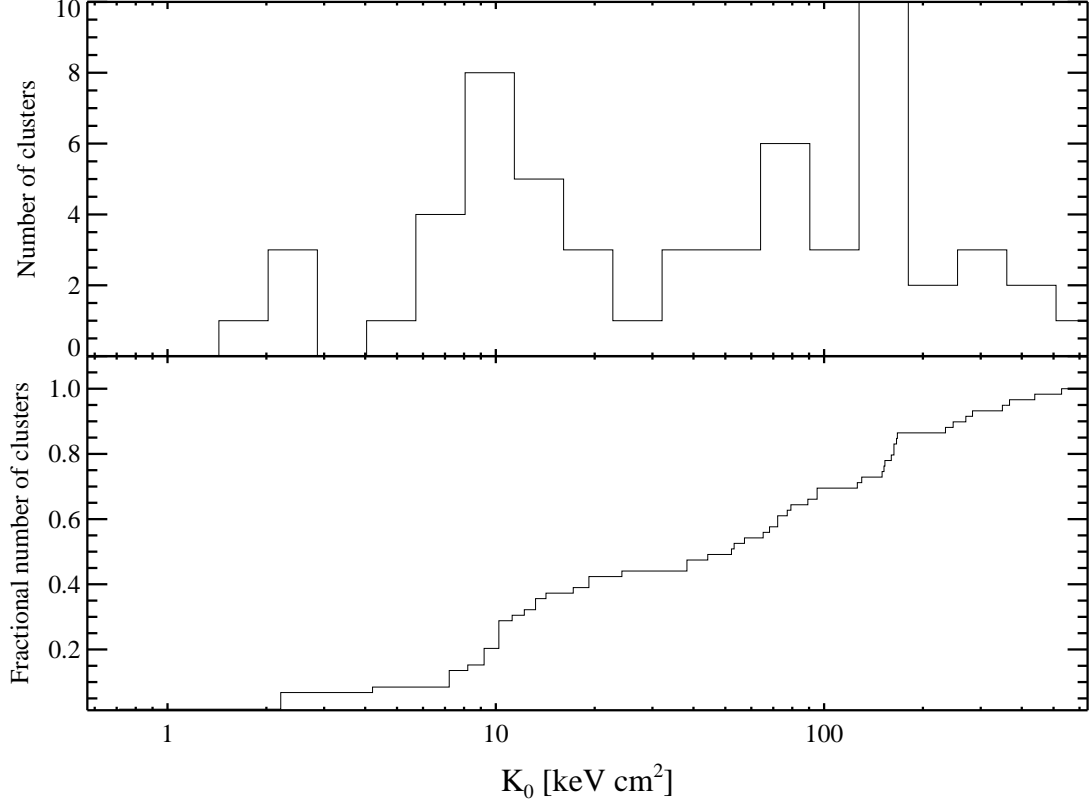


Fig. 7.— *Top panel:* Histogram of best-fit K_0 values for the primary *HIFLUGCS* sample. Bin widths are 0.15 in log space. *Bottom panel:* Cumulative distribution of best-fit K_0 values. The distinct bimodality seen in the full *ACCEPT* sample (Fig. 6) is also present in the *HIFLUGCS* subsample and shares the same gap between the low-entropy peak at 10-20 keV cm² and the high-entropy peak at 100-200 keV cm². That bimodality is present in both samples is strong evidence it is not a result of an unknown archival bias.

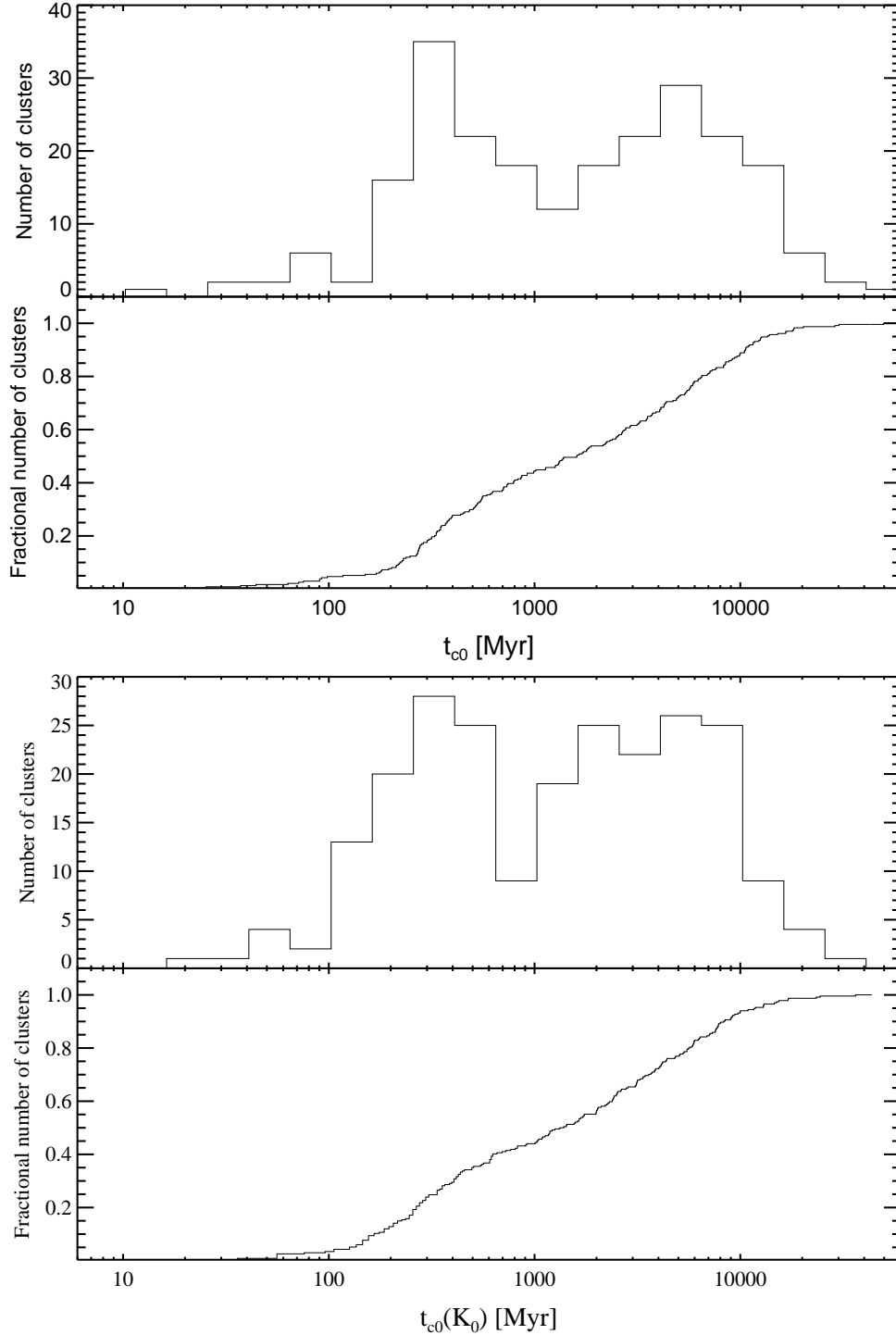


Fig. 8.— *Top panel:* Log-binned histogram and cumulative distribution of best-fit core cooling times, t_{c0} (eqn. 8), for all the clusters in *ACCEPT*. Histogram bin widths are 0.2 in log space. *Bottom panel:* Log-binned histogram and cumulative distribution of core cooling times calculated from best-fit K_0 values, $t_{c0}(K_0)$ (eqn. 9), for all the clusters in *ACCEPT*. Histogram bin widths are 0.2 in log space. The bimodality we observe in the K_0 distribution is also present in best-fit t_{c0} . However, the gaps between the two populations of t_{c0} and $t_{c0}(K_0)$ differ by ~ 0.3 Gyrs which may be an artifact of the binning.